

International Journal of Modern Physics E  
 © World Scientific Publishing Company

## OPEN AND HIDDEN CHARM IN PROTON-NUCLEUS AND HEAVY-ION COLLISIONS

O. LINNYK

*Frankfurt Institute for Advanced Studies, Ruth-Moufang-Str. 1  
 60438 Frankfurt am Main, Germany  
 Linnyk@fias.uni-frankfurt.de*

E. L. BRATKOVSKAYA

*Frankfurt Institute for Advanced Studies, Ruth-Moufang-Str. 1;  
 Institut für Theoretische Physik, Johann Wolfgang Goethe University, Max-von-Laue-Str. 1  
 60438 Frankfurt am Main, Germany  
 Elena.Bratkovskaya@th.physik.uni-frankfurt.de*

W. CASSING

*Institut für Theoretische Physik, Universität Giessen, Heinrich-Buff-Ring 16  
 35392 Giessen, Germany  
 Wolfgang.Cassing@theo.physik.uni-giessen.de*

Received (received date)

Revised (revised date)

We review the collectivity and the suppression pattern of charmed mesons - produced in proton-nucleus and nucleus-nucleus collisions at SPS ( $\sim 158$  A·GeV) and RHIC energies ( $\sim 21$  A·TeV) - in comparison to dynamical and thermal models. In particular, we examine the charmonium ‘melting’ and the ‘comover dissociation’ scenarios - implemented in a microscopic transport approach - in comparison to the available data from the SPS and RHIC. The analysis shows that the dynamics of  $c, \bar{c}$  quarks at RHIC are dominated by partonic or ‘pre-hadronic’ interactions in the strongly coupled plasma stage and can neither be modeled by ‘hadronic’ interactions nor described appropriately by color screening alone. Both the ‘charmonium melting’ and the hadronic ‘comover absorption and recreation model’ are found, however, to be compatible with the experimental observation at SPS energies; the experimental ratio of  $\Psi'/J/\Psi$  versus centrality clearly favors the ‘hadronic comover’ scenario. We find that the collective flow of charm in the purely hadronic Hadron-String Dynamics (HSD) transport appears compatible with the data at SPS energies, but substantially underestimates the data at top RHIC energies. Thus, the large elliptic flow  $v_2$  of  $D$ -mesons and the low  $R_{AA}(p_T)$  of  $J/\Psi$  seen experimentally have to be attributed to early interactions of non-hadronic degrees of freedom. Simultaneously, we observe that non-hadronic interactions are mandatory in order to describe the narrowing of the  $J/\Psi$  rapidity distribution from  $pp$  to central  $Au + Au$  collisions at the top RHIC energy of  $\sqrt{s} = 200$  GeV. We demonstrate additionally that the strong quenching of high- $p_T$   $J/\Psi$ 's in central  $Au + Au$  collisions indicates that a large fraction of final  $J/\Psi$  mesons is created by a coalescence mechanism close to the phase boundary. Throughout this review we, furthermore, provide predictions for charm observables from Au+Au collisions at FAIR energies of 25 - 35 A·GeV.

2 *Contents***Contents**

<b>1</b>	<b>Introduction</b>	<b>3</b>
<b>2</b>	<b>Transport models and elementary reactions</b>	<b>5</b>
<b>3</b>	<b>Energy-density evolution in relativistic heavy-ion collisions</b>	<b>11</b>
3.1	SPS energies . . . . .	11
3.2	RHIC energies . . . . .	13
3.3	FAIR energies . . . . .	15
<b>4</b>	<b>Proton-nucleus reactions: Cold nuclear matter effects</b>	<b>16</b>
4.1	SPS energies . . . . .	17
4.2	RHIC energies . . . . .	20
4.3	FAIR energies . . . . .	24
<b>5</b>	<b>Hadron abundances from heavy-ion collisions</b>	<b>24</b>
<b>6</b>	<b>Anomalous suppression of <math>J/\Psi</math>: The basic models</b>	<b>27</b>
6.1	‘Comover’ suppression (and recombination) . . . . .	27
6.2	‘Threshold melting’ (and recombination) . . . . .	35
6.3	Charm interactions with pre-hadrons in the early phase . . . . .	36
6.4	Thermal and statistical models . . . . .	37
<b>7</b>	<b>Anomalous suppression of <math>J/\Psi</math>: Comparison to data</b>	<b>39</b>
7.1	$J/\Psi$ and $\Psi'$ suppression at SPS energies . . . . .	39
7.2	Thermal and statistical models at SPS . . . . .	44
7.3	$J/\Psi$ and $\Psi'$ at RHIC . . . . .	46
7.4	Charmonia excitation functions . . . . .	52
7.5	FAIR energies . . . . .	54
<b>8</b>	<b>Testing the assumption of statistical hadronization</b>	<b>55</b>
<b>9</b>	<b>Transverse mass spectra</b>	<b>56</b>
9.1	Elementary collisions . . . . .	58
9.2	SPS and RHIC energies . . . . .	58
9.3	FAIR energies . . . . .	59
<b>10</b>	<b>High <math>p_T</math> quenching of open charm and charmonia</b>	<b>60</b>
<b>11</b>	<b>Collective flow</b>	<b>63</b>
11.1	SPS energies . . . . .	64
11.2	RHIC energies . . . . .	65
11.3	FAIR energies . . . . .	67

<b>12 Conclusions</b>	<b>68</b>
<b>13 Open questions and perspectives</b>	<b>69</b>

## 1. Introduction

The formation of a quark-gluon plasma and its transition to interacting hadronic matter has motivated a large community for almost three decades<sup>1</sup>. According to current understanding, the universe in the ‘Big Bang’ scenario has evolved from a quark-gluon plasma (QGP) to color neutral hadronic states within the first second of its lifetime. In this context, the phase transition from partonic degrees of freedom (quarks and gluons) to interacting hadrons is a central topic of modern high-energy physics. In order to understand the dynamics and relevant scales of this transition laboratory experiments under controlled conditions are performed with relativistic nucleus-nucleus collisions. The study of nuclear matter under extremely high baryon density and temperature – where according to lattice quantum chromodynamics (QCD)<sup>2</sup> the hadronic matter transforms to a strongly interacting quark-gluon plasma (sQGP) – is the aim of a variety of experiments at current and future facilities: NA38, NA50 and NA60 at the Super-Proton-Synchrotron (SPS)<sup>3,4,5</sup>; PHENIX, STAR, PHOBOS and BRAHMS at the Relativistic-Heavy-Ion-Collider (RHIC)<sup>6</sup>; ALICE at the Large-Hadron-Collider (LHC)<sup>7,8</sup>; CBM and PANDA at the Facility for Antiproton and Ion Research (FAIR)<sup>9</sup>; NA61 at the SPS Heavy-Ion and Neutrino Experiment (SHINE)<sup>10</sup>; MPD at the Nuclotron-based Ion Collider Facility (NICA)<sup>11</sup>.

Relativistic nucleus-nucleus collisions have been studied so far at beam energies from 0.1 to 2 A·GeV at the SIS (SchwerIonen-Synchrotron), from 2 to 11.6 A·GeV at the AGS (Alternating Gradient Synchrotron) and from 20 to 160 A·GeV at the SPS<sup>12,13</sup>. While part of these programs are closed now, the heavy-ion research has been extended at RHIC with Au+Au collisions at invariant energies  $\sqrt{s}$  from  $\sim 20$  to 200 GeV (equivalent energies in a fixed target experiment: 0.2 to 21.3 A·TeV). In the near future, further insight into the physics of matter at even more extreme conditions will be gained at the LHC, which will reach center-of-mass energies of the TeV scale. Apart from LHC, the SPS successor SHINE will operate at CERN in order to scan the 10A-158A·GeV energy range with light and intermediate mass nuclei<sup>10</sup>. At FAIR, which is expected to start operation in 2015, collisions of gold nuclei from 5 A·GeV up to 35 A·GeV will be studied, thus exploring the high baryon density region of the nuclear matter phase diagram. At NICA it is planned to start the experimental program of colliding Au and/or U ions as well as polarized light nuclei at energies up to of 5 A·GeV in 2013 (an upgrade to 9 A·GeV is foreseen<sup>14</sup>).

In fact, estimates based on the Bjorken formula<sup>15</sup> for the energy density achieved in central Au+Au collisions suggest that the critical energy density for the formation of a QGP is by far exceeded during a few fm/c in the initial phase of the collision at RHIC energies ( $\sqrt{s}$  up to 200 GeV), but sufficient energy den-

sities ( $\sim 0.7\text{-}1\text{ GeV}/\text{fm}^3$ , *cf.* Ref. <sup>16</sup>) might already be achieved at AGS energies of  $\sim 10\text{ A}\cdot\text{GeV}$  <sup>17,18,19</sup> and thus also for the energy regime of FAIR. The crucial question is, however, whether the partonic system really reaches thermal and chemical equilibrium in relativistic nucleus-nucleus collisions. Nonequilibrium models are needed to trace the entire collision history, so that one can study the nature of the transition and extract the characteristics of the partonic phase from data.

Currently many properties of the new sQGP phase are still under debate and practically no dynamical concepts are available to describe the freeze-out of partons to color neutral hadrons that are subject to experimental detection. Early concepts of the QGP were guided by the idea of a weakly interacting system of partons (quarks, antiquarks and gluons), because the entropy density and energy density were found in lattice QCD to be close (within 20% accuracy) to the Stefan Boltzmann limit for a relativistic noninteracting system <sup>16</sup>. However, this notion had to be given up in the last years, since experimental observations at RHIC indicated that the new medium created in ultrarelativistic Au+Au collisions interacted even more strongly than hadronic matter. Moreover, in line with earlier theoretical studies in Refs. <sup>20,21,22,23</sup> the medium showed phenomena of an almost perfect liquid of partons <sup>6,24</sup>, *i.e.* a strongly coupled system showing high collectivity. The most intriguing questions have become: what degrees of freedom are relevant in this new sQGP state and how is the transition from the partonic liquid to the gas of interacting hadrons realized?

The  $c, \bar{c}$  quark degrees of freedom are of particular interest in context with the phase transition to the sQGP. The heavy flavor sector is important for unraveling the actual dynamics from the experimental side since the high masses of the charm and especially bottom quarks provide independent (and new) energy scales. The hadronic bound states (with a  $c$  or  $\bar{c}$  quark) have a much larger mass than the ordinary hadrons, and it is expected that  $c\bar{c}$  pairs can only be formed in the very early phase of the heavy-ion collision <sup>25,26,27,28</sup>. As has been proposed in Ref. <sup>29</sup> the strangeness degrees of freedom might play an important role in distinguishing hadronic and partonic dynamics. The kaons (and antikaons), indeed, have been proven to provide a suitable probe for the compression phase in heavy-ion reactions at SIS energies. One expects that, due to the new scale introduced by the charm flavor,  $D$ -mesons can be used in a similar way to probe the high density matter at FAIR around the threshold for open charm production <sup>30</sup>. Moreover, heavy quarkonia ( $c\bar{c}, b\bar{b}$ ) might no longer be bound at high temperature. Due to different binding energies, quarkonium states should ‘melt’ at different temperatures and might provide the cleanest “measurement” for the energy densities achieved <sup>25</sup>.

Apart from the total and relative abundances of charmonia and open charm mesons also their collective properties are of interest. Here especially the transverse momentum (or mass) spectra are expected to provide valuable insight into the dynamics in either the very early or late phase <sup>31,32,33,34</sup>. We recall that the collective properties of open charm mesons go along with a suppression (relative

to scaled  $pp$  reactions) of high transverse momentum  $p_T$  particles as observed at RHIC by the STAR and PHENIX Collaborations<sup>35</sup> as well as the suppression of charmonia ( $J/\Psi$ ,  $\Psi'$ ). Since the charm quarks are produced early in the reaction, their rescattering – reflected in high  $p_T$  suppression – and collectivity (in the elliptic flow  $v_2(p_T)$ ) signal more sensitively the dynamics of the early phase. All the arguments above qualify charm-flavored particles as practical and promising probes for an exploration of QCD matter.

The present review is structured as follows: We shall start in Section 2 with a description of elementary reactions involving ‘charm’ and introduce the transport models that will be employed for a dynamical description of proton-nucleus and nucleus-nucleus collisions, respectively. The latter dynamical models allow for an overview of the local energy densities achieved in Au+Au collisions from FAIR to RHIC energies (Section 3). We continue with ‘cold nuclear matter’ effects in proton-nucleus reactions in Section 4 and provide information about the ‘hadronic environment’ of charmonia encountered in relativistic heavy-ion reactions in Section 5. The leading concepts/models for charmonium dynamics are presented in Section 6 as well as their actual implementation in the microscopic transport approach. The relative abundances of charmonia and open charm mesons are presented in Section 7 together with a discussion of the anomalous suppression of charmonia ( $J/\Psi$ ,  $\Psi'$ ) in comparison to the experimental data available. The issue of charmonium chemistry is examined in Section 8 in comparison with the statistical hadronization model. Sections 9 and 10 are devoted to the energy loss of charmonia in the dense medium, i.e. in particular to the transverse mass spectra and high  $p_T$  quenching. The collective flow properties of open charm and charmonia are studied for the elliptic flow  $v_2$  in Section 11. We conclude with a summary and discussion of open questions in Sections 12 and 13.

## 2. Transport models and elementary reactions

The main difficulty in the study of nuclear matter under extreme conditions as created in relativistic heavy-ion collisions is that the information about the initial sQGP stage of matter can be obtained only *indirectly* from the measurement of hadronic observables. The sQGP signal might be strongly distorted by the hadronization process and final state interactions of the hadrons. In order to reliably subtract the “trivial” hadronic contribution from the sQGP signal, one needs a microscopic transport dynamical approach. Also, the possible equilibration of quark-gluon matter is of central interest. Such issues of equilibration phenomena are traditionally examined within nonequilibrium relativistic transport theory<sup>36,17,37,38,39,40</sup>.

Ideally, one would use a microscopic transport model containing the proper degrees of freedom – quarks and gluons in the initial phase and hadrons in the final phase – and parton dynamics which are consistent with the Lattice QCD equation of state. The development of such approaches is in progress<sup>41,42,43</sup>. However, a

proper understanding of the transport properties of the partonic phase is still lacking (see Section 13 for details). One has to keep in mind that most of the results in this review have been obtained based on hadron-string or hydrodynamical models without including an explicit phase transition to the QGP. As we will see, there are a number of questions that can be answered before the development of a nonperturbative parton-hadron transport approach is completed. For example, the interactions of  $J/\Psi$ 's with formed hadrons in the late stages of the collision (when the energy density falls below a critical value of about 1 GeV/fm<sup>3</sup> corresponding roughly to the critical energy density for a parton/hadron phase transition) gives a sizable contribution to its anomalous suppression at all beam energies as demonstrated in Refs. <sup>44,45,46,33,47,48</sup>. Accordingly, this more obvious hadronic contribution has to be incorporated when comparing possible models for QGP-induced charmonium suppression to experimental data.

In any case, the link of the underlying physics to the heavy ion experiments should be provided by dynamical transport models, such as UrQMD <sup>40,49</sup>, HSD <sup>50,36</sup>, GiBUU <sup>51,52</sup>, RQMD <sup>53</sup>, QGSM <sup>54,55</sup>, or AMPT <sup>42</sup>. we recall that microscopic (pre-)hadronic transport models describe the formation and distributions of many hadronic particles from SIS to SPS energies reasonably well <sup>56</sup>. Furthermore, the nuclear equation of state has been extracted by comparing transport calculations to hadron flow data up to AGS energies <sup>57,58,59,60,61,62</sup>. In particular, at SIS energies, microscopic transport models reproduce the data on the excitation function of the proton elliptic flow  $v_2$  when incorporating a soft, momentum-dependent equation of state <sup>63,64,65,52</sup>. In addition to nucleus-nucleus collisions from SIS to SPS energies <sup>56,66</sup>, the HSD transport approach is found to work reasonably well also at RHIC energies for the 'soft' hadron abundances, so that the 'hadronic environment' for open charm mesons and charmonia should be sufficiently realistic <sup>47</sup>. One also finds generally a good agreement among the predictions of different transport models for hadron multiplicities. Modest differences between the HSD and UrQMD transport results for pion and kaon multiplicities can be attributed to different implementations of string formation and fragmentation, which are not sufficiently controlled by experimental data.

The precision of such models depends crucially on the elementary input, i.e. the knowledge of the elementary reaction cross sections. In order to tackle the production and dynamics of charmed hadrons in heavy-ion collisions, one needs data from  $NN$  and  $\pi N$  reactions at different energies to establish the underlying cross sections and distributions. One can apply perturbative QCD (pQCD) to calculate the total cross section for  $c\bar{c}$  pair production. The results of next-to-leading order pQCD <sup>68</sup> calculations are shown in Fig. 1 in comparison to  $pp$  data as well as to  $pA$  ( $AA$ ) measurements divided by the number of binary collisions  $N_{coll}$  (charm pairs, due to their high mass, are expected to be produced only in initial nucleon-nucleon collisions and their yield should scale with  $N_{coll}$ ). The discrepancy of a factor of  $\sim 2$  between the PHENIX and STAR cross sections is not yet understood. Moreover, the large theoretical uncertainty implies that there is little predictive

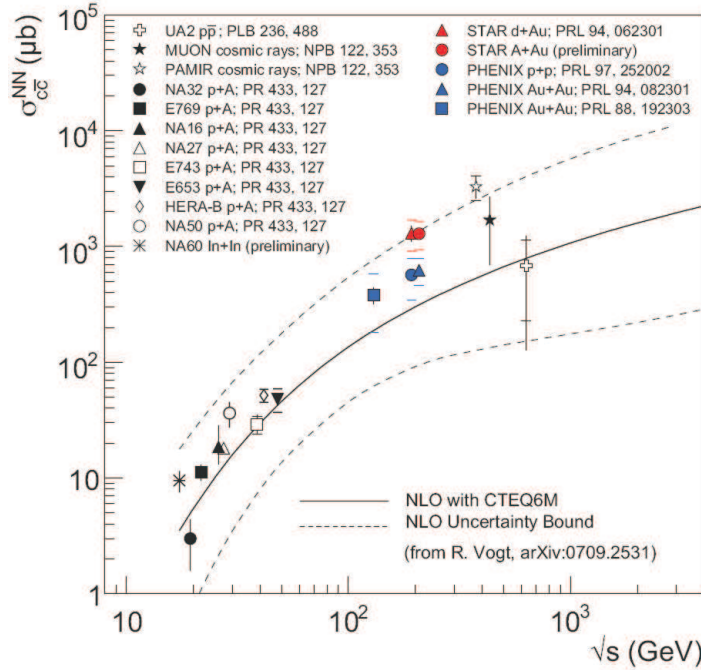


Fig. 1. Comparison of total cross section measurements for  $c\bar{c}$  pairs as a function of the invariant energy  $\sqrt{s}$ . The STAR and PHENIX results are given as cross section per binary collisions; vertical lines reflect the statistical errors, horizontal bars indicate the systematic uncertainties (where available). The figure is taken from Ref. 67.

power in the pQCD total charm cross section. Therefore, the use of phenomenological parametrizations of the world data for the total charm cross sections from elementary reactions is legitimate so far. This approach is followed up in transport models.

In the rest of this Section we present the implementation of charm production from elementary hadron collisions in the Hadron-String-Dynamics (HSD) <sup>36</sup> transport model<sup>a</sup>. The total cross sections for the elementary production channels including the charmed hadrons  $D, \bar{D}, D^*, \bar{D}^*, D_s, \bar{D}_s, D_s^*, \bar{D}_s^*, J/\Psi, \Psi(2S), \chi_{2c}$  from  $NN$  and  $\pi N$  collisions were fitted in Refs. <sup>36,44,33,47,18,45</sup> to PYTHIA <sup>80</sup> calculations above  $\sqrt{s} = 10$  GeV and extrapolated to the individual thresholds, while the absolute strength of the cross sections was adjusted to the experimental data (cf. Ref. <sup>33</sup>). The actual results are displayed in Fig. 2 for  $p+N$  and  $\pi+N$  reactions. The total charmonium cross sections ( $i = \chi_c, J/\Psi, \Psi'$ ) from  $NN$  collisions

<sup>a</sup>The open source code is available from Ref. <sup>79</sup>



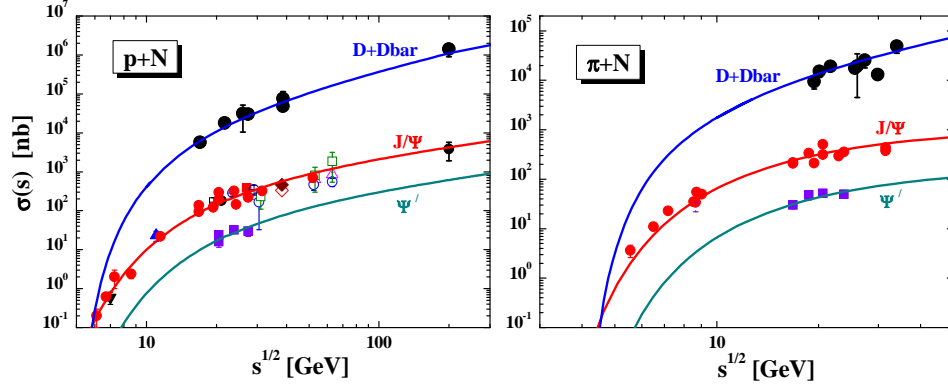


Fig. 2. The cross section for  $D + \bar{D}$ ,  $J/\Psi$  and  $\Psi'$  meson production in  $pN$  (left part) and  $\pi N$  reactions (right part). The solid lines show the parametrizations used in HSD, whereas the symbols stand for the experimental data from Refs. 69,70,71,72,73,74,75,76,77,78. Note that the  $J/\Psi$  cross sections include the decay from  $\chi_c$  mesons. The figure is taken from Ref. 44.

as a function of the invariant energy  $\sqrt{s}$  are approximated by the expression

$$\sigma_i^{NN}(s) = f_i a \left(1 - \frac{m_i}{\sqrt{s}}\right)^\alpha \left(\frac{\sqrt{s}}{m_i}\right)^\beta \theta(\sqrt{s} - \sqrt{s_{0i}}), \quad (1)$$

where  $m_i$  denotes the mass of charmonium  $i$  while  $\sqrt{s_{0i}} = m_i + 2m_N$  is the threshold in vacuum. The parameters in Eq. (1) have been fixed to describe the  $J/\Psi$  and  $\Psi'$  data up to the RHIC energy  $\sqrt{s} = 200$  GeV (*cf.* Ref. 44). We use  $a = 0.16$  mb,  $\alpha = 10$ ,  $\beta = 0.775$ .

The parameters  $f_i$  are fixed as  $f_{\chi_c} = 0.636$ ,  $f_{J/\Psi} = 0.581$ ,  $f_{\Psi'} = 0.21$  in order to reproduce the experimental ratio

$$\frac{B(\chi_{c1} \rightarrow J/\Psi)\sigma_{\chi_{c1}} + B(\chi_{c2} \rightarrow J/\Psi)\sigma_{\chi_{c2}}}{\sigma_{J/\Psi}^{exp}} = 0.344 \pm 0.031$$

measured in  $pp$  and  $\pi N$  reactions<sup>83,84</sup> as well as the averaged  $pp$  and  $pA$  ratio  $(B_{\mu\mu}(\Psi')\sigma_{\Psi'})/(B_{\mu\mu}(J/\Psi)\sigma_{J/\Psi}) \simeq 0.0165$  (*cf.* the compilation of experimental data in Ref. 85). The experimentally measured  $J/\Psi$  cross section includes the direct  $J/\Psi$  component ( $\sigma_{J/\Psi}$ ) as well as the decays of higher charmonium states  $\chi_c$  and  $\Psi'$ , *i.e.*

$$\sigma_{J/\Psi}^{exp} = \sigma_{J/\Psi} + B(\chi_c \rightarrow J/\Psi)\sigma_{\chi_c} + B(\Psi' \rightarrow J/\Psi)\sigma_{\Psi'}. \quad (2)$$

Note, we do not distinguish the  $\chi_{c1}(1P)$  and  $\chi_{c2}(1P)$  states. Instead, we use only the  $\chi_{c1}(1P)$  state (which we denote as  $\chi_c$ ), however, with an increased branching ratio for the decay to  $J/\Psi$  in order to include the contribution of  $\chi_{c2}(1P)$ , *i.e.*  $B(\chi_c \rightarrow J/\Psi) = 0.54$ . Furthermore, we adopt  $B(\Psi' \rightarrow J/\Psi) = 0.557$  from Ref. 86.

We recall that (as in Refs. 33,47,87,88,89) the charm degrees of freedom in the HSD approach are treated perturbatively and that initial hard processes (such as  $c\bar{c}$



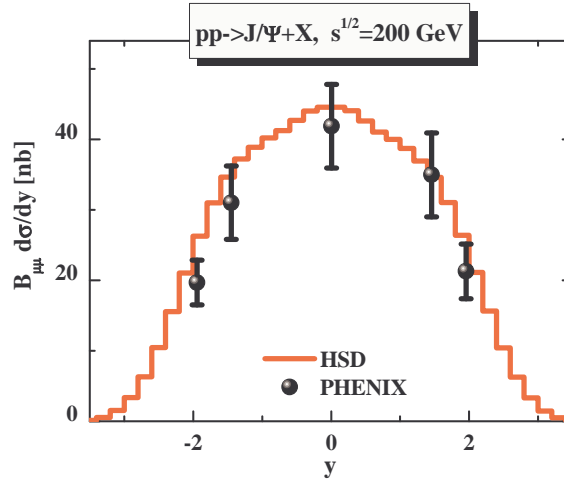


Fig. 3. Cross section for the differential  $J/\Psi$  production in rapidity (times the branching ratio to di-muons  $B_{\mu\mu}$ ) in  $pp$  collisions at  $\sqrt{s} = 200$  GeV. The HSD (input) parametrization (solid line) is compared to the PHENIX data (symbols) from Ref. <sup>81</sup>. The figure is taken from Ref. <sup>82</sup>.

or Drell-Yan production from  $NN$  collisions) are ‘pre-calculated’ to achieve a scaling of the inclusive cross section with the number of projectile and target nucleons as  $A_P \times A_T$  when integrating over impact parameter. For fixed impact parameter  $b$ , the  $c\bar{c}$  yield then scales with the number of binary hard collisions  $N_{coll}$  (cf. Fig. 8 in Ref. <sup>33</sup>). To implement this scaling, we separate the production of the hard and soft processes: The space-time production vertices of the  $c\bar{c}$  pairs are ‘precalculated’ in each transport run by neglecting the soft processes, i.e. the production of light quarks and associated mesons, and then reinserted in the dynamical calculation at the proper space-time point during the actual calculation that includes all soft processes. As shown in Ref. <sup>33</sup> this prescription is very well in line with Glauber calculations for the production of hard probes at fixed impact parameter, too. We mention that this ‘precalculation’ of  $c\bar{c}$  production might be modified at RHIC energies due to changes of the gluon structure functions during the heavy-ion reaction or related shadowing phenomena <sup>90</sup>. The amount of shadowing at RHIC energies will be discussed in more detail in Section 4.

In addition to primary hard  $NN$  collisions, the open charm mesons or charmonia may also be generated by secondary meson-baryon ( $mB$ ) reactions. Here we include all secondary collisions of mesons with baryons by assuming that the open charm cross section (from Section 2 of Ref. <sup>33</sup>) only depends on the invariant energy  $\sqrt{s}$  and not on the explicit meson or baryon state. Furthermore, we take into account all interactions of ‘formed’ mesons – after a formation time of  $\tau_F \approx 0.8$  fm/c (in their rest frame) <sup>91</sup> – with baryons or diquarks. For the total charmonium cross sections from meson-baryon (or  $\pi N$ ) reactions we use the parametrization (in line

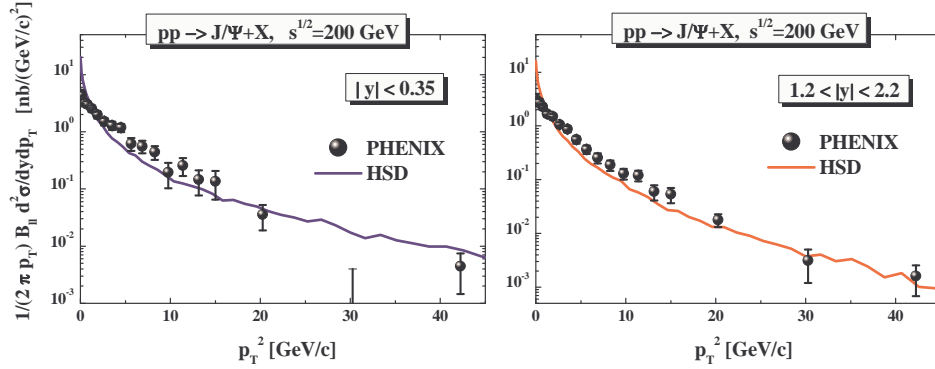


Fig. 4. Differential cross section of  $J/\Psi$  production in  $pp$  collisions at  $\sqrt{s} = 200$  GeV at mid-rapidity ( $|y| < 0.35$ , l.h.s.) and at forward rapidity ( $1.2 < |y| < 2.2$ , r.h.s.) vs the transverse momentum squared  $p_T^2$ , as implemented in HSD (solid line) compared to the PHENIX data from Ref. <sup>81</sup> (dots). The figure is taken from Ref. <sup>82</sup>.

with Ref. <sup>92</sup>):

$$\sigma_i^{\pi N}(s) = f_i b \left(1 - \frac{m_i}{\sqrt{s}}\right)^\gamma \quad (3)$$

with  $\gamma = 7.3$  and  $b = 1.24$  mb, which describes the existing experimental data at low  $\sqrt{s}$  reasonably well, as seen in Fig. 2.

Apart from the total cross sections for charmonia we also need the differential distributions of the produced mesons in the transverse momentum  $p_T$  and the rapidity  $y$  (or Feynman  $x_F$ ) from each individual collision. We recall that  $x_F = p_z/p_z^{max} \approx 2p_z/\sqrt{s}$  with  $p_z$  denoting the longitudinal momentum. For the differential distribution in  $x_F$  from  $NN$  and  $\pi N$  collisions we use the ansatz from the E672/E706 Collaboration <sup>93</sup> and for the  $p_T$  distribution: an exponential

$$\frac{dN}{dx_F dp_T} \sim (1 - |x_F|)^c \exp(-b_{p_T} p_T) \quad (4)$$

with  $b_{p_T} = 2.08$  GeV<sup>-1</sup> at SPS energies or a power law parametrization from Ref. <sup>94</sup> which has been fixed by the STAR data <sup>95</sup> at high energies relevant to RHIC, *i.e.*

$$\frac{dN}{dx_F dp_T} \sim (1 - |x_F|)^c \left(1 + \frac{p_T}{b_{p_T}}\right)^{c_{p_T}} \quad (5)$$

with  $b_{p_T} = 3.5$  GeV/ $c$  and  $c_{p_T} = -8.3$ . The exponent  $c$  is given by  $c = a/(1 + b/\sqrt{s})$  and the parameters  $a, b$  are chosen as  $a_{NN} = 16$ ,  $b_{NN} = 24.9$  GeV for  $NN$  collisions and  $a_{\pi N} = 4.11$ ,  $b_{\pi N} = 10.2$  GeV for  $\pi N$  collisions <sup>47,33</sup>. Note that the parametrizations of the differential cross sections are taken as in Refs. <sup>33,47</sup>, apart from a readjustment of the parameter  $a_{NN}$  in order to reproduce the recently measured rapidity distribution of  $J/\Psi$ 's in  $p + p$  reactions at  $\sqrt{s} = 200$  GeV by PHENIX <sup>81</sup> in Ref. <sup>45</sup>.

The resulting rapidity distribution for  $J/\Psi$  production in  $pp$  collisions at  $\sqrt{s} = 200$  GeV is shown in Fig. 3. We also present the  $pp \rightarrow J/\Psi + X$  differential cross section in  $p_T^2$  at mid-rapidity ( $|y| < 0.35$ ) and at forward rapidity (averaged in the interval  $1.2 < |y| < 2.2$ ) in Fig. 4. Both kinematical distributions (in  $y$  and  $p_T$ ) are in line with the data from Ref. <sup>81</sup> within error bars.

### 3. Energy-density evolution in relativistic heavy-ion collisions

The HSD approach <sup>36</sup> provides the space-time geometry of nucleus-nucleus reactions and a rather reliable estimate for the local energy densities achieved, since the production of secondary particles with light and a single strange quark/antiquark is described well from SIS to RHIC energies <sup>56,66</sup> (see also Section 5). In the transport approach the local energy density is calculated from the energy-momentum tensor  $T_{\mu\nu}(x)$  for all space-time points  $x$  in the local rest frame:  $\varepsilon(x) = T_{00}^{loc}(x)$ , where  $T_{00}^{loc}(x)$  is calculated from  $T_{\mu\nu}(x)$  by a Lorentz boost to the local rest frame. In order to exclude contributions to  $T_{\mu\nu}$  from noninteracting nucleons in the initial phase all nucleons without prior interactions are discarded in the rapidity intervals  $[y_{tar} - 0.4, y_{tar} + 0.4]$  and  $[y_{pro} - 0.4, y_{pro} + 0.4]$  where  $y_{tar}$  and  $y_{pro}$  denote projectile and target rapidity, respectively. Note that the initial rapidity distributions of projectile and target nucleons are smeared out due to Fermi motion by about  $\Delta y \approx \pm 0.4$ . Some comments on the choice of the grid in space-time are in order here: In the actual calculation (for Au+Au collisions) the initial grid has a dimension of  $1 \text{ fm} \times 1 \text{ fm} \times 1/\gamma_{cm} \text{ fm}$ , where  $\gamma_{cm}$  denotes the Lorentz  $\gamma$ -factor in the nucleon-nucleon center-of-mass system. After the time of maximum overlap  $t_m$  of the nuclei the grid-size in beam direction  $\Delta z_0 = 1/\gamma_{cm} \text{ [fm]}$  is increased linearly in time as  $\Delta z = \Delta z_0 + a(t - t_m)$ , where the parameter  $a$  is chosen in a way to keep the particle number in the local cells of volume  $\Delta V(t) = \Delta x \Delta y \Delta z(t)$  roughly constant during the longitudinal expansion of the system. In this way local fluctuations of the energy density  $\varepsilon(x)$  due to fluctuations in the particle number are kept low. Furthermore, the time-step is taken as  $\Delta t = 0.2 \Delta z(t)$  and increases in time in analogy to  $\Delta z(t)$ . This choice provides a high resolution in space and time for the initial phase and keeps track of the relevant dynamics throughout the entire collision history.

#### 3.1. SPS energies

As a first example we display in Fig. 5 the energy density  $\varepsilon(x, y = 0, z; t)$  for a Pb+Pb collision at 160 A-GeV and impact parameter  $b = 1 \text{ fm}$  in terms of contour lines for times of 1, 2, 3 and 5 fm/c (from contact). It is clearly seen that energy densities above  $4 \text{ GeV/fm}^3$  are reached in the early overlap phase of the reaction and that  $\varepsilon(x)$  drops within a few fm/c below  $1 \text{ GeV/fm}^3$  in the center of the grid. On the other hand the energy density in the region of the leading particles - moving almost with the velocity of light - stays above  $1 \text{ GeV/fm}^3$  due to Lorentz time dilatation since the time  $t$  here is measured in the nucleon-nucleon center-of-mass

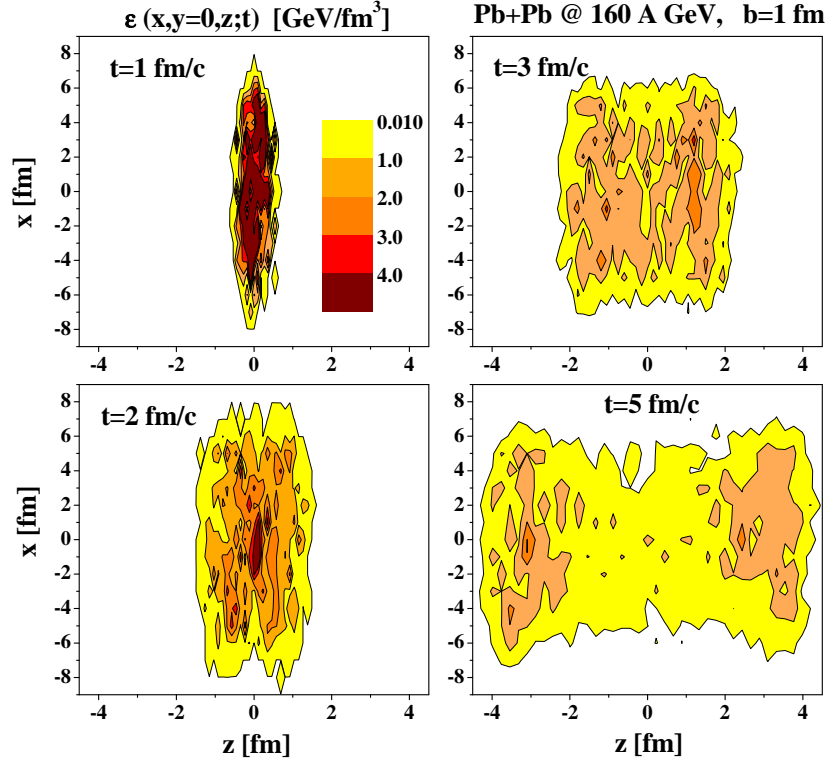


Fig. 5. The energy density  $\varepsilon(x, y = 0, z; t)$  from HSD for a Pb+Pb collision at 160 A·GeV and impact parameter  $b = 1$  fm in terms of contour lines (0.01, 1, 2, 3, 4 GeV/fm<sup>3</sup>) for times of 1, 2, 3 and 5 fm/c (from contact). Note that noninteracting nucleons have been discarded in the actual calculation of the energy-momentum tensor. The figure is taken from Ref. <sup>44</sup>.

system. Note that in the local rest frame of the leading particles the eigentime  $\tau$  is roughly given by  $\tau \approx t/\gamma_{cm}$  with  $\gamma_{cm} \approx 9.3$  (at 160 A·GeV).

Another view of the space time evolution of the energy density is given in Fig. 6 where we display  $\varepsilon(x = 0, y = 0, z; t)$  for the same system as in Fig. 5 on a linear scale. The contact time of the two Pb nuclei here is 2 fm/c and the overlap phase of the Lorentz contracted nuclei is identified by a sharp peak in space-time which is essentially given by the diameter of the nuclei divided by  $\gamma_{cm}$ . As noted before, the energy density in the center of the reaction volume ( $z \approx 0$ ) drops fast below 1 GeV/fm<sup>3</sup> whereas the ridges close to the light-cone basically stem from the leading ends of the strings formed in the early nucleon-nucleon collisions. In these space-time regions all reaction rates are reduced by the factor  $\sim 1/\gamma_{cm}$  such that the transport calculations have to be carried out to large times of several hundred fm/c in order to catch the dynamics and decays in these regions. In the central regime, however, all interaction rates vanish after about 15 fm/c. Since the  $c, \bar{c}$  pairs are produced dominantly at midrapidity with a small spread in rapidity ( $\sigma_y \approx 0.8$  at 160 A·GeV) it is the central region that is of primary interest for this study.

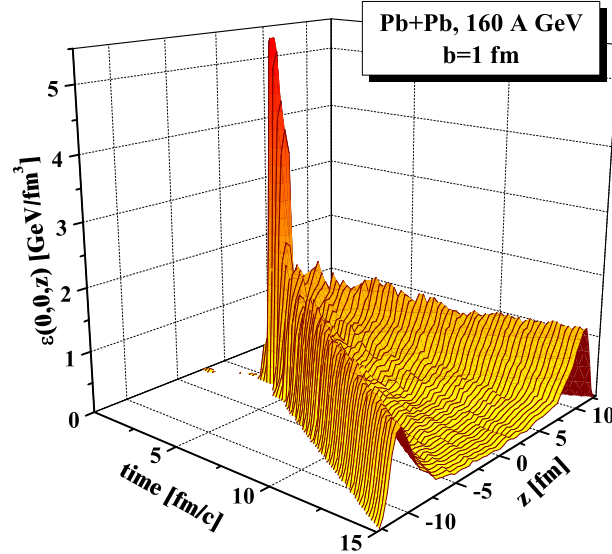


Fig. 6. The energy density  $\varepsilon(x = 0, y = 0, z; t)$  from HSD for a Pb+Pb collision at 160 A·GeV and impact parameter  $b = 1$  fm on a linear scale. Note that noninteracting nucleons have been discarded in the actual calculation of the energy-momentum tensor such that  $\varepsilon(x) \neq 0$  only after contact of the two Pb nuclei which is  $\sim 2$  fm/c. The figure is taken from Ref. <sup>44</sup>.

### 3.2. RHIC energies

The energy density  $\varepsilon(\mathbf{r}; t)$  becomes very high in a central Au+Au collision at  $\sqrt{s} = 200$  GeV as shown in Fig. 7 (in analogy to Fig. 6 for the top SPS energies). Fig. 7 shows the space-time evolution of the energy density  $\varepsilon(x = 0, y = 0, z; t)$  for a Au+Au collision at 21300 A·GeV or  $\sqrt{s} = 200$  GeV. It is clearly seen that energy densities above  $16 \text{ GeV/fm}^3$  are reached in the early overlap phase of the reaction and that  $\varepsilon(x)$  drops after about 6 fm/c (starting from contact) below  $1 \text{ GeV/fm}^3$  in the center of the grid. On the other hand the energy density in the region of the leading particles - moving almost with the velocity of light - stays above  $1 \text{ GeV/fm}^3$  due to Lorentz time dilatation since the time  $t$  in the transport calculation is measured in the nucleon-nucleon center-of-mass system. As seen from Fig. 7, the energy density in the local rest frame is a rapidly changing function of time in nucleus-nucleus collisions. For orientation let us quote the relevant time scales (in the cms reference frame):

- The  $c\bar{c}$  formation time  $\tau_c \approx 1/M_\perp$  is about 0.05 fm/c for a transverse mass

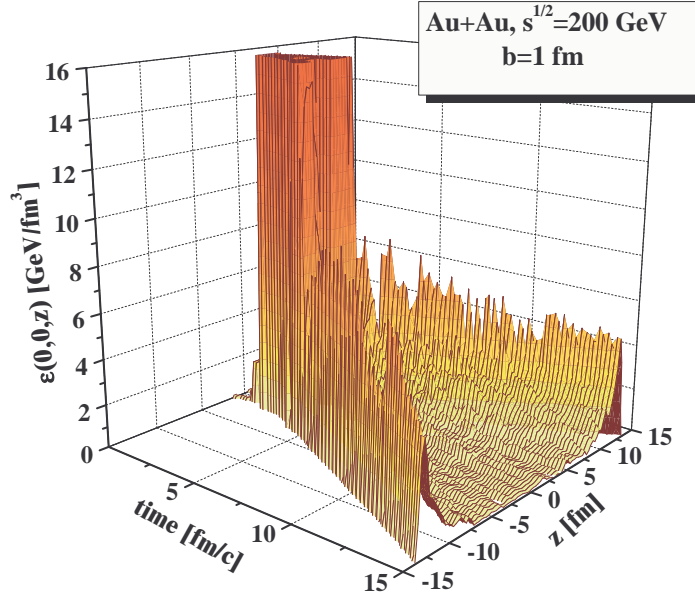


Fig. 7. The energy density  $\varepsilon(x = 0, y = 0, z; t)$  from HSD for a central Au+Au collision at  $\sqrt{s} = 200$  GeV. The time  $t$  is given in the nucleon-nucleon center-of-mass system. The figure is taken from Ref. <sup>82</sup>.

of 4 GeV; the transient time for a central Au+Au collision at  $\sqrt{s} = 200$  GeV is  $t_r \approx 2R_A/\gamma_{cm} \approx 0.13$  fm/c. According to standard assumptions, the  $c\bar{c}$  pairs are produced in the initial hard  $NN$  collisions dominantly by gluon fusion in the time period  $t_r$ . In fact, the formation time  $\tau_c$  is significantly smaller than  $t_r$ , which implies that the  $c$  or  $\bar{c}$  quarks may interact with the impinging nucleons of the projectile or target for times  $t \leq t_r$ .

– Using the Bjorken estimate for the energy density and employing the time-scale  $t_r = 0.13$  fm/c, the energy density – after the nuclei have punched through each other – amounts to about  $5/0.13 > 30$  GeV/fm<sup>3</sup> (as quoted also in the HSD calculations in Refs. <sup>45,82</sup>). Even when adding the  $c\bar{c}$  formation time, this gives an energy density  $\sim 5/0.18 \approx 28$  GeV/fm<sup>3</sup>. So the numbers in Fig. 7 agree with transparent and simple estimates and illustrate the high initial densities after  $c\bar{c}$  production from primary interactions.

The energy densities quoted above are considerably different from the estimate

$$\tau \cdot \epsilon_{Bj} = \frac{\langle E_T \rangle \frac{dN}{d\eta}}{\pi R_T^2}, \quad (6)$$

where  $\langle E_T \rangle$  is the average transverse energy per particle,  $dN/d\eta$  the number of particles per unit of pseudorapidity, and  $\tau$  a formation time parameter often used

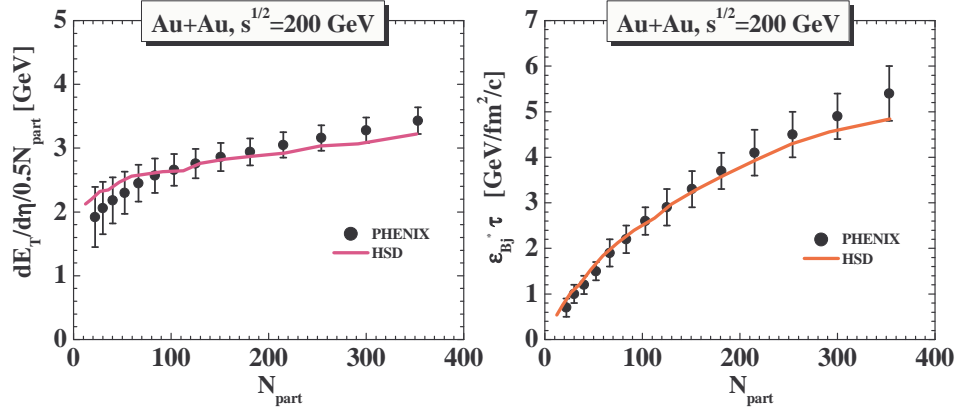


Fig. 8. Left part: The transverse energy  $E_T$  per pseudorapidity interval  $d\eta$  divided by the number of participant pairs ( $0.5N_{part}$ ) from HSD (solid line) in comparison to the PHENIX data (dots)<sup>96</sup>. Right part: The Bjorken energy density  $\epsilon_{Bj} \cdot \tau$  from HSD (solid line) for Au+Au collisions at  $\sqrt{s} = 200$  GeV in comparison to the PHENIX data (dots)<sup>96</sup>. The figure is taken from Ref.<sup>82</sup>.

as  $\tau = 1$  fm/c. Furthermore,  $\pi R_T^2$  denotes the overlap area for the corresponding centrality. It is important to point out that the estimate (6) is only well defined for the product  $\tau \cdot \epsilon_{Bj}$ ! The question naturally arises, if the transport calculations follow the corresponding experimental constraints.

To this aim we show  $dE_T/d\eta$  (divided by half the number of participants  $N_{part}$ ) from HSD in Fig. 8 (l.h.s.) in comparison to the measurements by PHENIX<sup>96</sup>. Accordingly, the Bjorken energy density  $\epsilon_{Bj}$  – multiplied by the time-scale  $\tau$  (6) – from HSD is shown additionally in the r.h.s. of Fig. 8 in comparison to the PHENIX data as a function of  $N_{part}$ . The similarity between the calculated quantities and the experimental data demonstrates that the space-time evolution of the energy-momentum tensor  $T_{\mu\nu}$  in HSD is sufficiently well under control also at RHIC energies.

### 3.3. FAIR energies

The question emerges if central collisions of e.g. Au+Au at the future FAIR facility might be also suited to explore a possible phase transition to the sQGP. For a quantitative orientation we display in Fig. 9 the volume (in the nucleus-nucleus center-of-mass) with energy densities above 1 GeV/fm<sup>3</sup> and 2 GeV/fm<sup>3</sup> as a function of time for a central Au+Au collision at 25 A·GeV, where only interacting and produced hadrons have been counted as explained in the beginning of this Section. It is important to note that in HSD the high energy density is essentially build up from ‘strings’, i.e. ‘unformed’ hadrons. The absolute numbers in Fig. 9 have to be compared to the volume of a Au-nucleus in the moving frame which – for a Lorentz  $\gamma$ -factor of 3.78 – gives  $\approx 330$  fm<sup>3</sup>. In this case, the overlap phase of the nuclei



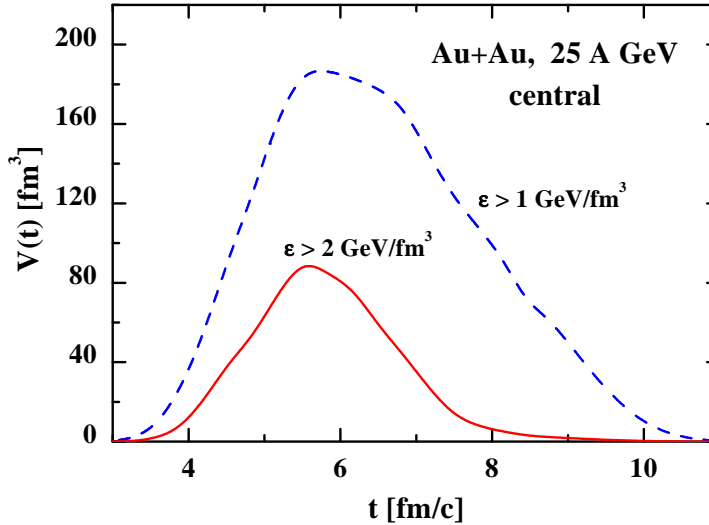


Fig. 9. Time evolution for the volume with energy density  $\varepsilon \geq 1 \text{ GeV/fm}^3$  (dashed line) and  $\geq 2 \text{ GeV/fm}^3$  (solid line) in the HSD approach for a central  $Au + Au$  reaction at 25 A·GeV. The figure is taken from Ref. 33.

lasts for about 3.7 fm/c during which energy densities above  $2 \text{ GeV/fm}^3$  are seen in Fig. 9 in a sizeable volume. Thus also at 25 A·GeV the phase boundary to a QGP might be probed in a sizeable volume for time scales of a few fm/c. Contrary to central collisions at the SPS and RHIC, these volumes are characterized by a high net quark density; for such configurations we presently have only ‘hints’ from lattice QCD calculations rather than solid information.

#### 4. Proton-nucleus reactions: Cold nuclear matter effects

Before coming to charm production and propagation in heavy-ion reactions it is mandatory to explore the charm dynamics in proton-nucleus reactions. Such reactions are a first step beyond the elementary  $pp$  reactions and provide an additional reference with respect to the heavy-ion case. Since in  $p+A$  reactions only subnormal nuclear densities are achieved and the target nucleus remains approximately in its geometrical shape for the first few fm/c, these reactions are much easier to treat and allow to separate ‘cold nuclear matter’ (CNM) effects from those induced by the new partonic medium encountered in relativistic nucleus-nucleus collisions. As we will show in the following, one can observe e.g. gluon shadowing at RHIC energies by its influence on charmonium production in  $d + Au$  collisions. Additionally, the amount of ‘normal’ nuclear charmonium dissociation by the target nucleons can be probed. Thus  $p + A$  reactions provide a necessary base-line for the heavy-ion case and can independently be controlled by experimental data.

It is found experimentally that the yield of  $J/\Psi$  in  $p + A$  and  $A + A$  reactions

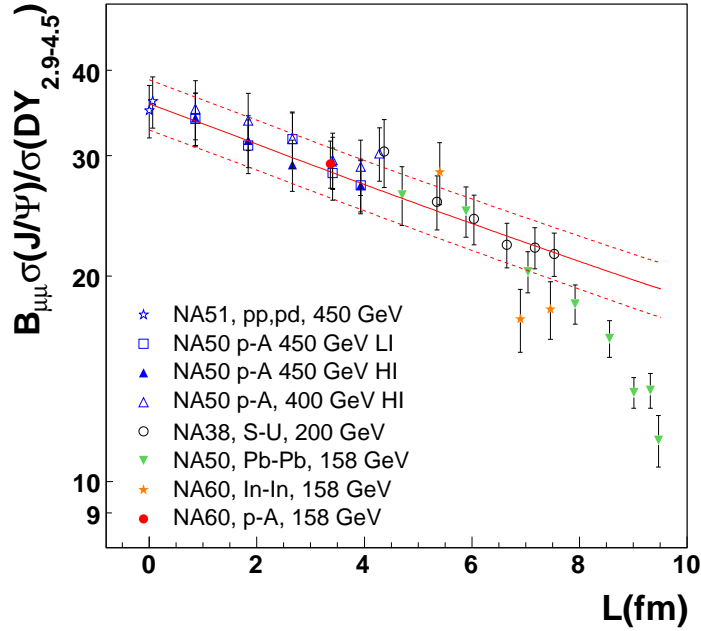


Fig. 10. The ratio  $\sigma_{J/\psi}/\sigma_{DY}$  (times the branching ratio  $B_{\mu\mu}$ ) measured in p-A and nucleus-nucleus collisions at the SPS, compiled and re-scaled, when necessary, to 158 GeV incident energy by the NA60 Collaboration. The quantity  $L$  denotes the effective path length of the  $J/\Psi$  as extracted within the Glauber model. The lines indicate the results of a Glauber fit to the p-A data and the size of the error as calculated by the NA60 Collaboration. The figure is taken from Ref. <sup>4</sup>.

is modified compared to that in  $p + p$  collisions - scaled with the number of initial binary scatterings  $N_{coll}$  <sup>5,97</sup>. Indeed, the produced  $c\bar{c}$  can be dissociated or absorbed on either the residual nucleons of the projectile or target or on light co-moving particles (usually on mesons or, at high energy, on partons) produced in the very early phase. Alternatively, the initial production of  $c\bar{c}$  pairs by gluon fusion might be suppressed due to shadowing (at RHIC energies). In particular, charmonium absorption on *baryons* is the leading suppression mechanism in  $d + A$  ( $p + A$ ) scattering at SPS energies and is an important base-line for the investigation of charmonium absorption.

#### 4.1. SPS energies

The NA50 and NA60 Collaborations present their results on  $J/\Psi$  suppression as the ratio of the dimuon decay of the  $J/\Psi$  relative to the Drell-Yan background from 2.9 - 4.5 GeV invariant mass as a function of the transverse energy  $E_T$ , or alternative, as a function of the number of participants  $N_{part}$ , *i.e.*

$$B_{\mu\mu}\sigma(J/\Psi)/\sigma(DY)|_{2.9-4.5}, \quad (7)$$

where  $B_{\mu\mu}$  is the branching ratio for  $J/\Psi \rightarrow \mu^+\mu^-$ . In order to compare our calculated results to experimental data (see below) we need an extra input, i.e. the normalization factor  $B_{\mu\mu}\sigma_{NN}(J/\Psi)/\sigma_{NN}(DY)$ , which defines the  $J/\Psi$  over Drell-Yan ratio for elementary nucleon-nucleon collisions. We will adopt  $B_{\mu\mu}\sigma_{NN}(J/\Psi)/\sigma_{NN}(DY) = 36$  in line with the NA60 compilation<sup>5</sup> (at the SPS energy of 158 GeV).

In Fig. 10 we show the combined  $p + A$ ,  $S + U$ ,  $Pb + Pb$  and  $In + In$  data (from NA50 and NA60) for the ratio  $B_{\mu\mu}\sigma(J/\Psi)/\sigma(DY)$  at 158 A·GeV as a function of centrality - reflected in the effective path length  $L$  - together with the Glauber-model fit by the NA50/60 collaboration. The ‘default’ interpretation of the experimental results in Fig. 10 is that for a  $J/\Psi$  path length  $L$  below about 7 fm dominantly ‘normal’  $J/\Psi$  dissociation with target nucleons is seen while for  $L > 7$  fm an ‘anomalous’ suppression sets in. Since this ‘anomalous’ suppression only is observed in central  $In + In$  and  $Pb + Pb$  collisions it is attributed to a ‘hot matter’ effect in contrast to the ‘normal’ absorption (‘cold nuclear matter’ effect). However, in order to distinguish more clearly such ‘hot’ and ‘cold nuclear’ matter effects it is mandatory to employ non-equilibrium transport.

In order to study the effect of charmonium rescattering on projectile/target nucleons, we adopt in HSD the following dissociation cross sections of charmonia with baryons independent of the energy (in line with the most recent NA50 and NA60 compilations<sup>5,98</sup>):

$$\begin{aligned}\sigma_{c\bar{c}B} &= 4.18 \text{ mb}; \\ \sigma_{J/\Psi B} &= 4.18 \text{ mb}; \quad \sigma_{\chi_{cB}} = 4.18 \text{ mb}; \quad \sigma_{\Psi'B} = 7.6 \text{ mb}.\end{aligned}\tag{8}$$

The applicability of the Glauber picture to the baryon-induced suppression (at  $L < 7$  fm) as illustrated in Fig. 10 suggests that the produced  $c\bar{c}$  pair can be absorbed on baryons already in its pre-resonant state. In (8) the cross section  $\sigma_{c\bar{c}B}$  stands for a (color dipole) pre-resonance ( $c\bar{c}$ ) - baryon cross section, since the  $c\bar{c}$  pair produced initially cannot be identified with a particular charmonium due to the uncertainty relation in energy and time. For the life-time of the pre-resonance  $c\bar{c}$  pair (in its rest frame) a value of  $\tau_{c\bar{c}} = 0.3$  fm/c is assumed following Ref. 99. This time scale corresponds to the mass difference of the  $\Psi'$  and  $J/\Psi$  according to the uncertainty relation. Note that - in contrast to the absorption on primordial baryons  $B$  (nucleons of the incoming nuclei) - interactions with secondary particles created in the nucleus-nucleus collision (mesons or secondary baryons) are only allowed after the local energy-density has dropped below 1 GeV/fm<sup>3</sup> in order to assure that the interaction is hadronic.

In Fig. 11 we present the results of the HSD calculations for the observable (7) for Pb+Pb and In+In collisions in the nuclear suppression scenario, *i.e.* with only baryonic absorption and no additional, meson- or parton-induced suppression. Instead of the (model-dependent) path length  $L$  we display this ratio as a function of the number of participants  $N_{part}$ , which can directly be taken from the transport calculations. The dashed (blue) lines stand for the HSD results while the (green-

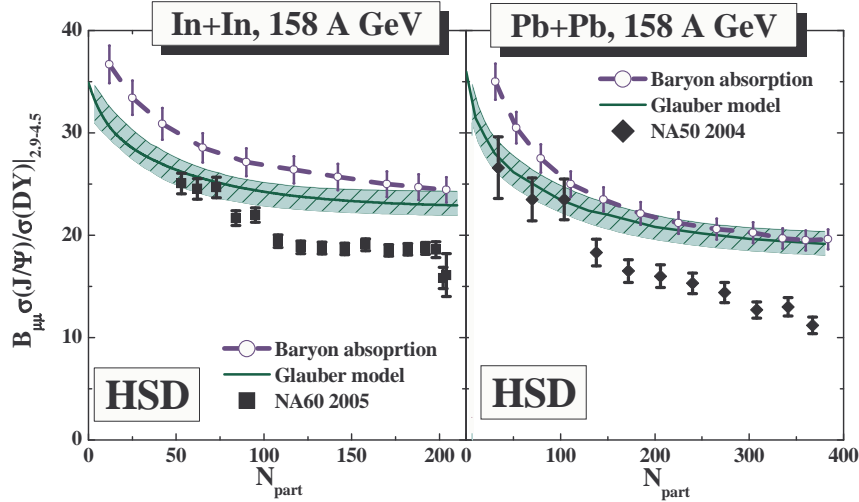


Fig. 11. The ratio  $B_{\mu\mu}\sigma(J/\Psi)/\sigma(DY)_{2,9-4.5}$  as a function of the number of participants in In+In (l.h.s.) and Pb+Pb reactions (r.h.s.) at 158 A-GeV. The full symbols denote the data from the NA50 and NA60 Collaborations (from Refs. 4,5,100), while the dashed (blue) lines represent the HSD calculations including only dissociation channels with nucleons. The (dashed blue-green) bands in the upper parts of the figure give the estimate for the normal nuclear  $J/\Psi$  absorption as calculated by the NA60 Collaboration. The vertical lines on the graphs reflect the theoretical uncertainty due to limited statistics of the calculations. The figure is taken from Ref. 44.

blue) bands give the estimate for the normal nuclear  $J/\Psi$  absorption as calculated by the NA60 Collaboration in the Glauber model<sup>4</sup>. The normal nuclear suppression from HSD is seen to be slightly lower than the (model dependent) estimate from NA60, however, agrees quite well with their calculations for more central reactions. The various experimental data points have been taken from Refs. 4,5,100.

Apart from the statistical uncertainties in the calculations – reflected by the vertical lines on the theoretical graphs in Fig. 11 – some dependence on the model parameters enters the actual numbers in Fig. 11. The charmonium nuclear absorption cross section is considered to be ‘fixed’ by the NA50/NA60 compilations and we have taken the same cross section for the ‘pre-resonance’ cross section for the  $J/\Psi$  and  $\chi_c$ . Accordingly, the life-time of the pre-resonance state ( $\tau_{c\bar{c}} = 0.3$  fm/c) has no impact on the absorption with baryons as far as the  $J/\Psi$  and  $\chi_c$  mesons are concerned. Only for  $\Psi'$  collisions with baryons this plays a role, since the  $\Psi' +$  baryon cross section is larger (7.6 mb). Consequently, the  $J/\Psi$  suppression (including the feed down from  $\chi_c$ ) does not depend on  $\tau_{c\bar{c}}$ . Within these systematic uncertainties we will now be able to separate ‘cold nuclear’ and ‘hot’ matter effects in relativistic nucleus-nucleus collisions at SPS energies.

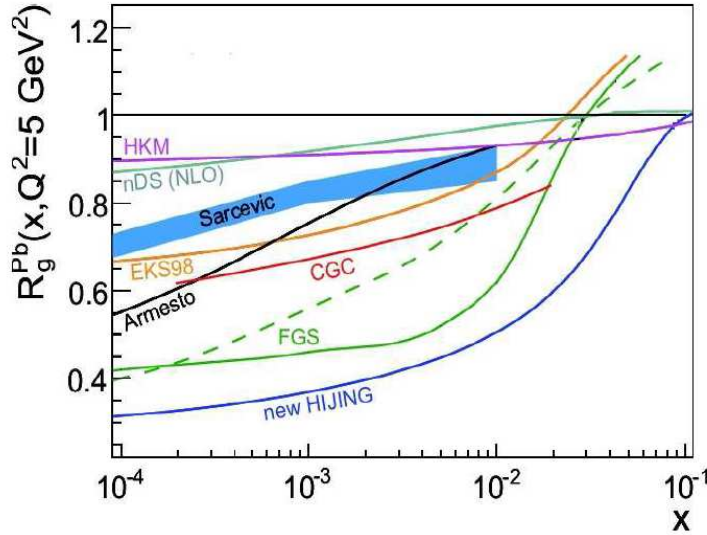


Fig. 12. Ratio of gluon densities in lead nucleus and in proton as a function of Bjorken  $x$  at a fixed hard scale  $Q^2 = 5 \text{ GeV}^2$  from various parton distribution fits. The figure is taken from Ref. <sup>101</sup>.

#### 4.2. RHIC energies

The cross sections  $\sigma_{J/\Psi N}, \sigma_{c\bar{c}N}$  at RHIC energies are currently debated in the literature. On one side, all the data on  $J/\Psi$  production in  $p + A$  reactions at energies  $\sqrt{s} \leq 40 \text{ GeV}$  are found to be consistent with an energy-independent cross section of the order of  $4 - 7 \text{ mb}$  <sup>5,98,102,103,104</sup>; on the other hand, at the much higher energy of  $\sqrt{s} = 200 \text{ GeV}$  some part of the suppression might be attributed to other (initial-state) ‘cold nuclear matter’ effects such as gluon shadowing <sup>105,106,107</sup>, radiative gluon energy loss in the initial state or multiple gluon rescattering <sup>108,109,110</sup>. We recall that ‘shadowing’ is a depletion of the low-momentum parton distribution in a nucleon embedded in a nucleus compared to the population in a free nucleon; this also leads to a lowering in the (scaled) charmonium production cross section in  $p + A$  relative to  $pp$  reactions. The reasons for depletion, though, are numerous, and models of shadowing vary accordingly. There is, therefore, a considerable (about a factor of 3) uncertainty in the amount of shadowing predicted at RHIC <sup>105,106,107,111,112</sup>. Indeed, there is currently a lack of precise differential data, which would allow to constrain the gluon distribution in nuclei at low Bjorken  $x$ ; this region is probed by charmonium production by gluon fusion processes. Fig. 12 shows an overview of the various model concepts which demonstrates that at low Bjorken  $x$  (of the order of  $10^{-2}$ - $10^{-4}$ ) the nuclear gluon distribution function has large uncertainties.

In the analysis of the  $d + Au$  data at  $\sqrt{s} = 200 \text{ GeV}$ , in which the maximum estimate for the effect of shadowing was made <sup>107,118</sup>, the additional absorption

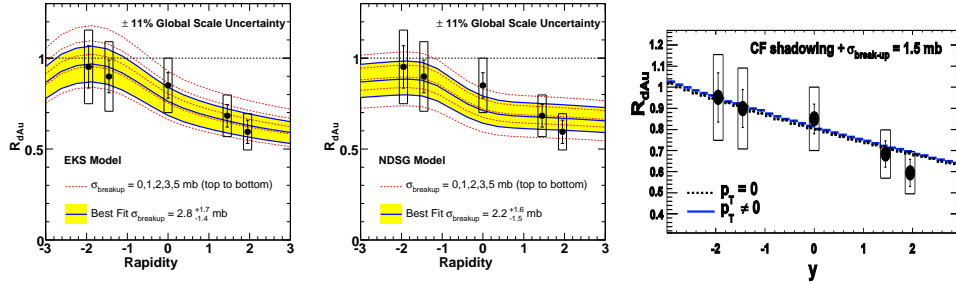


Fig. 13. The  $J/\psi$  nuclear modification factor in  $d + Au$  collisions at  $\sqrt{s} = 200$  GeV as a function of rapidity<sup>113</sup> compared with calculations including shadowing on top of the Glauber model nuclear absorption with an adjusted  $J/\psi N$  breakup cross section. Left panel: the data are compared with calculations<sup>107</sup> using the EKS98 parameterization<sup>114,115</sup> of shadowing. Middle panel: same as the left panel, but the calculations<sup>107</sup> employ the nDSg shadowing parameterization<sup>116</sup>. Right panel: the calculations<sup>117</sup> employ the CF picture of shadowing<sup>107,109,110,108</sup>. The figures are taken from Refs.<sup>67,117</sup>.

on baryons allowed by the data was found to lead to  $\sigma_{J/\psi N} = 1 - 3$  mb or higher, if some contribution of anti-shadowing is present. The authors of Ref.<sup>107</sup> advocate at least  $\sigma_{J/\psi N} = 3$  mb in order to preserve the agreement with the data of the Fermilab experiment E866. The PHENIX Collaboration<sup>113</sup> finds a breakup cross section of  $2.8^{+1.7}_{-1.4}$  mb (using EKS shadowing) which still overlaps with the CERN-SPS value of 4.18 mb (though with large error bars).

Fig. 13 demonstrates the variation in the rapidity dependence and the amount of initial state interaction between different implementations of shadowing for the nuclear modification factor defined as

$$R_{dA} \equiv \frac{dN_{J/\psi}^{dAu}/dy}{\langle N_{coll} \rangle \cdot dN_{J/\psi}^{pp}/dy}. \quad (9)$$

In Eq. (9)  $dN_{J/\psi}^{dAu}/dy$  is the  $J/\psi$  invariant yield in  $d + A$  collisions,  $dN_{J/\psi}^{pp}/dy$  is the  $J/\psi$  invariant yield in  $p + p$  collisions;  $\langle N_{coll} \rangle$  is the average number of binary collisions for the same rapidity bin ( $\langle N_{coll} \rangle = 7.6 \pm 0.3$  according to the PHENIX estimate<sup>113</sup>). There is an additional large theoretical uncertainty in the results shown in Fig. 13 since in the works above only an approximate model for baryonic absorption was applied and not a microscopic transport approach that e.g. also includes secondary production channels of charm pairs as described in Section 2.

We continue our investigation of ‘cold nuclear matter’ effects at RHIC energies for  $d + Au$  reactions employing the same cross sections for baryonic absorption (8) as at SPS energies (cf. Fig. 11). In Fig. 14 we compare the HSD result (neglecting shadowing) for the  $J/\psi$  production in  $d + Au$  collisions at  $\sqrt{s} = 200$  GeV to the PHENIX data<sup>113</sup>. It is seen from Fig. 14 that the calculations follow approximately the decrease in  $R_{dA}$  with rapidity, however, with a tendency to overshoot at forward rapidity. Within error bars we find the values of  $\sigma_{c\bar{c}B}$  from (8) to be compatible with

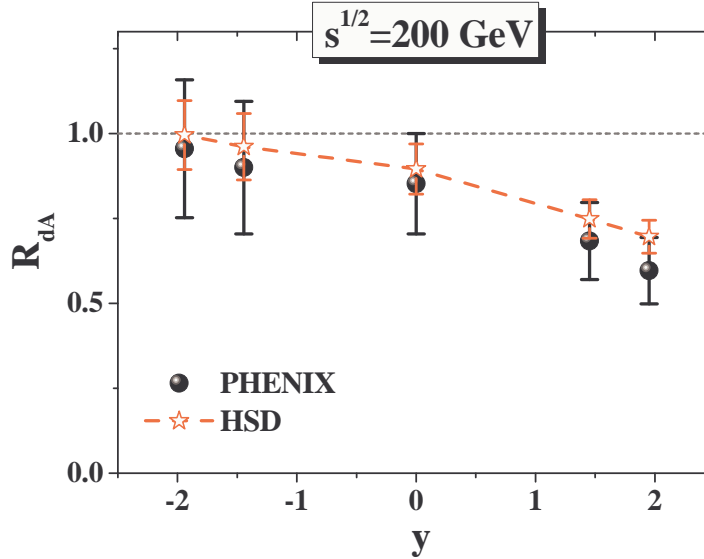


Fig. 14.  $J/\Psi$  production cross section in  $d + Au$  collisions relative to that in  $p + p$  collisions (see text for the definition of  $R_{dA}$ ) in HSD (red stars) – neglecting gluon shadowing – as compared to the PHENIX data <sup>113</sup> (full dots). The figure is taken from Ref. <sup>82</sup>.

the inclusive RHIC measurement as well as with the lower energy data <sup>102</sup>. This finding is also in line with the analysis of the PHENIX Collaboration in Ref. <sup>113</sup>.

In order to shed some further light on the role of shadowing, we compare our calculations for  $R_{dA}$  in different rapidity bins as a function of the centrality of the  $d + Au$  collision, which in Fig. 15 is represented by the number of binary collisions  $N_{coll}$ . The latter number is directly taken from the number of binary hard  $NN$  collisions in the transport calculation while the comparison with experiment is based on a Glauber model analysis of the data similar to that performed in Ref. <sup>119</sup>. The actual results displayed in Fig. 15 (stars connected by dashed lines) and the PHENIX data from Ref. <sup>113</sup> are roughly compatible for the rapidity intervals  $-2.2 < y < -1.2$  and  $|y| < 0.35$ , but demonstrate that the suppression at forward rapidity ( $1.2 < y < 2.2$ ) is underestimated in the color-dipole dissociation model with a constant cross section of 4.18 mb. This clearly points to the presence of shadowing effects at least at forward rapidities which is not so pronounced in the inclusive data set in Fig. 14. A more serious question is a quantification of the shadowing, which is extremely challenging because of the limited statistics of both the experimental data and the calculations. Here we do not attempt to attribute a fixed number for the shadowing effect but merely point out that independent high statistics data will be necessary to fix this unsatisfactory situation from the experimental side.

Nevertheless, some note of caution is appropriate for the further analysis of char-



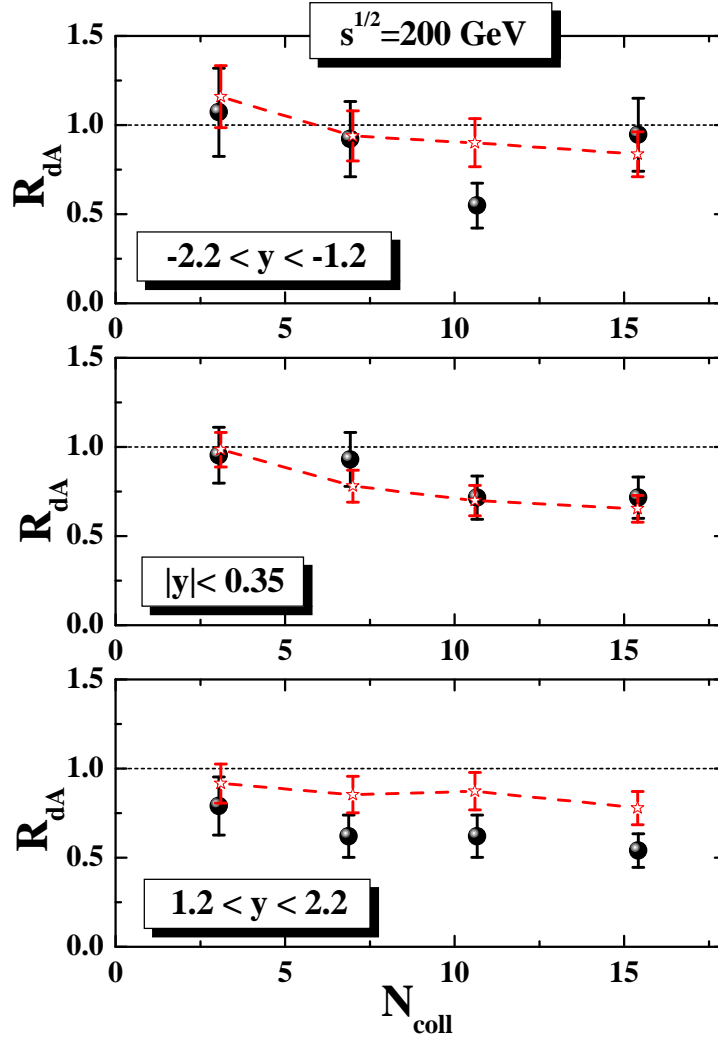


Fig. 15. The ratio  $R_{dA}$  (9) for backward, central and forward rapidity bins as a function of the number of binary collisions  $N_{coll}$  for  $d + Au$  at  $\sqrt{s} = 200 \text{ GeV}$ . The experimental data have been taken from Ref. 113. The HSD results (stars connected by red dashed lines) show calculations without including low- $x$  gluon shadowing and slightly overestimate  $R_{dA}$  in the forward interval  $1.2 < y < 2.2$ . The theoretical error bars are due to the finite statistics of the calculation. The figure is taken from Ref. 82.

monium suppression in  $Au + Au$  collisions: There are ‘cold nuclear matter effects’ such as ‘gluon shadowing’ beyond those incorporated in the HSD transport calculations, and especially quantitative statements about any ‘agreement with data’ might have to be reconsidered. In case of  $Au + Au$  reactions the shadowing from projectile/target will show up symmetrically around  $y = 0$  and in part contribute

to the stronger  $J/\Psi$  suppression at forward/backward rapidities. Nevertheless, following Granier de Cassagnac<sup>119</sup>, an anomalous suppression of  $J/\Psi$  beyond ‘cold nuclear matter’ effects is clearly present in the  $Au + Au$  data (to be investigated below).

### 4.3. FAIR energies

At FAIR energies shadowing is not expected to show any sizeable effect (as at SPS energies). Accordingly, the charmonium suppression will be driven by dissociation reactions with baryons, mesons etc. as will be discussed in Section 6. As we will see in Subsection 7.5, HSD predicts that the dissociation on nucleons will actually be the leading mechanism for  $J/\Psi$  suppression at FAIR energies.

## 5. Hadron abundances from heavy-ion collisions

We here recall the information gained from previous experimental (and theoretical) studies on hadron production in heavy-ion reactions. A general overview on the experimental meson and strange baryon abundances from central nucleus-nucleus collisions ( $Au+Au$  or  $Pb+Pb$ ) is given in Fig. 16, which shows the meson abundances from central  $Au+Au$  reactions as predicted by HSD transport calculations in 2000<sup>33</sup> from SIS to RHIC energies. The experimental data at AGS (dots), SPS (squares) and RHIC energies (triangles) have been added recently. All meson multiplicities show a monotonic increase with bombarding energy which is only very steep at ‘subthreshold’ energies, i.e. at bombarding energies per nucleon below the threshold in free space for  $NN$  collisions. Note that the HSD transport results are also in a fair agreement with results from the UrQMD transport approach and data (from AGS to RHIC energies) for the hadron rapidity distributions<sup>56</sup>. Only in case of transverse mass spectra both transport approaches underestimate the experimental slopes from lower SPS to RHIC energies<sup>66</sup>.

Some comments with respect to the charm production in heavy-ion reactions are in order: The mass of the  $J/\Psi$  - for the states of interest here - gives the lowest scale of 3.097 GeV. Accordingly, the formation of a  $J/\Psi$  from an initial  $c\bar{c}$  pair is the only allowed process (in vacuum) close to the charm threshold, because the  $D + \bar{D}$  channel, i.e.  $N + N \rightarrow D + \bar{D} + N + N$ , has an effective invariant mass of 3.739 GeV. The associated production of a  $D(\bar{c})$  meson with a charmed hyperon  $\Lambda_c(\Sigma_c)$ , i.e.  $N + N \rightarrow \Lambda_c + D + N$ , is more favorable due to effective invariant mass of 3.216 GeV (3.386 GeV), which is lower than for the production of a  $D\bar{D}$  pair. This explains, why in Fig. 16 the  $D(\bar{c})$  cross section is larger than the  $D(c)$  cross section close to threshold energies, and the  $J/\Psi$  formation dominates in the far subthreshold domain. At higher bombarding energies the meson abundances group according to their quark content, i.e. the multiplicities are reduced (relative to  $\pi^+$ ) by about a factor of 5 for a strange quark, a factor of  $\approx 2 \cdot 5^2 = 50$  for  $s\bar{s} \equiv \phi$ , a factor of  $\approx 100$  for  $D (\bar{D})$ , and  $\approx 2 \cdot 10^4$  for  $c\bar{c} \equiv J/\Psi$ .

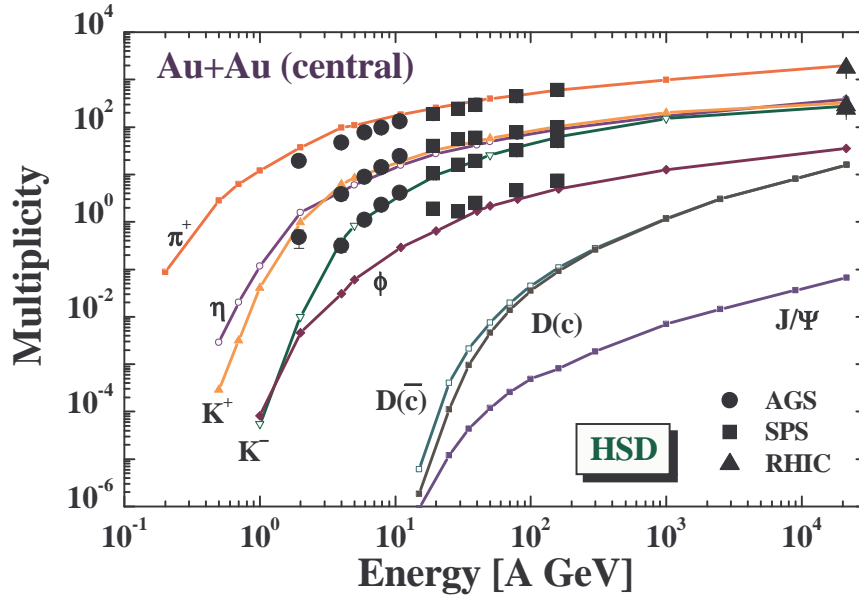


Fig. 16. Overview on the experimental meson abundances and HSD predictions for the multiplicities of  $\pi^+$ ,  $\eta$ ,  $K^+$ ,  $K^-$ ,  $\phi$ ,  $D$ ,  $\bar{D}$  and  $J/\Psi$ -mesons for central collisions of Au+Au as a function of bombarding energy from SIS to RHIC energies. The figure is taken from Ref. <sup>33</sup> while the experimental data have been added recently.

According to the arguments given above the  $\bar{D}$ -mesons with a  $\bar{c}$  are produced more frequently at low energies (due to an associated baryon  $\Lambda_c, \Sigma_c$ ). At roughly 15 A·GeV the cross sections for open charm and charmonia are expected to be of similar magnitude, while at higher energies the ratio of open charm to charmonium bound states increases rapidly with energy. Since the excitation function for open charm drops very fast with decreasing bombarding energy, experiments around 25 A·GeV, *e.g.* at the future FAIR facility <sup>9</sup>, will be a challenging task, because the multiplicity of the other mesons is higher by orders of magnitude.

In the statistical hadronization model of Ref. <sup>120</sup> the production of  $c\bar{c}$  pairs is assumed to proceed by hard initial nucleon-nucleon scattering - as in HSD - but the redistribution of charm quarks and antiquarks in the hadronization process is assumed to follow statistical laws determined by a chemical freeze-out temperature  $T_{cfr}$  and the baryon chemical potential  $\mu_B$ . The latter parameters are taken from the experimental systematics of the chemical freeze-out line in the  $(T, \mu_B)$  diagram <sup>120</sup>. The resulting energy dependence of charmed hadron production in heavy-ion collisions (at midrapidity) is displayed in Fig. 17, where the absolute yields are shown on the l.h.s. whereas the yields relative to the number of  $c\bar{c}$  pairs produced are given in the right panel. Note (in both panels) the scale factors of 10 and 100 for  $J/\Psi$  and  $\Psi'$  mesons, respectively. The relative ratios of charmed baryons to charmed mesons differ significantly from those in the HSD approach

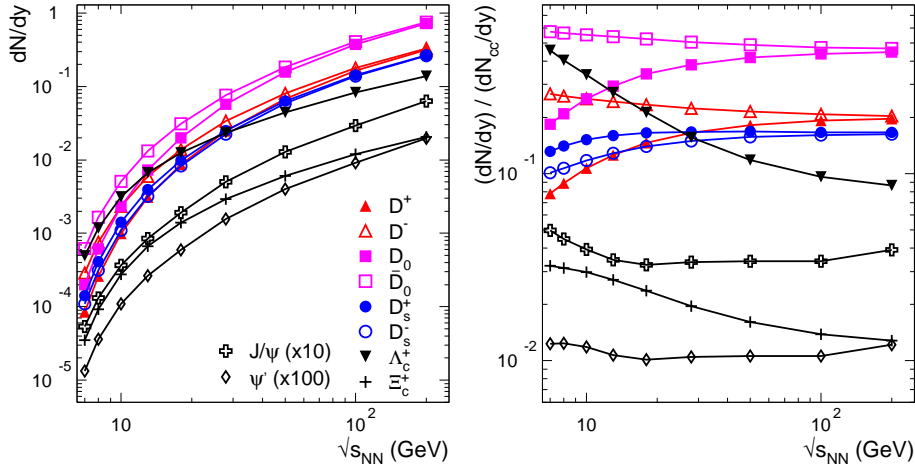


Fig. 17. Energy dependence of charmed hadron production in heavy-ion collisions at midrapidity in the statistical hadronization model of Ref. <sup>120</sup>. Left panel: absolute yields, right panel: yields relative to the number of  $c\bar{c}$  pairs. Note (in both panels) the scale factors of 10 and 100 for  $J/\Psi$  and  $\Psi'$  mesons, respectively. The figure is taken from Ref. <sup>121</sup>.

where full chemical equilibrium is not achieved in the charm sector (cf. Section 8). On the other hand it is unknown whether the statistical model is applicable to the charm sector in the FAIR energy range (particularly for non-central collisions). Future experiments at FAIR are expected to clarify this issue.

As pointed out in Ref. <sup>122</sup>, dropping  $D$ ,  $\bar{D}$  masses with baryon density (and/or temperature) might lead to an increase of  $J/\Psi$  absorption and to a net lowering of the  $\Psi'/J/\Psi$  ratio for central collisions. Thus the  $\Psi'/J/\Psi$  ratio could also qualify as a probe of  $D$ -meson in-medium effects. On the other hand, medium modification of  $D$ -mesons is more complex than a simple picture of dropping masses suggests. Microscopic G-matrix studies indicate that the drop of the  $D$ -meson masses with baryon density is only very moderate and as a leading effect one should expect a spectral broadening <sup>123,124</sup>.

Note, however, that the elementary cross sections for open charm and charmonia in  $pp$  and  $\pi N$  reactions have to be measured in the relevant kinematical regimes before reliable conclusions can be drawn about charm dynamics in the nucleus-nucleus case. Experimental data in the 20 - 30 A·GeV with light and heavy systems will have to clarify, furthermore, if the quasi-particle picture of open charm mesons at high baryon density is applicable at all or if the dynamics is already governed by partonic degrees of freedom rather than hadronic ones (see below).

The production of ‘ordinary’ hadrons (with ‘u,d,s’ flavor) as well as open charm and charmonium at SPS and RHIC energies has been calculated so far within the AMPT<sup>125</sup>, HSD<sup>33,47,126</sup> and UrQMD<sup>127</sup> transport approaches using

parametrizations for the elementary production channels as described in Section 2. Backward channels ‘charm + anticharm meson  $\rightarrow$  charmonia + meson’ are treated in HSD via detailed balance in a schematic interaction model with a single matrix element  $|M|^2$  that is fixed by the  $J/\Psi$  suppression data from the NA50 collaboration<sup>128</sup> at SPS energies (cf. Ref.<sup>47</sup> and Section 6.1). The independent transport approaches provide in general very similar results for energy densities, baryon densities, meson densities etc. such that the bulk dynamics of relativistic nucleus-nucleus collisions is known to a sufficient extent (cf. Ref.<sup>19</sup> for a more detailed comparison).

## 6. Anomalous suppression of $J/\Psi$ : The basic models

In the past, the charmonia  $J/\Psi$ ,  $\chi_c$ ,  $\Psi'$  have been discussed in context of the phase transition to the QGP, since  $c\bar{c}$  states might no longer be formed due to color screening<sup>26</sup>. However, more recent calculations within lattice QCD (lQCD) have shown that at least the  $J/\Psi$  survives up to  $\sim 1.5 T_c$  ( $T_c \approx 0.17 - 0.19$  GeV) such that the lowest  $c\bar{c}$  states remain bound up to energy densities of about 5 GeV/fm<sup>3</sup> (see Refs.<sup>129,130</sup>). It is presently not clear, if also the  $D$  or  $D^*$  mesons survive at temperatures above  $T_c$ , but strong correlations between a light quark (antiquark) and a charm antiquark (quark) are likely to persist. One may speculate that similar correlations survive also in the light quark sector above  $T_c$ , such that ‘pre-hadronic comovers’ - most likely with different spectral functions - might show up also at energy densities above 1 GeV/fm<sup>3</sup>, which is taken as a characteristic scale for the critical energy density.

On the other hand, it is well known that the baryonic (normal) absorption alone cannot explain the suppression of charmonia in heavy-ion collisions with increasing centrality<sup>131</sup> (cf. Fig. 11). Different mechanism for the additional (anomalous) suppression or formation of charmonia have been suggested in the past, i.e. charmonia might be ‘melting’ according to the scenario advocated in Ref.<sup>26</sup> (their formation be suppressed due to plasma screening<sup>132</sup>), absorbed on co-moving mesons in hot hadronic matter<sup>112,133</sup> or they could be absorbed early by neighboring strings<sup>87</sup>. Moreover, charmonia might also be generated in a statistical fashion at the phase boundary between the QGP and an interacting hadron gas such that their abundance could be in statistical (chemical) equilibrium with the light and strange hadrons as suggested in Refs.<sup>134,135</sup>. The latter picture is expected to lead not to a suppression but to an enhancement of  $J/\Psi$  mesons at the full RHIC energy if compared to the scaled  $J/\Psi$  multiplicity from  $pp$  collisions<sup>136</sup>.

### 6.1. ‘Comover’ suppression (and recombination)

First of all let us stress that the interactions with ‘comoving’ mesons lead not only to the dissociation of charmonia, but also to their recreation via the inverse recombination process  $D + \bar{D} \rightarrow c\bar{c} + m$ , where  $m = \{\pi, \rho, \omega, K, \dots\}$ . As already pointed out before, the  $J/\Psi$ ,  $\chi_c$ ,  $\Psi'$  formation cross sections by open charm mesons or the inverse ‘comover’ dissociation cross sections are not well known and the significance of these

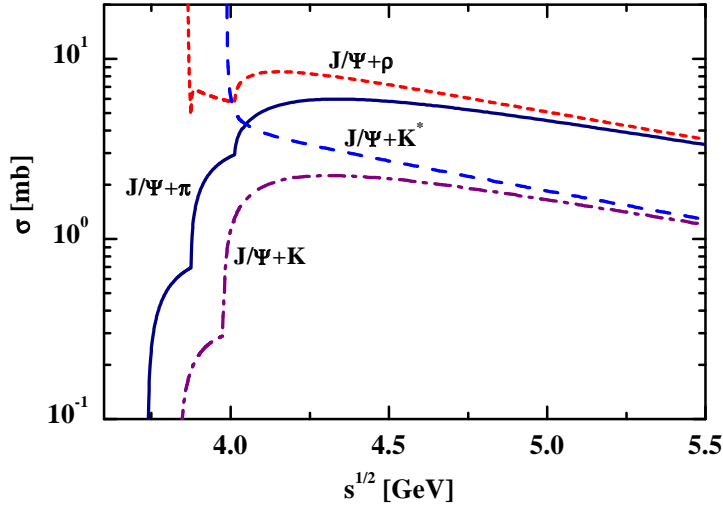


Fig. 18. The  $J/\Psi$  dissociation cross sections with  $\pi$ ,  $\rho$ ,  $K$  and  $K^*$  mesons as specified in the text (Eqs. (10)-(12)).

channels is discussed controversially in the literature <sup>132,137,136,138,139,140,141</sup>. In HSD – following the concept of Refs. <sup>47,48</sup> – a simple 2-body transition model is employed with a single parameter  $|M_0|^2$  that allows to implement the backward reactions uniquely by exploiting detailed balance for each individual channel. We briefly review this concept in the following.

Since the charmonium-meson dissociation and backward reactions typically occur with low relative momenta (‘comovers’), it is legitimate to write the cross section for the process  $1 + 2 \rightarrow 3 + 4$  as

$$\sigma_{1+2 \rightarrow 3+4}(s) = 2^4 \frac{E_1 E_2 E_3 E_4}{s} |\tilde{M}_i|^2 \left( \frac{m_3 + m_4}{\sqrt{s}} \right)^6 \frac{p_f}{p_i}, \quad (10)$$

where  $E_k$  denotes the energy of hadron  $k$  ( $k = 1, 2, 3, 4$ ), respectively. The initial and final momenta for fixed invariant energy  $\sqrt{s}$  are given by

$$\begin{aligned} p_i^2 &= \frac{(s - (m_1 + m_2)^2)(s - (m_1 - m_2)^2)}{4s}, \\ p_f^2 &= \frac{(s - (m_3 + m_4)^2)(s - (m_3 - m_4)^2)}{4s}, \end{aligned} \quad (11)$$

where  $m_k$  denotes the mass of hadron  $k$ . In (10)  $|\tilde{M}_i|^2$  ( $i = \chi_c, J/\Psi, \Psi'$ ) stands for the effective matrix element squared, which for the different 2-body channels is

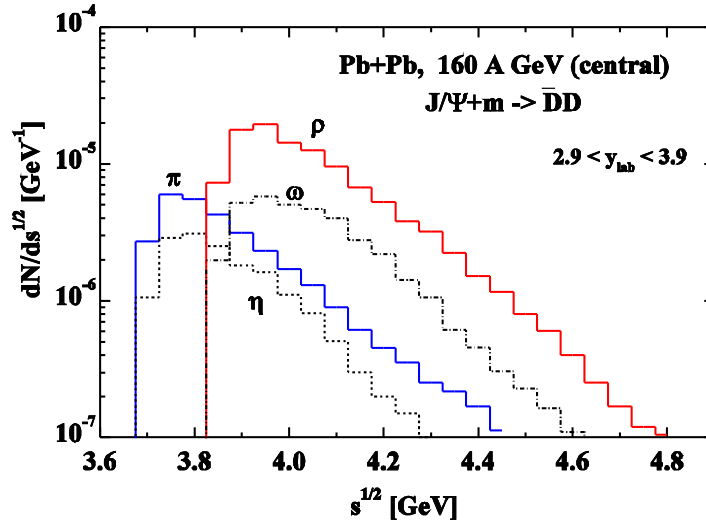


Fig. 19. The distribution in the invariant collision energy  $\sqrt{s}$  for  $J/\Psi$  absorption on  $\pi^-$ ,  $\eta^-$ ,  $\rho^-$  and  $\omega$ -mesons in central ( $b = 2$  fm) Pb + Pb collisions at 160 A-GeV within the HSD transport approach. The figure is taken from Ref. <sup>36</sup>.

taken of the form

$$\begin{aligned}
 |\tilde{M}_i|^2 &= |M_i|^2 \text{ for } (\pi, \rho) + (c\bar{c})_i \rightarrow D + \bar{D} & (12) \\
 |\tilde{M}_i|^2 &= 3|M_i|^2 \text{ for } (\pi, \rho) + (c\bar{c})_i \rightarrow D^* + \bar{D}, D + \bar{D}^*, D^* + \bar{D}^* \\
 |\tilde{M}_i|^2 &= \frac{1}{3}|M_i|^2 \text{ for } (K, K^*) + (c\bar{c})_i \rightarrow D_s + \bar{D}, \bar{D}_s + D \\
 |\tilde{M}_i|^2 &= |M_i|^2 \text{ for } (K, K^*) + (c\bar{c})_i \rightarrow D_s + \bar{D}^*, \bar{D}_s + D^*, D_s^* + \bar{D}, \\
 &\quad \bar{D}_s^* + D, \bar{D}_s^* + D^*
 \end{aligned}$$

The relative factors of 3 in (12) are guided by the sum rule studies in Ref. <sup>142</sup> which suggest that the cross section is increased whenever a vector meson  $D^*$  or  $\bar{D}^*$  appears in the final channel while another factor of 1/3 is introduced for each  $s$  or  $\bar{s}$  quark involved. The factor  $((m_3 + m_4)/\sqrt{s})^6$  in (10) accounts for the suppression of binary channels with increasing  $\sqrt{s}$  and has been fitted to the experimental data for the reactions  $\pi + N \rightarrow \rho + N, \omega + N, \phi + N, K^+ + \Lambda$  in Ref. <sup>143</sup>.

We use the same matrix elements for the dissociation of all charmonium states  $i$  ( $i = \chi_c, J/\Psi, \Psi'$ ) with mesons:

$$|M_{J/\Psi}|^2 = |M_{\chi_c}|^2 = |M_{\Psi'}|^2 = |M_0|^2. \quad (13)$$

The best fit for  $|M_0|^2$  (in comparison to the latest NA50 and NA60 analysis <sup>5,98</sup>) is obtained for  $|M_0|^2 = 0.18 \text{ fm}^2/\text{GeV}^2$  <sup>44</sup>; this value will be employed in the HSD calculations for all bombarding energies and systems.

The resulting  $J/\Psi$  dissociation cross sections with  $\pi, \rho, K$  and  $K^*$  mesons are displayed in Fig. 18. The final state includes all binary channels compatible



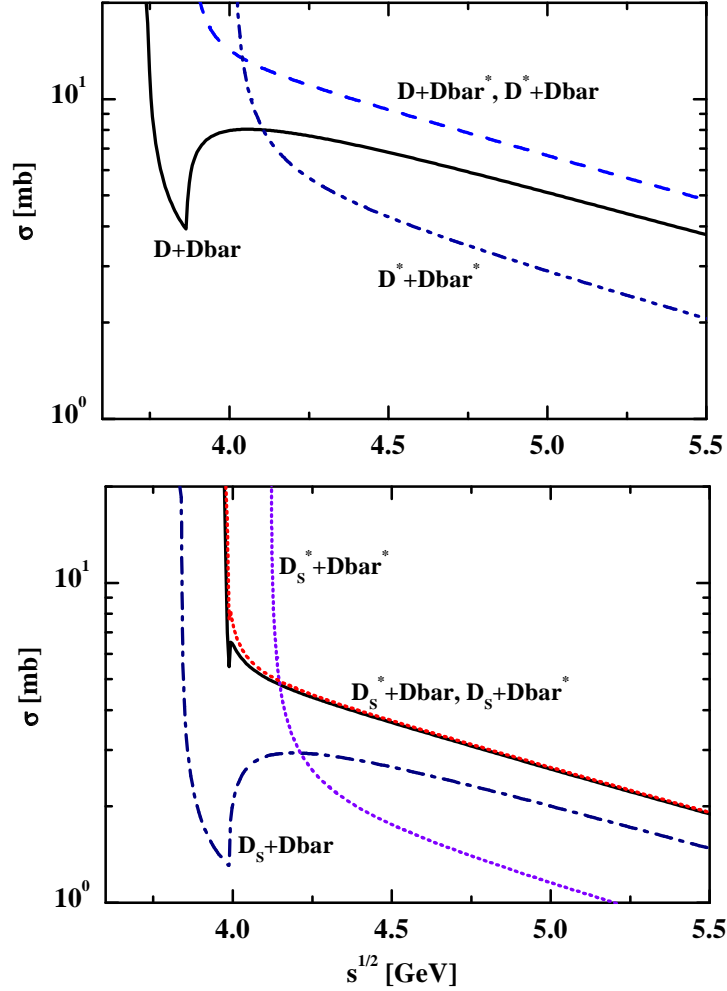


Fig. 20. The cross sections for the channels  $D+\bar{D}, D+\bar{D}^*, D^*+\bar{D}, D^*+\bar{D}^* \rightarrow J/\Psi + \text{meson}$  (upper part) and the channels involving  $s$  or  $\bar{s}$  quarks  $D_s+\bar{D}, D_s+\bar{D}^*, D_s^*+\bar{D}, D_s^*+\bar{D}^+ \rightarrow J/\Psi+(K, K^*)$  (lower part) as a function of the invariant energy  $\sqrt{s}$  according to the model described in the text (Eq. (14)).

with charm quark and charge conservation. Note that for the comover absorption scenario essentially the regime  $3.8 \text{ GeV} \leq \sqrt{s} \leq 4.8 \text{ GeV}$  is of relevance (cf. Fig. 19) where the dissociation cross sections are on the level of a few mb. We note that the explicit channel  $J/\Psi + \pi \rightarrow D + \bar{D}$ , which has often been calculated in the literature<sup>140,141,144,145</sup>, is below 0.7 mb in our model. A somewhat more essential result is that the  $J/\Psi$  dissociation cross section with  $\rho$ -mesons is in the order of 5-7 mb as in the calculations of Haglin<sup>146</sup> used before in Ref. 33, since this channel was found to dominate the  $J/\Psi$  dissociation at SPS energies<sup>36</sup>. Indeed, the calculations

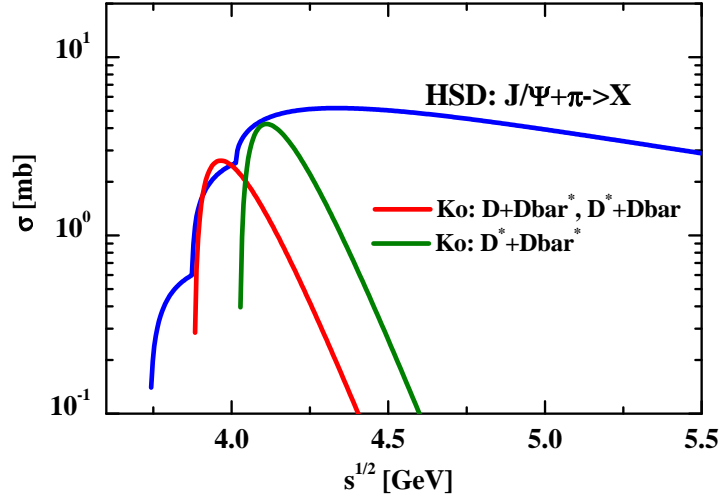


Fig. 21. The  $J/\Psi$  dissociation cross section specified in (10)-(12), upper blue line, compared to the exclusive cross sections with  $D\bar{D}^*$ ,  $D^*\bar{D}^*$  final states from Ref. <sup>132</sup> (red and green lines).

show that in the realistic fireball evolution the  $J/\Psi$ 's are dominantly absorbed in collisions with  $\rho$ -mesons as seen in Fig. 19, where the distribution in the invariant collision energy  $\sqrt{s}$  is plotted for  $J/\Psi$  absorption on  $\pi$ ,  $\eta$ ,  $\rho$  and  $\omega$  mesons in central ( $b = 2$  fm) Pb+Pb collisions at 160 A-GeV. It should be pointed out that the 'comover' dissociation channels for charmonia are described in HSD with the proper individual thresholds for each channel in contrast to the more schematic 'comover' absorption model in Refs. <sup>112,133</sup>.

The advantage of the model (10) is that detailed balance for the binary reactions can be employed strictly for each individual channel, *i.e.*

$$\sigma_{3+4 \rightarrow 1+2}(s) = \sigma_{1+2 \rightarrow 3+4}(s) \frac{(2S_1 + 1)(2S_2 + 1)}{(2S_3 + 1)(2S_4 + 1)} \frac{p_i^2}{p_f^2}, \quad (14)$$

and the role of the backward reactions ( $(c\bar{c})_i$ +meson formation by  $D + \bar{D}$  flavor exchange) can be explored without introducing any additional parameter once  $|M_0|^2$  is fixed. In Eq. (14) the quantities  $S_j$  denote the spins of the particles, while  $p_i^2$  and  $p_f^2$  denote the cms momentum squared in the initial and final channels, respectively. The uncertainty in the cross sections (14) is of the same order of magnitude as that in Lagrangian approaches using *e.g.*  $SU(4)_{\text{flavor}}$  symmetry <sup>144,145</sup>, since the form factors at the vertices are essentially unknown <sup>142</sup>. The cross sections for these backward channels – summed up again over all possible binary final states – are displayed in Fig. 20 separately for the 'non-strangeness' (upper part) and 'strangeness' channels (lower part).

The regeneration of charmonia by recombination of  $D$  ( $D^*$ ) mesons in the hadronic phase was first studied by C.M. Ko and collaborators in Ref. <sup>132</sup>. The con-

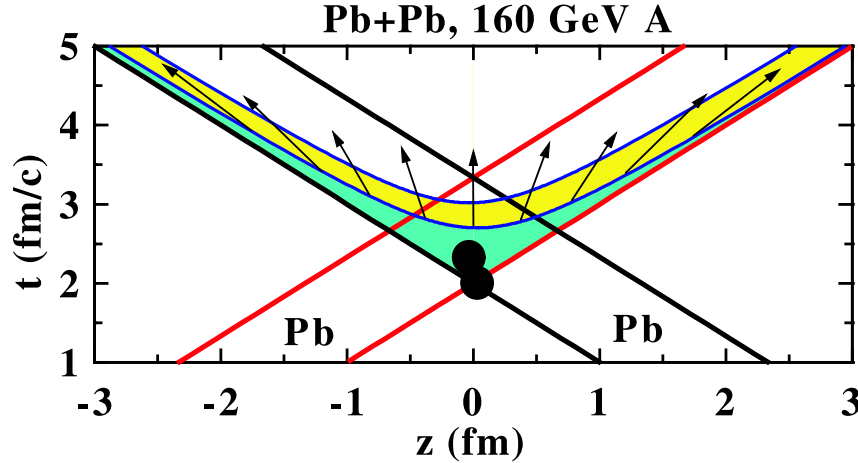


Fig. 22. Schematic representation of a Pb + Pb collision at 160 A·GeV in space-time. The full dots represent early hard collision events (for Drell-Yan and  $c\bar{c}$ -pairs) while mesons ( $\pi, \eta, \rho, \omega$ , etc. – arrows) only appear after a respective formation time  $t_F$ . The overlap area (inner rectangle) specifies the space-time region of hard production events. The figure is taken from Ref. <sup>88</sup>.

clusion at that time was that this process was unlikely at RHIC energies <sup>132,139,147</sup>. On the other hand, it was shown within HSD <sup>47</sup> that the contribution of the  $D + \bar{D}$  annihilation to the produced  $J/\Psi$  at RHIC is considerable. Moreover, the equilibrium in the reaction  $J/\Psi + m \leftrightarrow D\bar{D}$  is reached (i.e. the charmonium recreation is comparable with the dissociation by ‘comoving’ mesons). The reason for such differences is that the pioneering study <sup>132</sup> within the hadron gas model was confined to  $J/\Psi$  reactions with pions only and into two particular  $D\bar{D}$  channels ( $D + \bar{D}^*$  and  $D^* + \bar{D}$ ). As one can see in Fig. 21, the cross sections used in Refs. <sup>132,147</sup> – as obtained in the quark exchange model <sup>140</sup> – in the two dissociation channels  $J/\Psi + \pi \rightarrow D + \bar{D}^*$  and  $J/\Psi + \pi \rightarrow D^* + \bar{D}$  agree with the parametrization (10). However, in HSD the interactions with all mesons into all possible combinations of  $D\bar{D}$  states have been taken into account (cf. Fig. 18). Note that the  $\rho$ -meson density at RHIC is large such that the channel with the most abundant  $\rho$ -meson resonance is *dominant*. Furthermore, in Ref. <sup>47</sup> the feed down from  $\chi_c$  and  $\Psi'$  decays has been considered. The results of Ref. <sup>47</sup> are in accordance with independent studies in Refs. <sup>148,149,150,151</sup> that stress the importance for  $D\bar{D}$  annihilation in the late (purely hadronic) stages of the collisions.

Note that in the default HSD approach (i.e. in the hadronic comover dissociation and recombination scenario) only formed comoving mesons participate in dissociation or  $D\bar{D}$  recombination reactions (cf. Subsection 6.3). Being hard probes,  $c\bar{c}$  pairs are created in the early stage of the collision, while the comoving mesons are formed at a later stage. This situation is illustrated in Fig. 22 for a central Pb+Pb collision at 160 A·GeV for freely streaming baryons (thick black and red

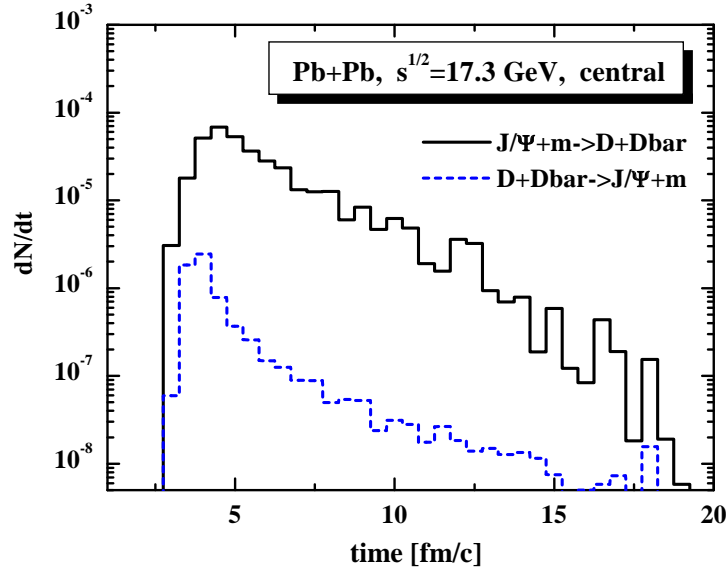


Fig. 23. The calculated rate of  $J/\Psi$  dissociation reactions with mesons (solid histogram) for central  $Pb + Pb$  collisions at  $\sqrt{s} = 17.3$  GeV in comparison to the rate of backward reactions of open charm pairs to  $J/\Psi +$  meson (dashed histogram). The figure is taken from Ref. 47.

lines). The initial string formation space-time points are indicated by the full dots; the mesons (indicated by arrows) hadronize after a time delay  $t_F \approx 0.8$  fm/c as shown by the first hyperbola. A  $c\bar{c}$ -pair produced in the initial hard nucleon-nucleon collision cannot be absorbed by mesons in the (green) shaded areas in space and time; however, a sizeable fraction of  $c\bar{c}$  pairs (which should be produced within the inner rectangles) can also be produced in a dense mesonic environment. The upper hyperbolas in Fig. 22 represent the boundaries for the appearance of mesons from the second interaction points (full dots) which appear somewhat later in time; they stand for a representative further nucleon-nucleon collision during the reaction.

Thus, the interaction with comoving mesons can occur only in the late stages of the reaction, i. e. after  $t_F$  in their rest frame. This is taken into account in HSD by treating ‘formed’ particles and ‘pre-hadrons’ differently:

- A ‘formed’ meson (baryon) is a quark-antiquark (quark-diquark) correlation – produced at time  $t_0$  – with hadronic quantum numbers that satisfies the two constrains:

$$\text{the time since production } t - t_0 > t_F = \gamma\tau_F$$

and

$$\text{the local energy density } \varepsilon < 1 \text{ GeV/fm}^3,$$

where  $\tau_F \approx 0.8$  fm/c is the formation time, and  $\gamma$  the Lorentz  $\gamma$ -factor w.r.t. to the calculational frame.

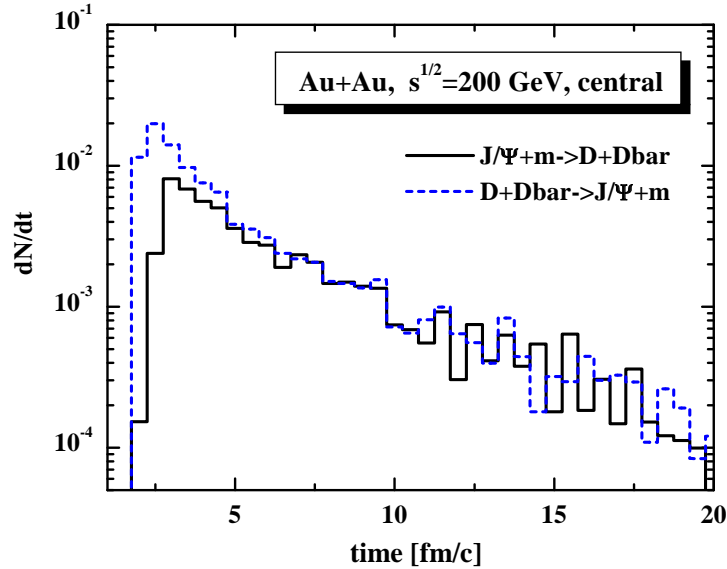


Fig. 24. The calculated rate of  $J/\Psi$  dissociation reactions with mesons (solid histogram) for central  $Au + Au$  collisions at  $\sqrt{s} = 200$  GeV in comparison to the rate of backward reactions of open charm pairs to  $J/\Psi +$  meson (dashed histogram). The figure is taken from Ref. 47.

- A ‘pre-hadron’ is a correlation with hadronic quantum numbers for

$$t - t_0 < t_F = \gamma\tau_F$$

or

$$\varepsilon > 1\text{GeV}/\text{fm}^3.$$

- leading quarks (diquarks) of the strings do not carry hadronic quantum numbers; they interact with reduced cross sections, which are set to 1/3 (2/3) of the hadronic ones in line with constituent quark number scaling.

The result for the total  $J/\Psi$  comover absorption rate (solid histogram) in central  $Pb + Pb$  collisions at 160 A GeV is shown in Fig. 23 in comparison to the  $J/\Psi$  reformation rate (dashed histogram) that includes all backward channels. Since the rates differ by about 2 orders of magnitude, the backward rate for  $J/\Psi$  formation can be neglected at SPS energies even for central  $Pb + Pb$  reactions. For central  $Au + Au$  collisions at  $\sqrt{s} = 200$  GeV, however, the multiplicity of open charm pairs should be  $\sim 16$ , i.e. by about 2 orders of magnitude larger, such that a much higher  $J/\Psi$  reformation rate ( $\sim N_{cc}^2$ ) is expected at RHIC energies (cf. Ref. 152). In Fig. 24 we display the total  $J/\Psi$  comover absorption rate (solid histogram) in comparison to the  $J/\Psi$  reformation rate (dashed histogram) as a function of time in the center-of-mass frame. Contrary to Fig. 23 now the two rates become comparable for  $t \geq 4$ -5 fm/c and suggest that in central collisions at the full RHIC energy of  $\sqrt{s} =$

200 GeV the  $J/\Psi$  comover dissociation is no longer important since the charmonia dissociated in this channel are approximately recreated in the backward channels.

## 6.2. ‘Threshold melting’ (and recombination)

The ‘threshold melting’ scenario is based on the idea of a sequential dissociation of charmonia with increasing temperature<sup>25,26,27,28</sup>, *i.e.* of charmonium melting in the QGP due to color screening as soon as the fireball temperature reaches the dissociation temperatures ( $\approx 2T_c$  for  $J/\Psi$ ,  $\approx 1.1 - 1.2T_c$  for excited states, where  $T_c$  stands for the critical temperature of the deconfinement phase transition). In the geometrical Glauber model of Blaizot et al.<sup>153</sup> as well as in the percolation model of Satz<sup>27,154</sup>, it is assumed that the QGP suppression sets in rather abruptly as soon as the energy density exceeds a threshold value  $\varepsilon_c$ , which is a free parameter. These models are motivated by the idea that the charmonium dissociation rate is drastically larger in a quark-gluon-plasma (QGP) than in a hadronic medium<sup>27</sup> such that further (hadronic) comover absorption channels might be neglected.

We modify the standard sequential dissociation model of Refs.<sup>153,27,154</sup> in two aspects: (i) the energy density is calculated locally and microscopically instead of using schematic estimates (*cf.* Section 3); (ii) the model incorporates a charmonium regeneration mechanism (by  $D\bar{D}$  annihilation processes as described in Section 6.1). The ‘threshold scenario’ for charmonium dissociation is implemented in HSD in a straight forward way: whenever the local energy density  $\varepsilon(x)$  is above a threshold value  $\varepsilon_j$ , where the index  $j$  stands for  $J/\Psi, \chi_c, \Psi'$ , the charmonium is fully dissociated to  $c + \bar{c}$ . The default threshold energy densities adopted are

$$\varepsilon_{J/\Psi} = 16 \text{ GeV/fm}^3, \quad \varepsilon_{\chi_c} = 2 \text{ GeV/fm}^3, \quad \text{and} \quad \varepsilon_{\Psi'} = 2 \text{ GeV/fm}^3. \quad (15)$$

The dissociation of charmonia has been widely studied using lattice QCD (lQCD) in Refs.<sup>155,156,157,158,159</sup> in order to determine the dissociation temperature (or energy density) via the maximum entropy method. On the other hand one may use potential models - reproducing the charmonium excitation spectrum in vacuum - to calculate Mott transition temperatures in a hot medium. Both approaches have their limitations and the quantitative agreement between the different groups is still unsatisfactory:

- (A) Potential models usually employ the static heavy quark-antiquark pair free energy  $F(T)$  - calculated on the lattice - to obtain the charmonium spectral functions. This leads to the (low) dissociation temperatures<sup>160,161</sup>

$$T_{melt}(J/\Psi) \leq 1.2T_c, \quad T_{melt}(\chi_c) \leq T_c, \quad T_{melt}(\Psi') \leq T_c.$$

An alternative way is to use the internal energy  $U = F + TS$  as a quark-antiquark potential, which due to large contributions from the entropy  $S$  provides dissociation temperatures closer to the estimate

(15) 162,163,164,165,166,167. It is presently unclear (and very much debated) how to extract a proper quark-antiquark potential from IQCD calculations.

- (B) The maximum entropy method is used to relate the Euclidean thermal correlators of charmonia - calculated on the lattice - to the corresponding spectral functions. This yields higher dissociation temperatures<sup>155</sup>

$$T_{melt}(J/\Psi) = 1.7 - 2T_c, \quad T_{melt}(\chi_c) = 1.1 - 1.2T_c$$

or<sup>156</sup>

$$T_{melt}(J/\Psi) \geq 1.5T_c, \quad T_{melt}(\chi_c) \approx 1.1T_c.$$

Since the low values for the melting temperatures from the potential models are already in conflict with the  $J/\Psi$  data at SPS, the values (15) are employed in the following (if not stated otherwise).

### 6.3. Charm interactions with pre-hadrons in the early phase

In the default HSD approach all newly produced hadrons (by string fragmentation) have a formation time of  $\tau_F \approx 0.8 \text{ fm}/c \approx 1/\Lambda_{QCD}$  in their rest frame and do not interact during the ‘partonic’ propagation. Furthermore, hadronization is inhibited, if the energy density – in the local rest frame – is above  $1 \text{ GeV}/\text{fm}^3$ , which roughly corresponds to the energy density for QGP formation in equilibrium. This default approach underestimates the elliptic flow of hadrons at RHIC energies<sup>47</sup>, the suppression of hadrons with high transverse momentum  $p_T$ <sup>168</sup> as well as the suppression of the far-side jets<sup>169</sup> in central  $Au + Au$  collisions at  $\sqrt{s} = 200 \text{ GeV}$ . This failure has been attributed to the lack of explicit partonic interactions in the early collision phase, which corresponds to the phase of high energy density with the majority of hadrons being still ‘under formation’. In order to simulate partonic interaction effects the HSD approach has been extended by explicit interactions of pre-hadrons with the (perturbative) charm degrees of freedom<sup>82</sup>.

Accordingly, an additional scenario has been implemented in the HSD simulations which is closely related to the ‘comover suppression’ scenario outlined in Section 6.1, which clearly separates ‘formed hadrons’ (existing only at energy densities below the energy density  $\varepsilon_{cut} = \varepsilon_c \approx 1 \text{ GeV}/\text{fm}^3$ ) from possible pre-hadronic states at higher energy densities, i.e. above the parton/hadron phase transition. Indeed, it is currently not clear whether  $D$ - or  $D^*$ -mesons survive at energy densities above  $\varepsilon_c$ , but hadronic correlators with the quantum numbers of the hadronic states are likely to persist above the phase transition<sup>170</sup>. Thus ‘comovers’ – with modified spectral functions – could show up also at energy densities above  $\varepsilon_c$ . We recall that in HSD a *pre-hadron* is defined as a state with the quantum numbers of a hadron, if the local energy density is above  $\approx 1 \text{ GeV}/\text{fm}^3$  or if the state is still under ‘formation’, i.e. if the time between production and hadronization is smaller than



the formation time  $\tau_F$  (in its rest frame). For a more detailed description of the pre-hadron concept we refer the reader to Section 6.1 and to Refs. <sup>171,168,172,169</sup>.

In line with the investigations in Refs. <sup>168,169</sup>, the  $J/\Psi$  production and absorption in  $Au + Au$  collisions at  $\sqrt{s} = 200$  AGeV has been studied assuming the absorption of charmonia on pre-hadrons as well as their regeneration by pre-hadrons <sup>82</sup>. This adds additional interactions of the particles with charm quarks (antiquarks) in the very early phase of the nucleus-nucleus collisions as compared to the default HSD approach. Since these pre-hadronic (color-dipole) states represent some new degrees-of-freedom, the interactions of charmed states with these objects have to be specified separately.

For notation, we define a pre-hadronic state consisting of a quark-antiquark pair as *pre-meson*  $\tilde{m}$  and a state consisting of a diquark-quark pair as *pre-baryon*  $\tilde{B}$ . The dissociation cross section of a  $c\bar{c}$  color dipole state with a pre-baryon is taken to be of the same order as with a formed baryon,

$$\sigma_{c\bar{c}\tilde{B}}^{diss} = 5.8 \text{ mb}, \quad (16)$$

whereas the cross section with a pre-meson follows from the additive quark model as <sup>171,172</sup>

$$\sigma_{c\bar{c}\tilde{m}}^{diss} = \frac{2}{3}\sigma_{c\bar{c}\tilde{B}}^{diss}. \quad (17)$$

Elastic cross sections are taken as

$$\sigma_{c\bar{c}\tilde{B}}^{el} = 1.9 \text{ mb}, \quad \sigma_{c\bar{c}\tilde{m}}^{el} = \frac{2}{3}\sigma_{c\bar{c}\tilde{B}}^{el}. \quad (18)$$

Furthermore, elastic interactions of a charm quark (antiquark) are modeled by the scattering of an unformed  $D$  or  $D^*$  meson on pre-hadrons with only light quarks as

$$\sigma_{D\tilde{B}}^{el} = 3.9 \text{ mb}, \quad \sigma_{D\tilde{m}}^{el} = \frac{2}{3}\sigma_{D\tilde{B}}^{el}. \quad (19)$$

In this way one can incorporate in HSD some dynamics of quark-antiquark pairs with a medium that has not yet formed the ordinary hadrons. However, it has to be stressed that further explicit partonic degrees of freedom, i.e. gluons and their mutual interactions as well as gluon interactions with quarks and antiquarks, have not been taken into account explicitly so far.

#### 6.4. Thermal and statistical models

The statistical and thermal models are based on the assumption of statistical equilibrium, where the physical system can be characterized by a few Lagrange parameters that specify the average energy as well as the average particle number, flavor content, *etc.* Since the fireball created in relativistic nucleus-nucleus collisions is rapidly expanding, equilibrium rate equations for charmonium dissociation and regeneration are folded over a thermally evolving background in time <sup>173</sup>. In a

simplified form, the rate equation for the time evolution of a charmonium state  $\psi$ ,  $N_\psi(\tau)$  can be written as

$$\frac{dN_\psi}{d\tau} = -\Gamma_\psi [N_\psi - N_\psi^{eq}] . \quad (20)$$

The first key quantity in (20) is the inelastic charmonium reaction rate,  $\Gamma_\psi$ , which, by detailed balance, governs both gain and loss terms<sup>173</sup>. This is in quite analogy to the covariant transport models. In the QGP, the leading-order (LO) process is the well-known gluo-dissociation,  $g + \psi \rightarrow c + \bar{c}$ . However, as has been first emphasized in Ref.<sup>152</sup>, the gluo-dissociation process becomes inefficient for small  $J/\psi$  binding energies as expected due to color screening in the QGP (and even without screening for  $\psi'$  and  $\chi_c$  states). Therefore, the quasi-free dissociation process,  $p + \psi \rightarrow c + \bar{c} + p$  ( $p = q, \bar{q}, g$ ) has been introduced<sup>152</sup>, which naively is of next-to-leading order in  $\alpha_s$ , but provides a much larger phase space, and, consequently, the dominant dissociation rate for small charmonium binding (for gluo-dissociation, the phase space vanishes in the limit of vanishing binding energy). The other key quantity is the charmonium equilibrium limit,  $N_\psi^{eq}(\tau)$ , which depends on the charm content and temperature of the system. The typical procedure is to assume charm production to be a hard process and thus to be restricted to primordial  $N$ - $N$  collisions. The statistical model is then used to distribute the fixed number of  $c\bar{c}$  pairs over the available charmed states in the system. This introduces both temperature and volume dependencies into  $N_\psi^{eq}(T(\tau))$ , as well as a sensitivity to medium modifications of the charm states (e.g., reduced  $D$ -meson masses lead to a reduction in the charmonium equilibrium numbers)<sup>122,174</sup>. Alternative absorption mechanisms might also play a role, such as gluon scattering on color dipole states as suggested in Refs.<sup>125,152,175,176</sup> or charmonium dissociation in the strong color fields of overlapping strings<sup>87</sup>.

The statistical hadronization model<sup>120</sup> (originally proposed in Ref.<sup>137</sup>) follows a very different idea. The  $c\bar{c}$  are produced by initially hard  $NN$  scattering, but charmonium bound states are generated in a statistical fashion at the phase boundary from the QGP to the hadronic phase<sup>177</sup>. This is fundamentally different from a regeneration of charmonia in the hadronic phase by  $D + \bar{D}$  collisions and implies that all charmonia are emerging from a QGP phase. Since this assumption is questionable for peripheral nucleus-nucleus collisions, the authors have later on introduced ‘corona effects’ that mimic non-QGP charmonium formation. We will come back to actual results and comparisons in Section 8.

Slightly later Thews et al. developed a coalescence model for charmonium production in the QGP<sup>136</sup> which states that the abundance of charmonia increases roughly with the  $c\bar{c}$  density squared and accordingly becomes increasingly important at higher bombarding energy (especially at LHC energies). While actual data at RHIC do not strongly support this scenario, it will be of substantial interest if the future data at LHC will provide evidence for charmonium enhancement instead of suppression<sup>120,173</sup>.

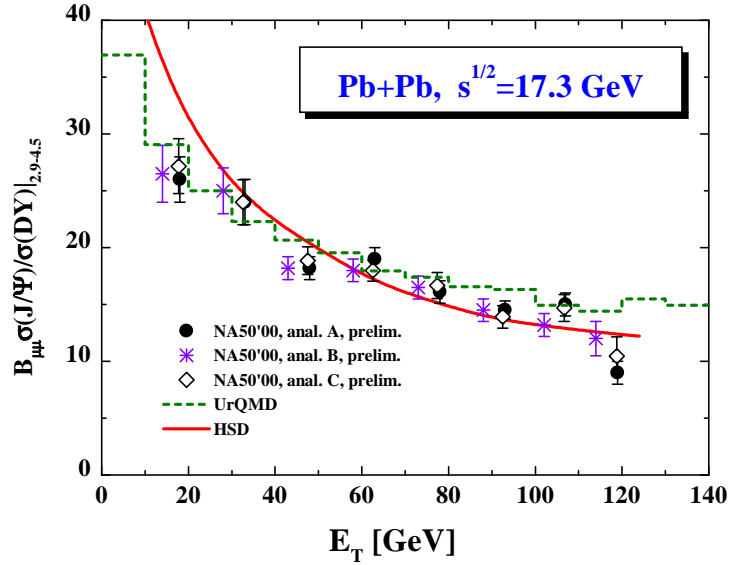


Fig. 25. The  $J/\Psi$  suppression as a function of the transverse energy  $E_T$  in Pb+Pb collisions at 160 A·GeV. The solid line shows the HSD result within the comover absorption scenario<sup>47,48</sup>. The different symbols stand for the NA50 data<sup>128</sup> from the year 2000 (analysis A,B,C) while the dashed histogram is the UrQMD result<sup>127</sup>. The figure is taken from Ref.<sup>126</sup>.

## 7. Anomalous suppression of $J/\Psi$ : Comparison to data

### 7.1. $J/\Psi$ and $\Psi'$ suppression at SPS energies

As pointed out before, ‘cold nuclear matter’ absorption effects alone cannot reproduce the strong suppression of  $J/\Psi$  observed by the NA50 collaboration in central  $Pb+Pb$  collisions (*cf.* Fig 11). The extra suppression of charmonia in the high density phase of nucleus-nucleus collisions then may be attributed to the different ‘hot matter’ scenarios outlined in Section 6.

As a reminder, we recall the early  $J/\Psi$  suppression results for Pb+Pb at 160 A·GeV (in the comover suppression scenario) both from the UrQMD and HSD transport calculations, which are in line with the data of the NA50 Collaboration as demonstrated in Fig. 25, where the calculated  $J/\Psi$  suppression is shown as a function of the transverse energy  $E_T$ . The solid line stands for the HSD result (within the comover absorption scenario)<sup>47,48</sup>, while the various data points reflect the NA50 data from the year 2000 (analysis A,B,C) that agree reasonably well with the HSD and UrQMD calculations<sup>127</sup> (dashed histogram in Fig. 25).

The anomalous suppression observed in S+U and Pb+Pb collisions by the NA38<sup>3</sup> and NA50 Collaborations<sup>4,128</sup> has been experimentally confirmed by NA60<sup>5</sup> in In+In collisions at 158 A·GeV. A couple of models have predicted  $J/\Psi$  suppression in In+In collisions as a function of centrality at 158 A·GeV based on the parameters fixed for Pb+Pb reactions at the same bombarding energy. How-

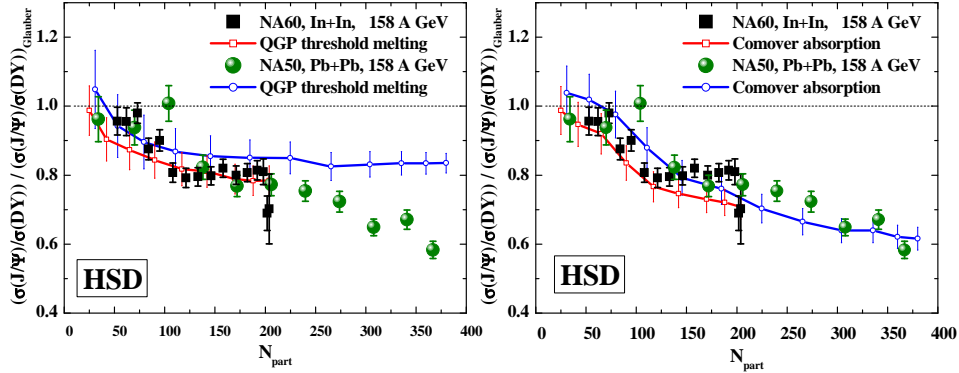


Fig. 26. The ratio  $B_{\mu\mu}\sigma(J/\Psi)/\sigma(DY)$  as a function of the number of participants  $N_{part}$  in In+In (red line with open squares) and Pb+Pb reactions (blue line with open circles) at 158 A-GeV relative to the normal nuclear absorption given by the straight black line. The full dots and squares denote the respective data from the NA50 and NA60 Collaborations. The model calculations reflect the comover absorption model (right part) and the ‘QGP threshold scenario’ (left part) with  $\varepsilon_{J/\Psi} = 16 \text{ GeV}/\text{fm}^3$ ,  $\varepsilon_{\chi_c} = 2 \text{ GeV}/\text{fm}^3$ ,  $\varepsilon_{\Psi'} = 2 \text{ GeV}/\text{fm}^3$  while discarding comover absorption. The figure is taken from Ref. 44.

ever, the predictions within the ‘Glauber based’ comover model and the ‘threshold melting scenario’ from Refs. 178,179,154 have failed to describe the In+In data with sufficient accuracy (cf. Section 7.2).

The charmonium production and suppression in In+In and Pb+Pb reactions at SPS energies has been reinvestigated in the HSD transport approach in 2006 within the ‘hadronic comover model’ as well as the ‘QGP threshold scenario’ 44. As found in Ref. 44, the comover absorption model – with a single parameter  $|M_0|^2$  for the matrix element squared for charmonium-meson dissociation – performs best with respect to all data sets for  $J/\Psi$  suppression as well as for the  $\Psi'$  to  $J/\Psi$  ratio for Pb+Pb (cf. Figs. 26,27). We recall that the  $\Psi'$  suppression is presented experimentally by the ratio

$$\frac{B_{\mu\mu}(\Psi' \rightarrow \mu\mu)\sigma(\Psi')/\sigma(DY)}{B_{\mu\mu}(J/\Psi \rightarrow \mu\mu)\sigma(J/\Psi)/\sigma(DY)}. \quad (21)$$

In the HSD calculations this ratio is taken as 0.0165 for nucleon-nucleon collisions, which is again based on the average over  $pp, pd, pA$  reactions 85. The centrality dependence of the ratio is then a prediction of the model for different systems and bombarding energies.

The ‘QGP threshold scenario’ roughly reproduces the  $J/\Psi$  suppression for both systems at 158 A-GeV (Fig. 26, l.h.s.) apart from the very central Pb+Pb collisions. The comover absorption model follows slightly better the fall of the  $J/\Psi$  survival probability with increasing centrality (Fig. 26, r.h.s.), whereas the ‘threshold scenario’ leads to an approximate plateau in both reactions for high centrality.

On the other hand, the ‘threshold melting scenario’ clearly fails for the  $\Psi'$  to

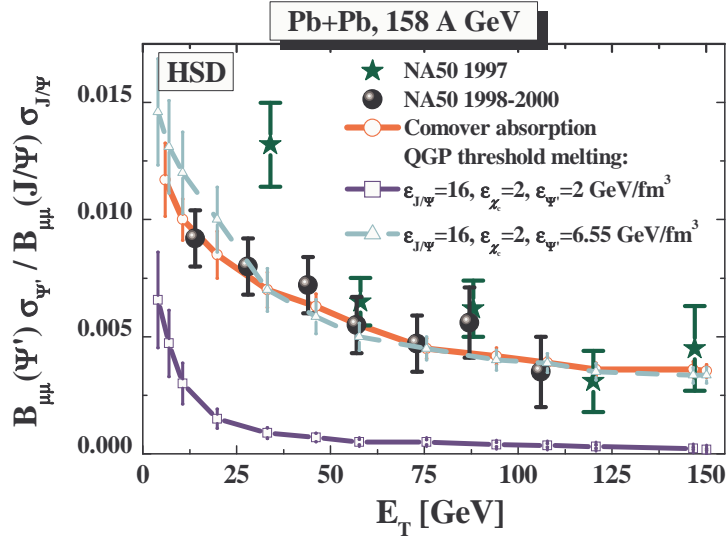


Fig. 27. The  $\Psi'$  to  $J/\Psi$  ratio as a function of the transverse energy  $E_T$  for Pb+Pb at 160 A-GeV. The full dots and stars denote the respective data from the NA50 Collaboration<sup>100</sup>. The HSD result<sup>44</sup> for the comover absorption model is shown as the red line, whereas the blue line indicates the ‘QGP threshold scenario’ with  $\epsilon_{J/\Psi} = 16 \text{ GeV/fm}^3$ ,  $\epsilon_{\chi_c} = 2 \text{ GeV/fm}^3 = \epsilon_{\Psi'}$ , and the light blue line with  $\epsilon_{J/\Psi} = 16 \text{ GeV/fm}^3$ ,  $\epsilon_{\chi_c} = 2 \text{ GeV/fm}^3$  and  $\epsilon_{\Psi'} = 6.55 \text{ GeV/fm}^3$  (discarding comover absorption). The figure is taken from Ref. 44.

$J/\Psi$  ratio, since too many  $\Psi'$  already melt away for a critical energy density of  $2 \text{ GeV/fm}^3$  at 158 A-GeV (cf. Fig. 27). Only when assuming the  $\Psi'$  to dissolve above  $\sim 6.5 \text{ GeV/fm}^3$  a reasonable description of all data is achieved in the ‘QGP threshold scenario’; this threshold, however, is not in accordance with lattice QCD calculations such that the ‘threshold scenario’ meets severe problems.

Indeed, the extra suppression of charmonia by comovers is seen in Fig. 28 (solid red lines) to match the  $J/\Psi$  suppression in In+In and Pb+Pb as well as the  $\Psi'$  to  $J/\Psi$  ratio (for Pb+Pb) rather well. The more recent data (1998-2000) for the  $\Psi'$  to  $J/\Psi$  ratio agree with the HSD prediction<sup>48</sup> within error bars. This had been a problem in the past when comparing to the 1997 data (dark green stars). One may conclude that the comover absorption model so far cannot be ruled out on the basis of the available data sets from the SPS within error bars. The  $\Psi'$  to  $J/\Psi$  ratio for In+In versus centrality is not yet available from the experimental side but the theoretical predictions (provided in Fig. 28) might be verified/falsified in future.

Some comments on the comover absorption model appear in place: As shown in Fig. 7.2 of Ref. 36, the comover densities in central Pb+Pb collisions at 158 A-GeV become quite large and almost reach  $2 \text{ fm}^{-3}$  in the maximum, which appears high for ‘free’ mesons with an eigenvolume of about  $1 \text{ fm}^3$ . However, as mentioned before, the quasi-particle mesons considered here dynamically should not be identified with ‘free’ meson states that show a long polarization tail in the vacuum. As known from

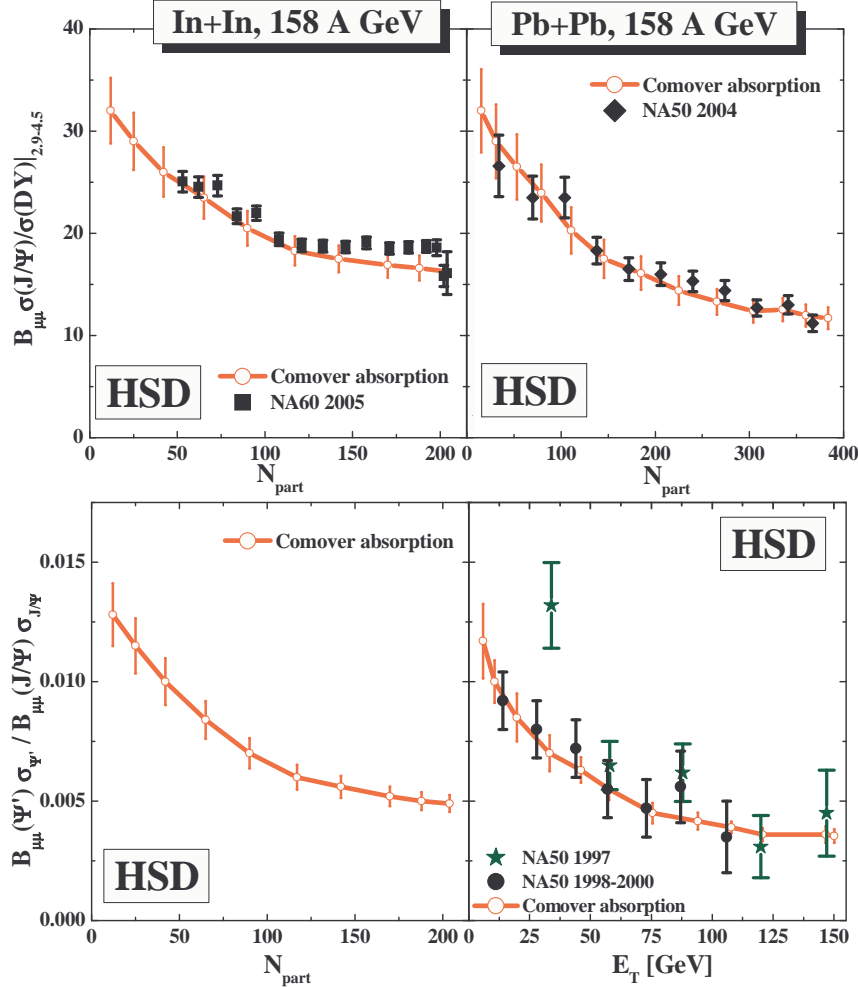


Fig. 28. The ratio  $B_{\mu\mu}\sigma(J/\Psi)/\sigma(DY)$  as a function of the number of participants in In+In (l.h.s.) and Pb+Pb reactions (r.h.s.) at 158 A-GeV. The full symbols denote the data from the NA50 and NA60 Collaborations (from Refs. 4,5,100). The solid (red) lines show the HSD results for the comover absorption model with a matrix element squared  $|M_0|^2 = 0.18 \text{ fm}^2/\text{GeV}^2$ . The lower parts of the figure show the HSD results in the same limit for the  $\Psi'$  to  $J/\Psi$  ratio as a function of  $N_{part}$  (for In+In) or the transverse energy  $E_T$  (for Pb+Pb). The vertical lines on the graphs reflect the theoretical uncertainty due to limited statistics of the calculations. The figure is taken from Ref. 44.

lattice QCD, the correlators for pions and  $\rho$ -mesons survive well above the critical temperature  $T_c$ , such that ‘dressed’ mesons, i.e spectral densities with the quantum numbers of the pseudo-scalar and vector (isovector) modes, also show up at high energy density (similar to the  $J/\Psi$  discussed above <sup>129,130,180</sup>). Such ‘dressed’ mesons are expected to have a more compact size in space.

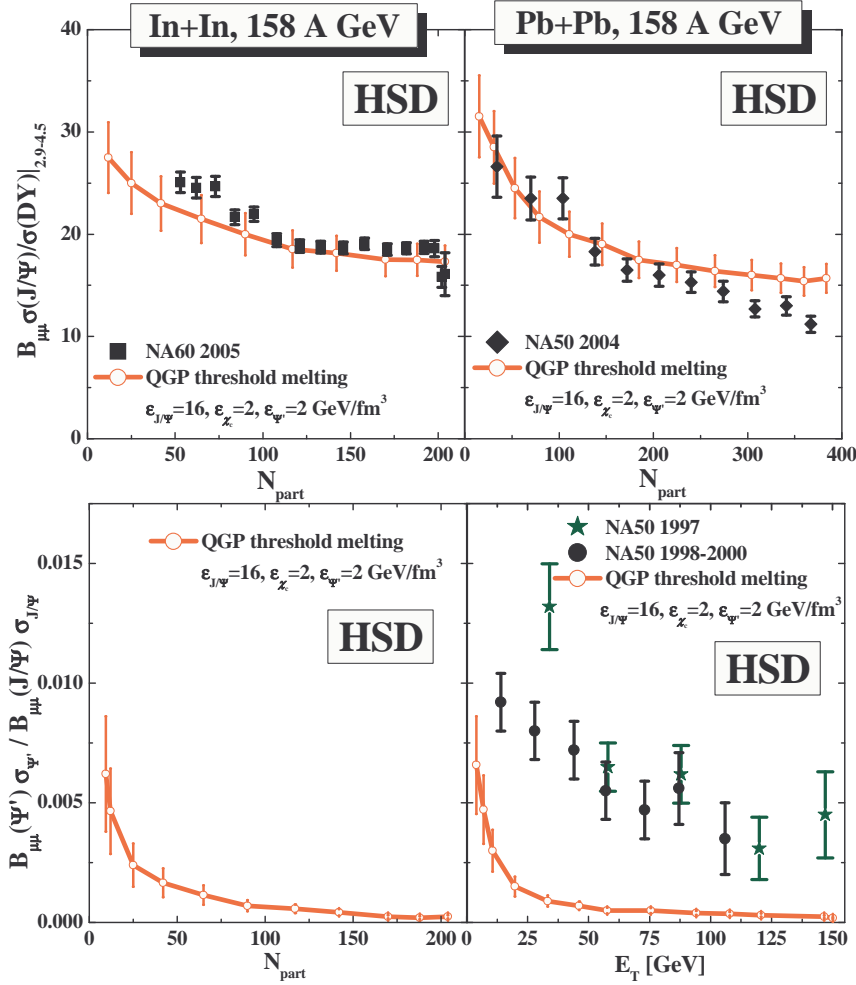


Fig. 29. Same as Fig. 28 but for the ‘QGP threshold scenario’ with  $\varepsilon_{J/\Psi} = 16 \text{ GeV/fm}^3$ ,  $\varepsilon_{\chi_c} = 2 \text{ GeV/fm}^3 = \varepsilon_{\Psi'}$  while discarding comover absorption, *i.e.* for  $|M_0|^2 = 0$ . The figure is taken from Ref. 44.

The results for the ‘threshold scenario’ for  $J/\Psi$  as well as  $\Psi'$  are displayed in Fig. 29 in comparison to the same data for the thresholds  $\varepsilon_{J/\Psi} = 16 \text{ GeV/fm}^3$ ,  $\varepsilon_{\chi_c} = 2 \text{ GeV/fm}^3 = \varepsilon_{\Psi'}$  while discarding any dissociation with comovers, *i.e.*  $|M_0|^2 = 0$ . In this scenario, the  $J/\Psi$  suppression is well described for In+In, but the suppression is slightly too weak for very central Pb+Pb reactions. This result emerges, since practically all  $\chi_c$  and  $\Psi'$  dissolve for  $N_{part} > 100$  in both systems whereas the  $J/\Psi$  itself survives at the energy densities reached in the collision. Since the nucleon dissociation is a flat function of  $N_{part}$  for central reactions, the total absorption strength is flat, too. The deviations seen in Fig. 29 might indicate a partial

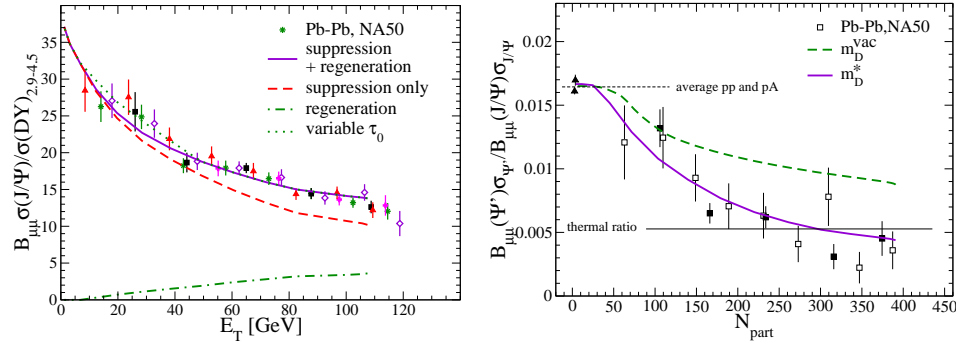


Fig. 30. NA50 data <sup>128,182</sup> on  $J/\psi$  (left panel) and  $\psi'$  (right panel) production in Pb(158 AGeV)-Pb collisions at the SPS, compared to solutions of a kinetic rate equation in a thermal fireball background <sup>122</sup> starting from initial yields subject to primordial nuclear absorption. The figure is taken from Ref. <sup>30</sup>.

melting of the  $J/\Psi$  for  $N_{part} > 250$ , which is not in line with current lattice QCD calculations claiming at least  $\varepsilon_{J/\Psi} > 5 \text{ GeV}/\text{fm}^3$ . In fact, a lower threshold of  $5 \text{ GeV}/\text{fm}^3$  (instead of  $16 \text{ GeV}/\text{fm}^3$ ) for the  $J/\Psi$  has practically no effect on the results shown in Fig. 29. Furthermore, a threshold energy density of  $2 \text{ GeV}/\text{fm}^3$  for the  $\Psi'$  leads to a dramatic reduction of the  $\Psi'$  to  $J/\Psi$  ratio, which is in severe conflict with the data (lower part of Fig. 29). Also note that due to energy density fluctuations in reactions with fixed  $N_{part}$  (or  $E_T$ ) there is no step in the suppression of  $J/\Psi$  versus centrality as pointed out before by Gorenstein et al. in Ref. <sup>181</sup>.

## 7.2. Thermal and statistical models at SPS

It is of interest to compare the results of dynamical (transport) models with the statistical and thermal fireball models, which assume statistical equilibrium during the nucleus-nucleus collision.

In Ref. <sup>122</sup> the rate equation (20) has been solved for  $Pb(158 \text{ AGeV})$ - $Pb$  collisions using a fireball evolution fitted to transport calculations. The authors also include primordial nuclear absorption and suppression in the hadronic phase. The resulting centrality dependence for  $J/\psi$  production (including feed-down from  $\chi_c$  and  $\Psi'$ ) is shown in the left panel of Fig. 30. The only free parameter in this approach is the strong coupling constant entering into the quasi-free dissociation cross section in the QGP which has been fixed to  $\alpha_s \simeq 0.25$ . The NA50 data <sup>128</sup> are fairly well reproduced, with a small contribution from regeneration (incorporated also by detailed balance). The main effect for the direct  $J/\psi$ 's is their suppression which is largely restricted to the QGP (after nuclear absorption as inferred from  $p$ -A data). On the other hand,  $\Psi'$  suppression is found to be substantially affected by the hadronic phase, and the NA50 data <sup>182</sup> can only be reproduced in this approach, if in-medium (dropping)  $D$ -meson masses are implemented, which accelerate the direct  $\Psi' \rightarrow D\bar{D}$  decays, cf. right panel of Fig. 30.



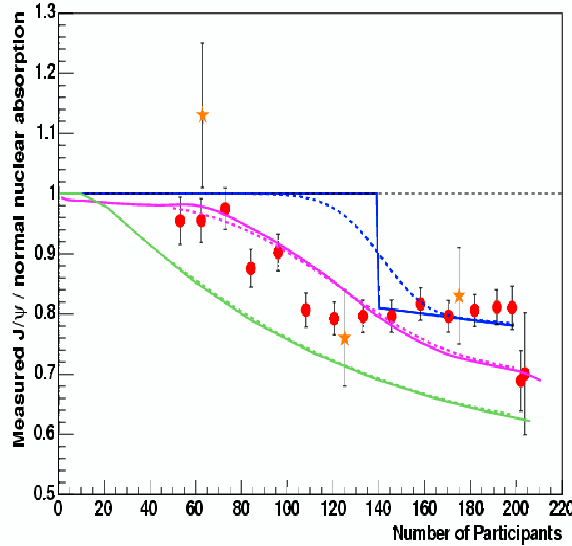


Fig. 31. NA60 data for  $J/\psi$  production in In(158 AGeV)-In<sup>185</sup> compared to theoretical model predictions that are in approximate agreement with the NA50  $Pb - Pb$  data: percolation model (upper (dashed) blue line)<sup>154</sup>, kinetic rate equation (middle magenta line)<sup>184</sup> and hadronic comovers (lower green line)<sup>109</sup>. Data and theory curves are normalized to an “expected yield” which includes the effects of primordial nuclear absorption as extracted from  $p$ -A data. The figure is taken from Ref. 183.

A widely debated issue, furthermore, is whether the NA50 data support the notion of a more or less sharp “onset behavior” of  $J/\psi$  suppression, possibly related to the formation of a deconfined medium. The NA60 collaboration has scrutinized this issue by measuring the  $J/\psi$  suppression pattern in a medium-size system, i.e., In-(158 AGeV)-In. The data<sup>183</sup>, normalized to the  $J/\psi$  yield expected after primordial nuclear absorption, are compared to theoretical predictions in Fig. 31: dissociation of  $c\bar{c}$  states in QGP by Satz, Digal, Fortunato<sup>154</sup> (blue lines); regeneration of charmonium in the QGP by Rapp, Grandchamp, Brown<sup>184</sup> (pink lines); comover absorption by mesons in a Glauber type model (green lines) by Capella and Ferreiro<sup>109</sup>. The latter approaches have been adjusted to the NA50  $Pb+Pb$  data, but it turns out that none of them fully describes the In-In measurements. The hadronic comover scenario<sup>109</sup> over-predicts the suppression throughout, the schematic percolation model<sup>154</sup> misses the onset significantly, while the kinetic rate equation approach<sup>184</sup> somewhat over-predicts the suppression for the most central collisions. Overall, the predictions of the kinetic approach (in a time-dependent thermal fireball background) do not fare too badly with the data.

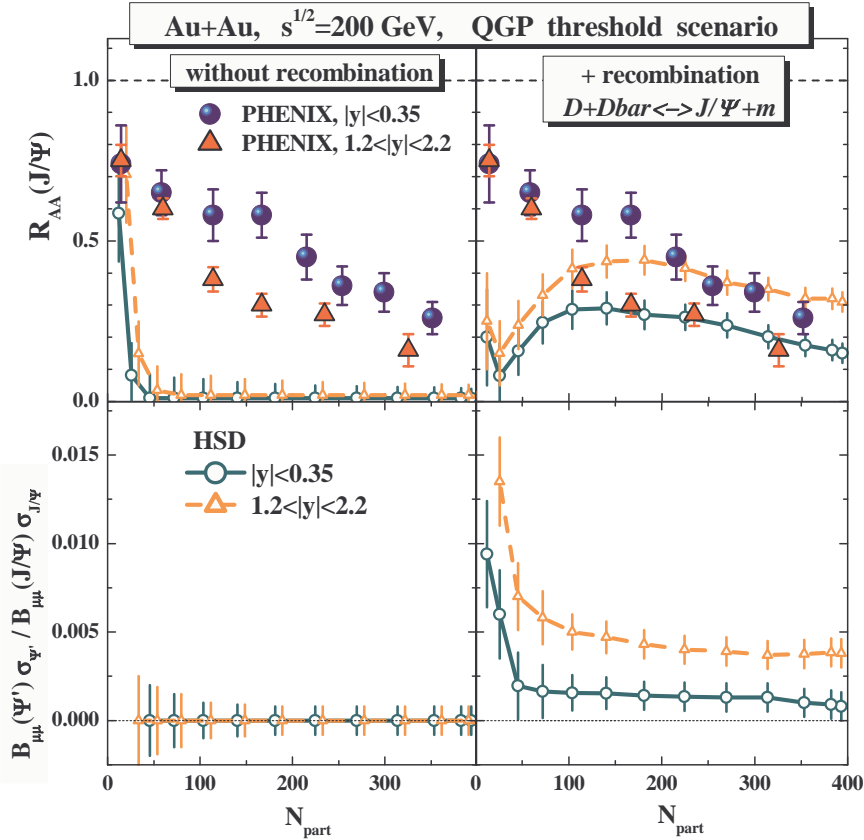


Fig. 32. The  $J/\Psi$  nuclear modification factor  $R_{AA}$  for Au+Au collisions at  $\sqrt{s} = 200$  GeV as a function of the number of participants  $N_{part}$  in comparison to the data from Ref. <sup>97</sup> for midrapidity (full circles) and forward rapidity (full triangles). HSD results for the 'QGP threshold melting' scenarios are displayed in terms of the lower (green solid) lines for midrapidity  $J/\Psi$ 's ( $|y| \leq 0.35$ ) and in terms of the upper (orange dashed) lines for forward rapidity ( $1.2 \leq y \leq 2.2$ ) without recombination (l.h.s.) and with a recombination via  $D + \bar{D}$ . The error bars on the theoretical results indicate the statistical uncertainty due to the finite number of events in the HSD calculations. Predictions for the ratio  $B_{\mu\mu}(\Psi')\sigma_{\Psi'}/B_{\mu\mu}(J/\Psi)\sigma_{J/\Psi}$  as a function of the number of participants  $N_{part}$  for Au+Au at  $\sqrt{s} = 200$  GeV are shown in the lower set of plots. The figure is taken from Ref. <sup>45</sup>.

### 7.3. $J/\Psi$ and $\Psi'$ at RHIC

Up to date a simultaneous description of the seemingly energy-independent suppression of  $J/\Psi$  together with its narrow rapidity distribution and a strong elliptic flow  $v_2$  of charmed hadrons - as found at RHIC - has presented a challenge to microscopic theories. The large discrepancies of present studies are striking in view of the success of the hadron-string transport theories in describing charmonium data at SPS energies. This has led to the conjecture that the sizeable difference between

the measured yields and transport predictions is due to a neglect of the transition from hadronic to partonic matter, i.e. the strongly-coupled Quark-Gluon-Plasma (sQGP).

In the RHIC experiments, one defines the nuclear modification factor  $R_{AA}$  as

$$R_{AA} = \frac{dN_{AA}^{J/\Psi}/dy}{N_{coll} \cdot dN_{pp}^{J/\Psi}/dy}, \quad (22)$$

where  $dN_{AA}^{J/\Psi}/dy$  denotes the final yield of  $J/\Psi$  in  $AA$  collisions,  $dN_{pp}^{J/\Psi}/dy$  is the yield in elementary  $pp$  reactions while  $N_{coll}$  is the number of initial binary collisions.

In the upper part of Fig. 32 we present a comparison of  $R_{AA}(J/\Psi)$  (from HSD) for  $Au + Au$  collisions as a function of the number of participants  $N_{part}$  to the data from Ref. 97. The results for the ‘threshold melting’ scenario (without the reformation channels  $D + \bar{D} \rightarrow (J/\Psi, \chi_c, \Psi') + \text{meson}$ ) are displayed on the l.h.s. of Fig. 32 in terms of the lower (green) solid line for mid-rapidity  $J/\Psi$ 's ( $|y| \leq 0.35$ ) and in terms of the upper (orange) dashed line at forward rapidity ( $1.2 \leq |y| \leq 2.2$ ). The experimental data from PHENIX 97 are given by the full circles at mid-rapidity and by triangles at forward rapidity. In this simple scenario practically all charmonia are dissolved for  $N_{part} > 50$  due to the high energy densities reached in the overlap zone of the collision, which is clearly not compatible with the PHENIX data and indicates that charmonium reformation channels are important.

The reformation and dissociation channels ( $D + \bar{D} \leftrightarrow (J/\Psi, \chi_c, \Psi') + \text{meson}$ ) are switched on after a formation time. The results for this model study are displayed in the upper right part of Fig. 32 and demonstrate that for  $N_{part} > 200$  an approximate equilibrium between the reformation and dissociation channels is achieved. However, here the calculations for forward rapidity match the data at mid-rapidity and vice versa showing that the rapidity dependence is fully wrong. Furthermore, the  $J/\Psi$  suppression at more peripheral reactions is severely overestimated. Thus one has to conclude that the ‘threshold melting + reformation scenario’ is incompatible with the PHENIX data and has to be ruled out at top RHIC energies.

In the lower parts of Fig. 32 the results for the ratio of the  $\Psi'$  and  $J/\Psi$  dilepton yields (given by their cross sections multiplied by the corresponding branching ratios) are shown, which so far have not been measured. Here the two recombination models give finite ratios as a function of centrality but predict a larger  $\Psi'$  to  $J/\Psi$  ratio at forward rapidity than at mid-rapidity which is a consequence of the higher comover density at mid-rapidity. Experimental data on this ratio should provide further independent information.

The suppression of charmonia by the ‘comover’ dissociation channels within the model described in Section 6.1 is presented in Fig. 33, where the charmonium reformation channels by  $D + \bar{D}$  annihilation have been incorporated. The HSD results for  $R_{AA}$  in the purely hadronic ‘comover’ scenario are displayed in the upper part of Fig. 33 in comparison to the data from Ref. 97 using the same assignment of the lines as in Fig. 32. This scenario gives a continuous decrease of  $R_{AA}(J/\Psi)$

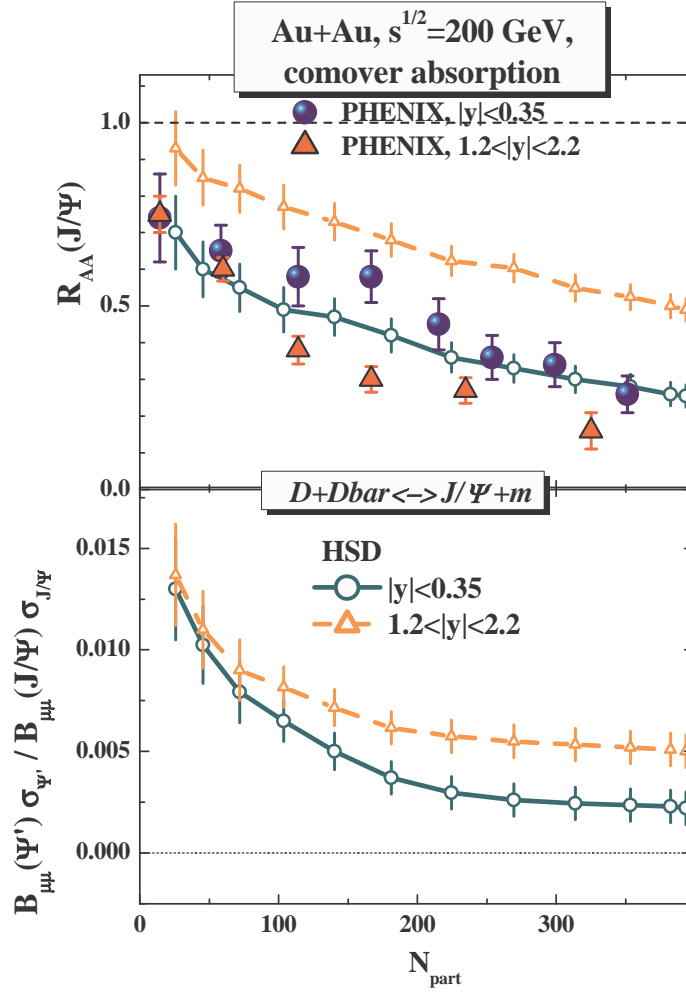


Fig. 33. Same as Fig. 32 for the ‘comover absorption scenario’ including the charmonium reformation channels. The figure is taken from Ref. <sup>45</sup>.

with centrality. However, the rapidity dependence of the comover result is opposite to the one experimentally observed, as dictated by the higher comover density at mid-rapidity.

The  $\Psi'$  to  $J/\Psi$  ratio is displayed in the lower parts of Fig. 33 and shows a decreasing ratio with centrality similar to the results at SPS energies (*cf.* Fig. 28). As pointed in Ref. <sup>44</sup>, an independent measurement of  $\Psi'$  will provide further information on the charm reaction dynamics and final charmonium formation. For instance, a leveling off of the  $\Psi'$  to  $J/\Psi$  ratio with increasing centrality would be a signal for charm chemical equilibration in the medium <sup>137,177,186</sup>. Additionally, it

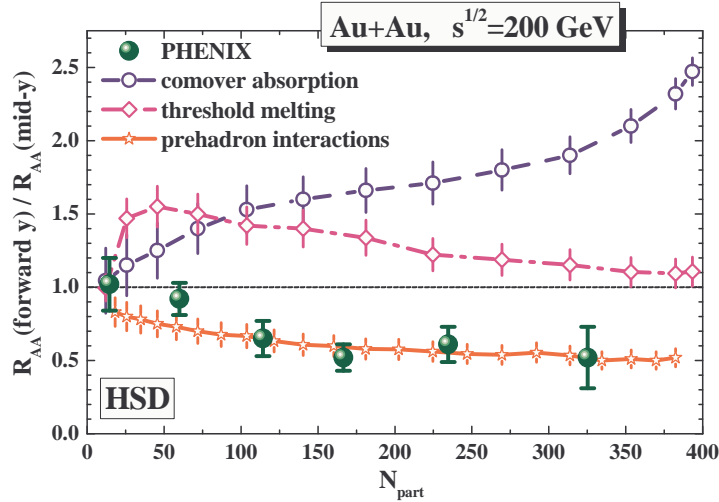


Fig. 34. The ratio of the nuclear modification factors  $R_{AA}$  at mid-rapidity ( $|y| < 0.35$ ) and at forward rapidity ( $1.2 < |y| < 2.2$ ) vs centrality in  $Au + Au$  collisions at  $\sqrt{s} = 200$  GeV. The HSD results in the purely hadronic scenario ('comover absorption') are displayed in terms of the blue dashed line (with open circles) and in case of the 'threshold melting' scenario in terms of the violet dot-dashed line (with open squares). The error bars on the theoretical results indicate the statistical uncertainty due to the finite number of Monte-Carlo events in the calculations. The lower full green dots represent the data of the PHENIX Collaboration<sup>97</sup>. Note that the data have an additional systematic uncertainty of  $\pm 14\%$ . The lower solid (red) line with stars gives the result for the 'comover absorption' scenario when including additional pre-hadronic interactions with charm (see text). The figure is taken from Ref.<sup>82</sup>.

provides a very clear distinction between the 'threshold melting' scenario and the 'comover' approach.

The non-applicability of the traditional 'comover absorption' model and 'threshold melting' scenario at the top RHIC energy is most clearly seen in the centrality dependence of the ratio of the nuclear modification factors  $R_{AA}$  at forward rapidity ( $1.2 < |y| < 2.2$ ) and at mid-rapidity ( $|y| < 0.35$ ) as shown in Fig. 34. The HSD results in the purely hadronic scenario ('comover absorption') are displayed in terms of the blue dashed line (with open circles) and in case of the 'threshold melting' scenario in terms of the dot-dashed magenta line (with open squares). The error bars on the theoretical results indicate the statistical uncertainty due to the finite number of Monte-Carlo events in the calculations. The lower full green dots in Fig. 34 represent the corresponding data of the PHENIX Collaboration<sup>97</sup> which show a fully different pattern as a function of centrality (here given in terms of the number of participants  $N_{part}$ ). The failure of these 'standard' suppression models at RHIC has led to the conclusion in Ref.<sup>45</sup> that the hadronic 'comover absorption and recombination' model is falsified by the PHENIX data and that strong interactions in the pre-hadronic (or partonic) phase is necessary in order to explain

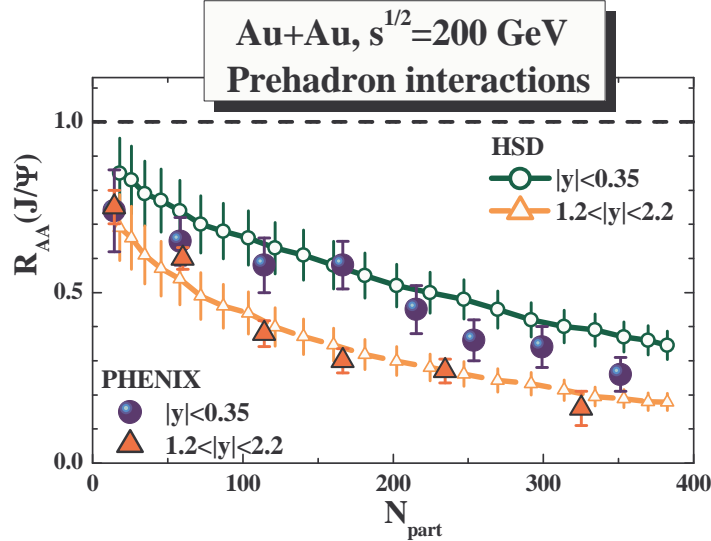


Fig. 35. The  $J/\Psi$  nuclear modification factor  $R_{AA}$  (22) for Au+Au collisions at  $\sqrt{s} = 200$  AGeV as a function of the number of participants  $N_{part}$  in comparison to the data from <sup>97</sup> for mid-rapidity (full circles) and forward rapidity (full triangles). The HSD results for the hadronic ‘comover’ scenario including additionally pre-hadronic interactions of charm according to (16) - (19) are displayed in terms of the upper (green solid) line with open circles for mid-rapidity  $J/\Psi$ 's ( $|y| \leq 0.35$ ) and in terms of the lower (orange dashed) line with open triangles for forward rapidity ( $1.2 \leq |y| \leq 2.2$ ). The figure is taken from Ref. <sup>82</sup>.

the large suppression at forward rapidities.

Consequently, in Ref. <sup>82</sup> additional interactions of charm with pre-hadrons (as described in Section 6.3) have been incorporated in the ‘comover scenario’ to have a first glance at the dominant effects. The  $J/\Psi$  suppression pattern in this case is shown in Fig. 35 in comparison to the same data as in Fig. 33 for the hadronic comover model. When including the pre-hadronic interactions, the suppression pattern for central and forward rapidities becomes rather similar to the data within the statistical accuracy of the calculations. Indeed, the ratio of  $R_{AA}$  at forward rapidity to mid-rapidity now follows closely the experimental trend as seen in Fig. 34 by the lower red solid line.

Some further information may be gained from the  $J/\Psi$  rapidity distributions in Au+Au collisions at RHIC. The latter distribution is shown in Fig. 36 in comparison to the PHENIX data for central collisions (upper l.h.s.), semi-central (upper r.h.s.), semi-peripheral (lower l.h.s.) and peripheral reactions (lower r.h.s.) for the standard ‘comover’ scenario (dashed blue lines) and the ‘comover’ model including additionally pre-hadronic interactions of charm according to (16) - (19) (solid red lines). Whereas for peripheral reactions these additional early interactions practically play no role, the additional pre-hadron elastic scattering lead to a narrowing

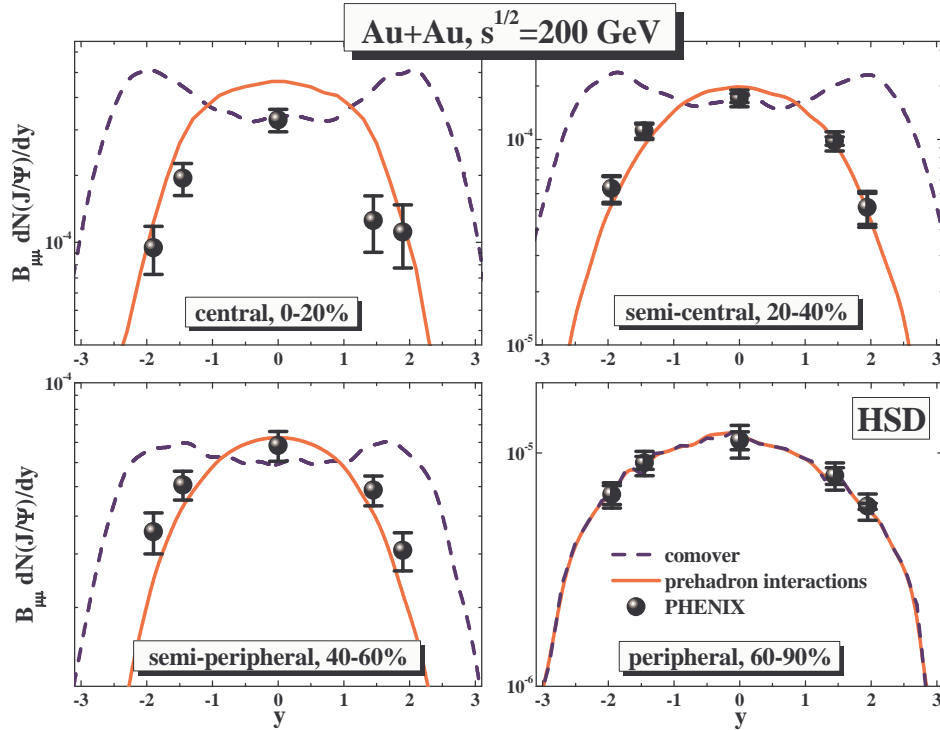


Fig. 36. The rapidity distribution  $dN_{J/\Psi}/dy$  for different centralities from the standard ‘comover’ model (dashed blue lines) and the ‘comover’ model with additional pre-hadronic interactions of charm according to (16) - (19) (solid red lines). The full dots show the respective data from the PHENIX Collaboration<sup>97</sup>. The calculated lines have been smoothed by a spline algorithm. The reactions are Au+Au at  $\sqrt{s} = 200$  GeV. The figure is taken from Ref.<sup>82</sup>.

of the  $J/\Psi$  rapidity distribution with the centrality of the collision (roughly in line with the data). In the standard ‘comover’ model an opposite trend is seen: here the interactions of charmonia with formed hadrons produce a dip in the rapidity distribution at  $y \approx 0$  which increases with centrality since the density of formed hadrons increases accordingly around mid-rapidity. Since the total number of produced  $c\bar{c}$  pairs is the same (for the respective centrality class) and detailed balance is incorporated in the reaction rates, we find a surplus of  $J/\Psi$  at more forward rapidities. The net result is a broadening of the  $J/\Psi$  rapidity distribution with centrality in the purely hadronic scenario opposite to the trend observed in experiment.

In summarizing the results at RHIC energies, the hadronic ‘comover’ dynamics for charmonium dissociation and recreation as well as the charmonium ‘melting’ scenario do not match the general dependence of the  $J/\Psi$  on rapidity and centrality as seen by the PHENIX Collaboration. In fact, a narrowing of the  $J/\Psi$  rapidity distribution cannot be achieved by comover interactions with formed hadrons,

since the latter appear too late in the collision dynamics. Only when including early pre-hadronic interactions with charm, a dynamical narrowing of the charmonium rapidity distribution with centrality can be achieved, as demonstrated within the pre-hadronic interaction model. Consequently, the PHENIX data on  $J/\Psi$  suppression indicate the presence and important impact of pre-hadronic or partonic interactions in the early charm dynamics. This finding is in line with earlier studies in Refs. 47,168,169 demonstrating the necessity of non-hadronic degrees of freedom in the early reaction phase of nucleus-nucleus collisions at RHIC energies for the description of the elliptic flow  $v_2$ , the suppression of hadrons at high transverse momentum  $p_T$  and far-side jet suppression.

#### 7.4. Charmonia excitation functions

In this Section we present the excitation functions for the  $J/\Psi$  survival probability in Au + Au collisions from FAIR to top RHIC energies in the different scenarios in order to allow for a further distinction between the different concepts. The results of HSD calculations are presented in the upper part of Fig. 37 for the ‘QGP threshold melting + hadronic recombination’ scenario (dashed green lines with open triangles) and the ‘comover absorption + recombination’ model (solid red lines with open circles) for central (l.h.s.) and minimum bias (r.h.s.) Au+Au reactions as a function of the beam energy. The  $J/\Psi$  survival probability  $S_{J/\Psi}$  is defined as

$$S_{J/\Psi} = \frac{N_{fin}^{J/\Psi}}{N_{BB}^{J/\Psi}}, \quad (23)$$

where  $N_{fin}^{J/\Psi}$  and  $N_{BB}^{J/\Psi}$  denote the final number of  $J/\Psi$  mesons and the number of  $J/\Psi$ 's produced initially by  $BB$  reactions, respectively. We find that from FAIR energies of 20 - 40 A·GeV up to top SPS energies of 158 A·GeV there is no significant difference between the two models for the  $J/\Psi$  survival probability in case of central collisions. The differences here show up mainly in the full RHIC energy range where the ‘QGP threshold melting + hadronic recombination’ scenario leads to substantially lower  $J/\Psi$  survival probabilities. In case of minimum bias collisions the ‘comover absorption + recombination’ model (solid lines) gives a roughly energy independent  $J/\Psi$  survival probability, whereas the ‘QGP threshold melting + hadronic recombination’ scenario shows lower  $J/\Psi$  survival probabilities (lower dashed green lines) for laboratory energies above  $\sim 100$  A·GeV due to a larger initial melting of  $J/\Psi$ -mesons at high energy density.

A clearer distinction between the different concepts is offered by the excitation functions for the  $\Psi'$  to  $J/\Psi$  ratio in Au + Au collisions. The calculated results are shown in the lower part of Fig. 37 for the ‘QGP threshold melting + hadronic recombination’ scenario (dashed green lines with open triangles) and the ‘comover absorption + recombination’ model (solid red lines) for central (l.h.s.) and minimum bias reactions (r.h.s.). Here the  $\Psi'$  is already melting away in central Au+Au reactions in the ‘QGP threshold melting’ scenario at bombarding energies above 40



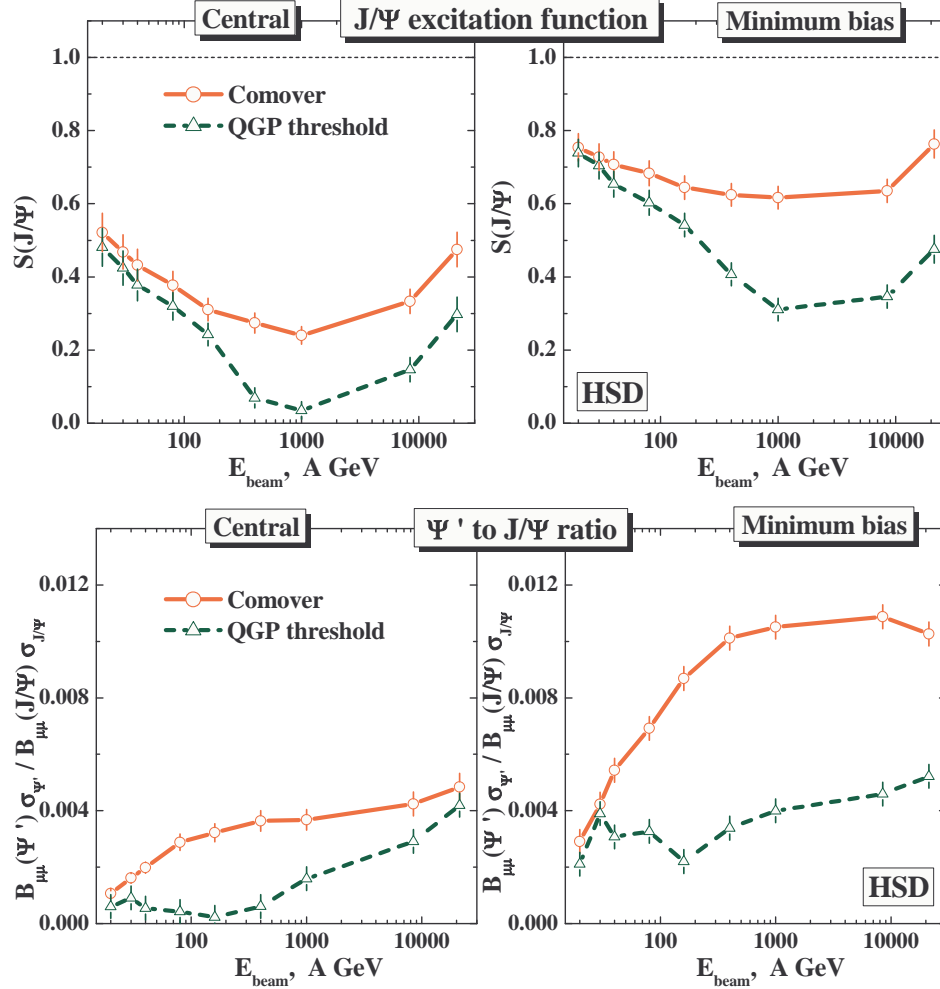


Fig. 37. upper part: The excitation function for the  $J/\Psi$  survival probability in the ‘QGP threshold melting + hadronic recombination’ scenario (dashed green lines with triangles) and the ‘comover absorption + recombination’ model (solid red lines with circles) for central (l.h.s.) and minimum bias Au+Au reactions (r.h.s.) as a function of the beam energy. Lower part: The  $\Psi'$  to  $J/\Psi$  ratio for the same reactions as in the upper part of the figure in the ‘QGP threshold melting + hadronic recombination’ scenario (dashed green lines with triangles) and the ‘comover absorption + recombination’ model (upper solid red lines with circles). The figure is taken from Ref. <sup>82</sup>.

A-GeV, whereas a substantial amount of  $\Psi'$  survives in the ‘comover absorption + recombination’ model. Thus measurements of  $\Psi'$  suppression at the lower SPS or top FAIR energies will clearly distinguish between the different model concepts.

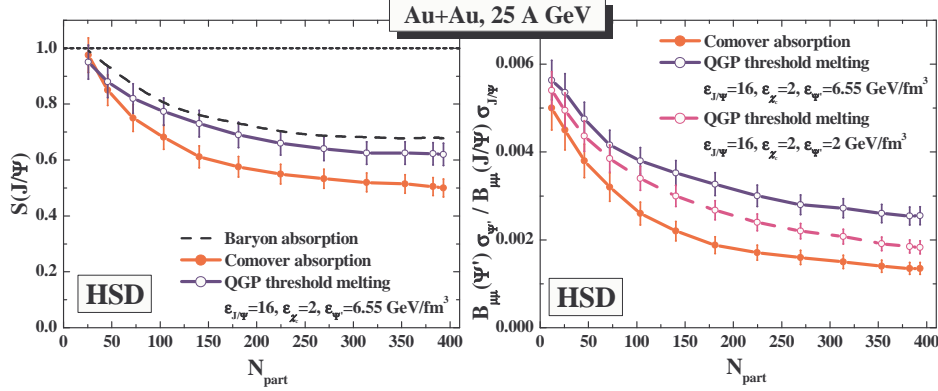


Fig. 38. The survival probability  $S_{J/\Psi}$  (left plot) and ratio  $\Psi'$  to  $J/\Psi$  (right plot) as a function of the number of participants  $N_{part}$  in Au+Au reactions at 25 A-GeV. The blue lines (with open dots) reflect the ‘threshold scenario’ for  $\epsilon_{J/\Psi} = 16 \text{ GeV/fm}^3$ ,  $\epsilon_{\chi_c} = 2 \text{ GeV/fm}^3$ ,  $\epsilon_{\Psi'} = 6.55 \text{ GeV/fm}^3$  while the violet line (the lower line with open dots on the r.h.s.) stands for the ‘threshold scenario’ for  $\epsilon_{J/\Psi} = 16 \text{ GeV/fm}^3$ ,  $\epsilon_{\chi_c} = 2 \text{ GeV/fm}^3$ ,  $\epsilon_{\Psi'} = 2 \text{ GeV/fm}^3$ . The solid red lines (full dots) denote the results for the comover absorption model with the standard matrix element squared  $|M_0|^2 = 0.18 \text{ fm}^2/\text{GeV}^2$ . The dashed line (l.h.s.) represents the HSD calculations including only dissociation channels with nucleons. The figure is taken from Ref. <sup>44</sup>.

### 7.5. FAIR energies

The CBM Collaboration at GSI is aiming at charmonium measurements in heavy-ion collisions at the future FAIR facility <sup>187</sup>. This opens up the possibility to explore the charmonium suppression mechanism at lower bombarding energies of about 25 A-GeV in Au+Au collisions. The corresponding HSD predictions are displayed in Fig. 38 for the survival probability  $S_{J/\Psi}$  (l.h.s.) and the ratio  $\Psi'$  to  $J/\Psi$  (r.h.s.) as a function of the number of participants  $N_{part}$ . The violet line in Fig. 38 stands for the ‘threshold scenario’ with  $\epsilon_{\Psi'}$ , i.e.  $\epsilon_{J/\Psi} = 16 \text{ GeV/fm}^3$ ,  $\epsilon_{\chi_c} = 2 \text{ GeV/fm}^3$ ,  $\epsilon_{\Psi'} = 2 \text{ GeV/fm}^3$ . The solid red lines denote the results for the comover absorption model with the standard matrix element squared  $|M_0|^2 = 0.18 \text{ fm}^2/\text{GeV}^2$ .

We note that in Au+Au reactions at 25 A-GeV in the ‘threshold scenario’ (solid line with open dots in the left plot) only a very low amount of  $\chi_c$  and no  $J/\Psi$  are melted at the energy densities reached in these reactions. On the other hand the comover density decreases only moderately when stepping down in energy from 158 A-GeV to 25 A-GeV such that the  $J/\Psi$  survival probability in the comover absorption model (lower solid line in the left part) is lower. This is even more pronounced for the  $\Psi'$  to  $J/\Psi$  ratio versus centrality, which in the ‘threshold melting scenario’ (middle line in the right part) is clearly above the result achieved in the comover absorption model (lower line in the right part). Consequently, the different dissociation scenarios may well be distinguished in future charmonium measurements at FAIR.

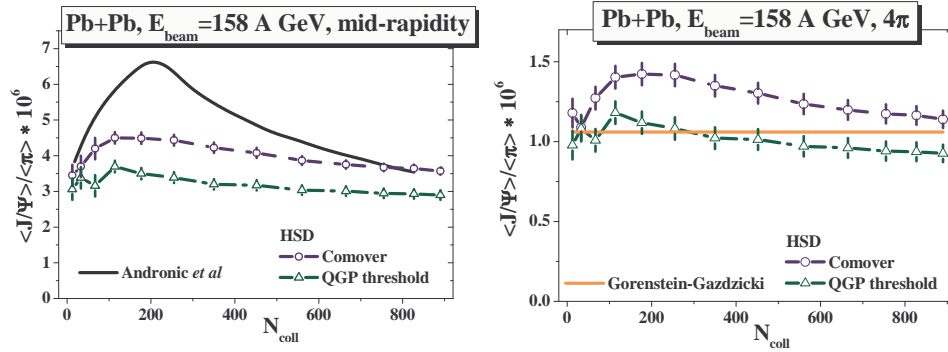


Fig. 39. Ratio of the averaged  $J/\Psi$  to  $\pi$  multiplicity for  $Pb + Pb$  at the SPS beam energy of 158 A·GeV at mid-rapidity (l.h.s.) and in full  $4\pi$  acceptance (r.h.s.) as a function of the number of binary collisions  $N_{coll}$  for the different suppression scenarios implemented in HSD - the ‘comover’ model (dashed blue line with open circles) and the ‘threshold melting’ scenario (green dot-dashed line with open triangles) - in comparison to the statistical model by Gorenstein and Gazdzicki<sup>134</sup> (r.h.s.; straight orange line) and the statistical hadronization model by Andronic *et al.*<sup>186</sup> (l.h.s.; solid black line). The figure is taken from Ref.<sup>82</sup>.

## 8. Testing the assumption of statistical hadronization

The assumption of statistical hadronization – *i.e.* of  $J/\Psi$ ’s being dominantly produced at hadronization in a purely statistically fashion according to available phase space and the number of available  $c$  and  $\bar{c}$  quarks – leads to a scaling of the  $\langle J/\Psi \rangle / \langle h \rangle$  ratio with the system size<sup>134</sup>, where  $\langle h \rangle$  is the average hadron multiplicity. Since  $\langle h \rangle \sim \langle \pi \rangle$ , the ratio  $\langle J/\Psi \rangle / \langle \pi \rangle$  has been calculated in HSD in the different scenarios for charmonium suppression:

- ‘threshold melting’ + recombination via  $D\bar{D} \rightarrow c\bar{c} + m$  including the backward reactions  $c\bar{c} + m \rightarrow D\bar{D}$ ,
- hadronic (‘comover’) absorption:  $D\bar{D} \rightarrow c\bar{c} + m$  and the backward reactions  $c\bar{c} + m \rightarrow D\bar{D}$ ;
- ‘prehadron interactions’:  $D\bar{D} \rightarrow c\bar{c} + m$  and the backward reactions  $c\bar{c} + m \rightarrow D\bar{D}$  as well as early pre-hadronic charm interactions as described in Section 6.3.

The results of the calculations are shown in Fig. 39 together with the prediction of the statistical model of Gorenstein and Gazdzicki<sup>134</sup> for the full phase space (straight orange line; r.h.s.) and the statistical hadronization model by Andronic *et al.*<sup>186,188</sup> for mid-rapidity (solid black line; l.h.s.) for Pb+Pb at 158 A·GeV. The centrality dependence here is given by the number of initial binary collisions  $N_{coll}$ . The actual comparison in Fig. 39 indicates that the statistical model by Andronic *et al.*<sup>186</sup> predicts a sizeably larger  $J/\Psi$  to  $\pi$  ratio at midrapidity for peripheral and semi-peripheral reactions than the microscopic HSD results for the different scenarios. For central reactions - where an approximate equilibrium is achieved -

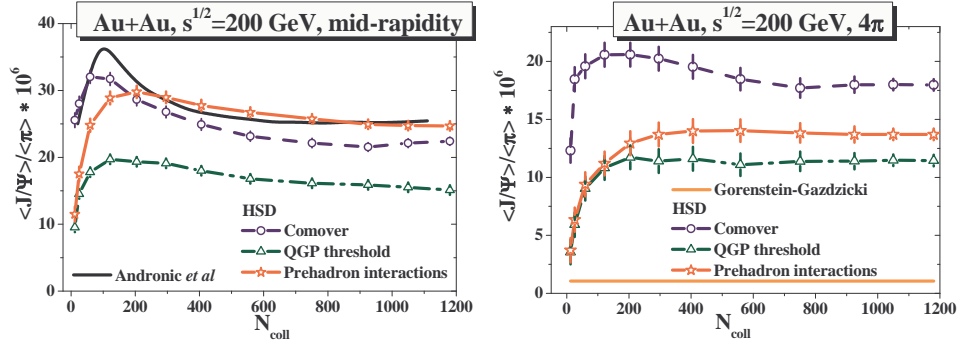


Fig. 40. Same as Fig. 39 but for  $Au + Au$  at the top RHIC energy of  $\sqrt{s} = 200$  GeV. The red solid line shows additionally the result of the ‘comover’ model including the pre-hadronic charm interactions (see text). The figure is taken from Ref. 82.

all scenarios give roughly the same ratio. In full  $4\pi$  phase space the HSD results indicate also a slightly higher  $J/\Psi$  to  $\pi$  ratio in the ‘comover’ model relative to the ‘melting’ scenario but both ratios only weakly depend on centrality - roughly in line with the statistical model of Gorenstein and Gazdzicki<sup>134</sup> (orange straight line). Consequently, only peripheral reactions of heavy nuclei might be used to disentangle the different scenarios at top SPS energies at midrapidity (or in full phase space).

The situation is different for  $Au+Au$  collisions at the top RHIC energy as may be extracted from Fig. 40 where the  $J/\Psi$  to pion ratio (l.h.s.: at mid-rapidity; r.h.s.: for  $4\pi$  acceptance) is shown as a function of  $N_{coll}$ . The standard ‘comover’ model (dashed blue lines) is only presented for reference but is unrealistic according to the analysis in Section 7. We find that the ‘comover’ model with early pre-hadronic charm interactions (solid red line with stars, l.h.s.) is very close to the statistical hadronization model<sup>186</sup> (solid black line) at mid-rapidity except for very peripheral collisions. The ‘threshold melting’ scenario follows the trend in centrality but is down by about 30%. Thus at mid-rapidity there is no essential extra potential in differentiating the scenarios. Considering the full  $4\pi$  acceptance (r.h.s.) one finds a practically constant  $J/\Psi$  to pion ratio for  $N_{coll} > 200$  from the HSD calculations as expected from the statistical model, however, the early model of Gorenstein and Gazdzicki<sup>134</sup> is down by about a factor of  $\sim 10$  (and may be ruled out by present data). The latter conclusion is in agreement with the independent analysis in Ref. 137.

## 9. Transverse mass spectra

Apart from rapidity dependent particle abundances, also the dynamics in the transverse direction (to the beam) provides relevant information.

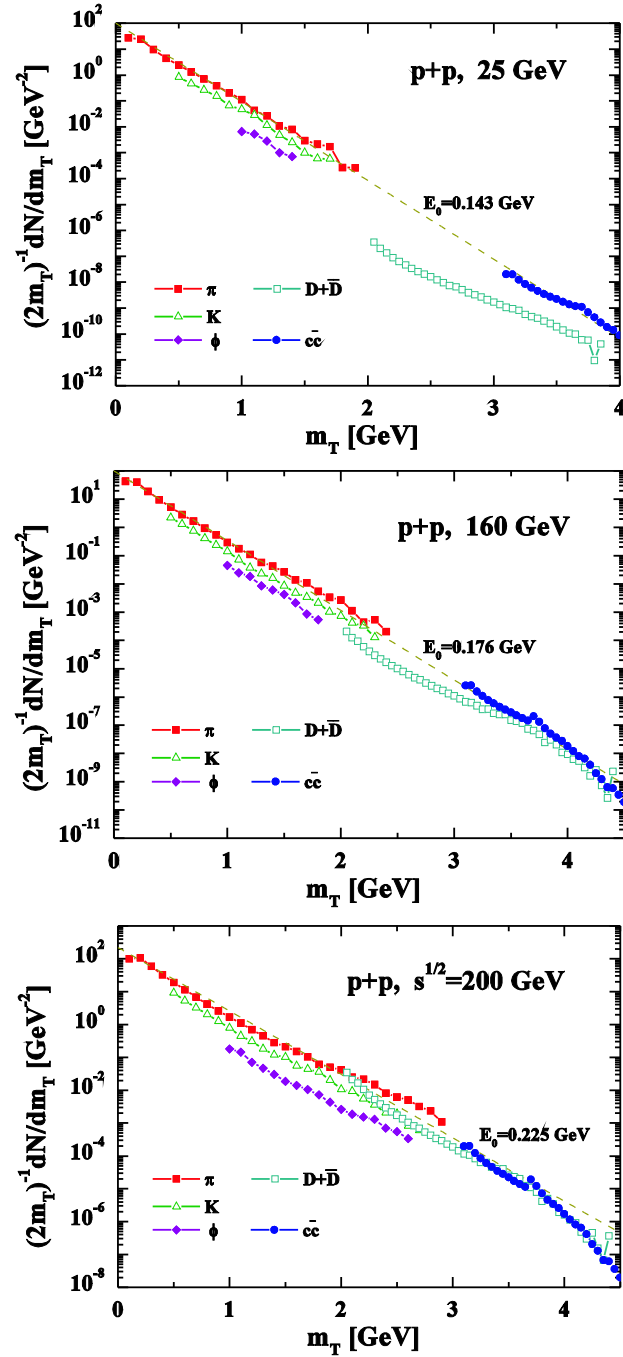


Fig. 41. Upper plot: The transverse mass spectra from  $pp$  collisions at  $T_{lab} = 25$  GeV for pions (full squares), kaons (open triangles), and  $\phi$ -mesons (full rhombi) from the string model as implemented in HSD. The dashed line shows an exponential with slope parameter  $E_0 = 0.143$  GeV. Middle plot: The same as the upper plot, but for  $pp$  reactions at  $T_{lab} = 160$  GeV. The dashed line shows an exponential with slope parameter  $E_0 = 0.176$  GeV. Lower plot: The same as the upper plot, but for  $pp$  reactions at  $\sqrt{s} = 200$  GeV. The dashed line shows an exponential with slope parameter  $E_0 = 0.225$  GeV. The figures are taken from Ref. <sup>33</sup>.

### 9.1. Elementary collisions

We recall again that HSD successfully reproduces the measured transverse mass  $m_T = \sqrt{p_T^2 + m_X^2}$  spectra of pions and kaons in  $pp$  collisions for bombarding energies of 12 GeV, 24 GeV as well as for collisions at  $\sqrt{s} = 200$  GeV<sup>66</sup>. In Fig. 41 we present additionally the corresponding spectra for  $\phi$ -mesons,  $D + \bar{D}$  mesons and charmonia at SPS, RHIC and FAIR energies. We display the differential multiplicities  $(2m_T)^{-1}dN_X/dm_T$  in the transverse mass. The pion spectra describe the sum of  $\pi^+, \pi^0, \pi^-$ , the kaon spectra the sum of  $K^+, K^0, \bar{K}^0, K^-$ , the  $D$ -meson spectra the sum of all  $D, D^*, D_s, D_s^*$  and their antiparticles while the spectrum denoted by  $c\bar{c}$  includes the  $J/\Psi$ , the  $\chi_c$  as well as the  $\Psi'$ , where the latter contribution starts at  $m_T \approx 3.7$  GeV and becomes visible as a tiny kink in the  $m_T$ -spectra. Here the open charm and charmonia results stem from the parametrizations specified in Section 2 (including the decay  $\chi_c \rightarrow J/\Psi + \gamma$ ), while the spectra for pions, kaons and  $\phi$ -mesons are from the LUND string model as implemented in the HSD transport approach. For orientation, we also show exponential spectra with slope parameters of 143 MeV, 176 MeV and 225 MeV, respectively, which describe the  $m_T$ -spectra of pions rather well. The kaon spectra at all energies are down by a factor of  $\sim 3$ , the  $\phi$  spectra by a factor of 9-10 relative to this line due to strangeness suppression in  $pp$  collisions. However, it is quite remarkable that the charmonia spectra fit well to this approximate  $m_T$ -scaling (within a factor of 2-3) at  $\sqrt{s} = 7.1, 17.3$  and 200 GeV, respectively. Furthermore, the spectrum of open charm is roughly compatible with  $m_T$ -scaling at  $\sqrt{s} = 17.3$  and 200 GeV, while the  $D, \bar{D}$  mesons are suppressed relative to the scaling by a factor  $\sim 30$  close to threshold ( $\sqrt{s} = 7.1$  GeV). Such an ‘apparent’ statistical production of mesons in elementary reactions has been advocated before by Becattini<sup>189</sup>. We have to stress, however, that all these observations on the charm sector are based on our extrapolations (Section 2) and have to be checked experimentally.

### 9.2. SPS and RHIC energies

As mentioned before (cf. Ref.<sup>66</sup>) the hadron spectra at high  $m_T$  are underestimated both in HSD and UrQMD compared to the data at energies from SPS to RHIC. Nevertheless, it is illustrative to have a global view on the transverse mass spectra of hadrons with different flavor in case of central Au+Au collisions. In this respect Fig. 42 displays the results of the hadronic transport at SPS and RHIC energies which illustrates an approximate meson  $m_T$ -scaling for all flavors (cf. Ref.<sup>33</sup>). The  $m_T$ -scaling for pions, kaons,  $D$ -mesons and  $J/\Psi$  in central collisions of Au + Au at top SPS and RHIC energies is essentially due to an approximate  $m_T$ -scaling in  $pp$  collisions at  $\sqrt{s} = 17.3$  GeV and substantial  $D, \bar{D}$  and  $J/\Psi$  final state interactions in the nucleus-nucleus case.

We recall that the measured transverse mass spectra of hadrons (heavier than pions) at AGS, SPS and RHIC energies show a ‘hardening’ in central Au+Au collisions relative to  $pp$  interactions (cf. Ref.<sup>13</sup>) for low transverse mass or momentum.

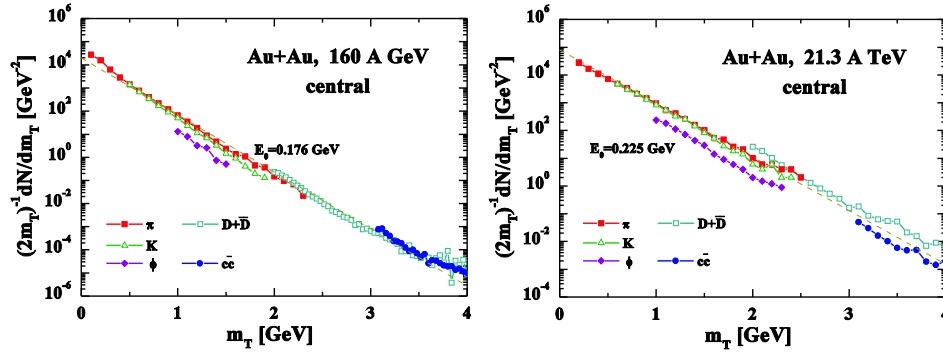


Fig. 42. Left panel: The transverse mass spectra of pions (full squares), kaons (open triangles),  $\phi$ -mesons (full rhombi),  $D + \bar{D}$  mesons (open squares) and  $J/\Psi, \Psi'$  mesons (full dots) in the HSD approach for a central  $Au + Au$  collision at 160 A·GeV. The thin dashed line shows an exponential with slope parameter  $E_0 = 0.176$  GeV. Right panel: Same as left panel, but at top RHIC energy of 21.3 A·TeV. The thin dashed line shows an exponential with slope parameter  $E_0 = 0.225$  GeV. Both figures are taken from Ref. 33.

This hardening is commonly attributed to collective flow, which is absent in the respective  $pp$  or  $pA$  collisions. Consequently it is important to get precise data on open charm and charmonium transverse momentum ( $p_T$ ) spectra, since their slope might give information on the pressure generated in a possible early partonic phase<sup>190</sup>. This argument is expected to hold especially for  $J/\Psi$  mesons, since their elastic rescattering cross section with hadrons should be small in the hadronic expansion phase<sup>191,192</sup> (see also Section 10).

### 9.3. FAIR energies

In contrast to the observation at SPS energy, the approximate  $m_T$ -scaling for pions, kaons,  $D$ -mesons and  $J/\Psi$  no longer holds for central collisions of  $Au+Au$  at 25 A·GeV as demonstrated in Fig. 43. Here the HSD calculations show a suppression of  $D$ -mesons by a factor of  $\sim 10$  relative to the global  $m_T$ -scaling - characterized by a slope of 143 MeV - if no  $D$ -meson self energies are accounted for.

On the other hand, attractive mass shifts of  $D, \bar{D}$  mesons of -50 MeV at  $\rho_0$  might be expected due to hadronic interaction models when extending  $SU(3)_{flavor}$  to  $SU(4)_{flavor}$  symmetry<sup>193</sup>. At the densities of 5-8  $\rho_0$  chiral symmetry should be restored, i.e. the large  $\langle q\bar{q} \rangle$  condensate of the nonperturbative vacuum should have disappeared. Accordingly, the production of  $c\bar{c}$  pairs in the ‘new’ perturbative vacuum might be enhanced since only the invariant mass of a  $c\bar{c}$  has to be produced e.g. by gluon-gluon fusion. Accordingly, the threshold for  $D\bar{D}$  production - which is  $\sim 3.739$  GeV in vacuum - might be reduced by  $\approx 2 \cdot 0.35$  GeV = 0.7 GeV in the chirally restored phase to about 3 GeV, only. Such a reduction of the  $c\bar{c}$  production threshold leads to an enhancement of open charm mesons by about a factor of 7 (magenta crosses in Fig. 43) such that an approximate  $m_T$ -scaling for all mesons

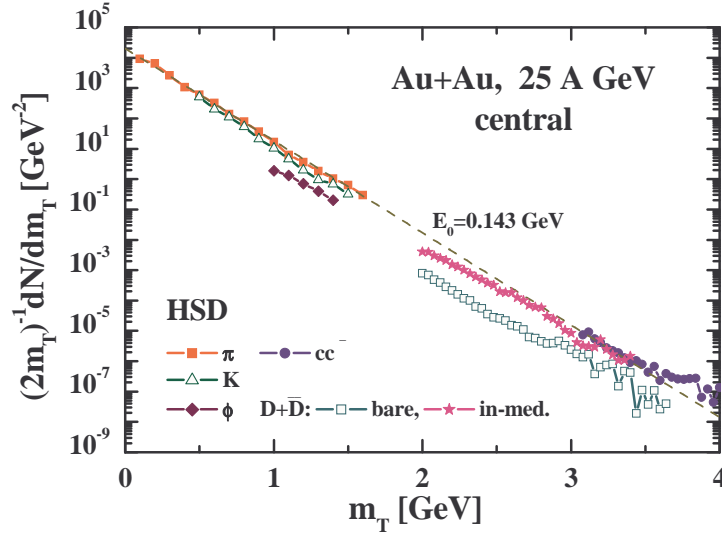


Fig. 43. The transverse mass spectra of pions (full squares), kaons (open triangles),  $\phi$ -mesons (full rhombi),  $D + \bar{D}$  mesons (open squares) and  $J/\Psi, \Psi'$  mesons (full dots) in the HSD approach for a central Au+Au collision at 25 A-GeV without including self energies for the mesons. The crosses stand for the  $D$ -meson  $m_T$  spectra when including an attractive mass shift of  $-50\rho/\rho_0$  MeV. The thin dashed line shows an exponential with slope parameter  $E_0 = 0.143$  GeV. Note that final state elastic scattering of kaons and  $\phi$ -mesons with pions has been discarded in the calculations. The figure is taken from Ref. 30.

is regained. Thus, a global  $m_T$  scaling of all mesons may be regarded as a strong medium effect on the charmed hadrons and as a signature for a chirally restored phase – if observed by CBM.

## 10. High $p_T$ quenching of open charm and charmonia

A significant suppression of high transverse momentum hadrons in Au+Au collisions compared to  $pp$  is observed at RHIC energies of  $\sqrt{s} = 200$  GeV 197,198,199,200 and is attributed to the energy loss of highly energetic particles in a hot colored medium (QGP) 201,202. In fact, the recent observation by the PHENIX 203, STAR 204 and BRAHMS 200 collaborations that a similar suppression is not observed in d+Au interactions at mid-rapidity at the same energy supports this idea.

Vigorous theoretical efforts are under way to understand parton energy loss in terms of perturbative QCD (pQCD). Various groups have described the suppression of light hadrons in terms of radiative energy loss by gluon bremsstrahlung. According to such calculations, charm and beauty quarks should be absorbed significantly less than light quarks and gluons due to their higher mass. However, data from the PHENIX and STAR experiments, which compare the production in nucleus-nucleus to proton-proton collisions of high- $p_T$  "non-photonic" electrons (which originate



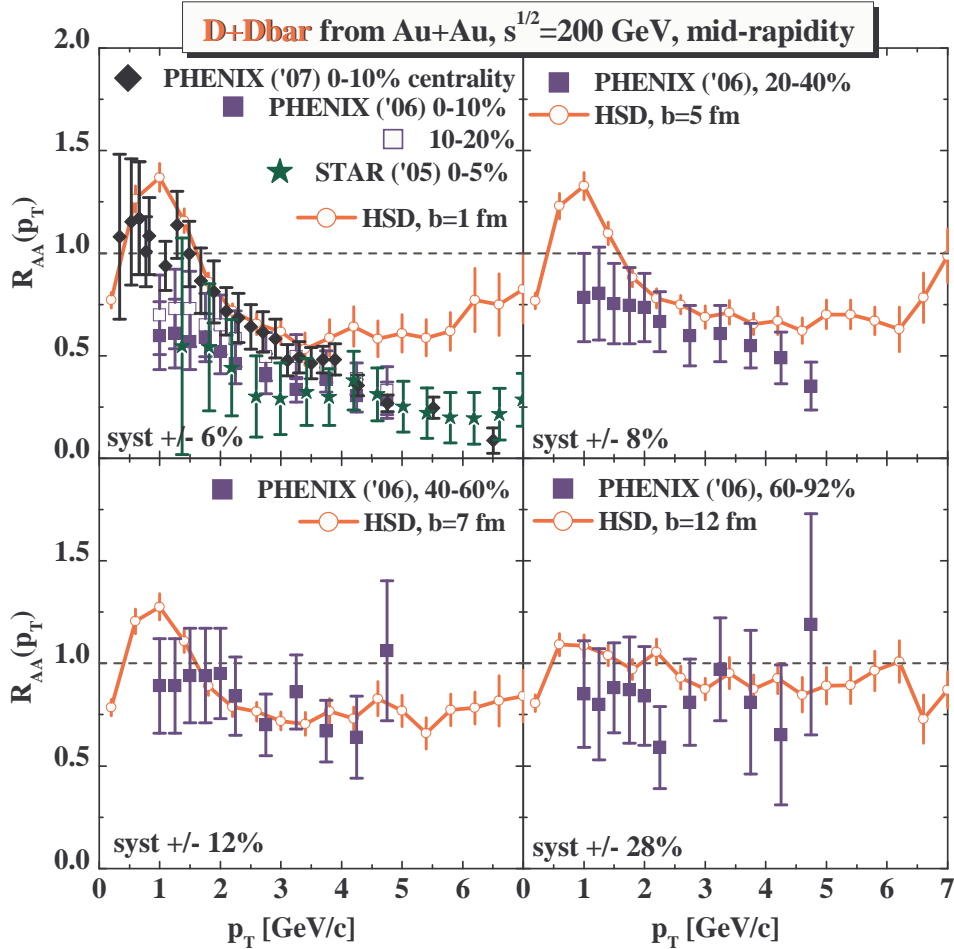


Fig. 44. HSD predictions for the ratio of the final to the initial (i.e. at the production point) transverse momentum spectra of  $D + \bar{D}$ -mesons (solid lines with open dots, color: blue) from Au + Au collisions at  $\sqrt{s} = 200$  GeV for  $b = 1, 5, 7$  and  $12$  fm at mid-rapidity as calculated in Ref. <sup>94</sup>. The PHENIX data from Ref. <sup>194</sup> (denoted '06) and from Ref. <sup>195</sup> (denoted '07) on  $R_{AA}$  of non-photonic electrons as well as the STAR data from Ref. <sup>196</sup> have been added later.

mainly from heavy-flavor decays) seem to indicate that heavy quarks lose energy in a comparable fashion as light quarks.

In order to quantify the effect of hadronic final state interactions, we show in Fig. 44 the HSD predictions from Ref. <sup>94</sup> for the ratio of the final to the initial transverse  $p_T$  spectra of  $D + \bar{D}$ -mesons (solid lines with open dots, color: blue) from Au + Au collisions at  $\sqrt{s} = 200$  GeV calculated for impact parameter  $b = 1, 5, 7$  and  $12$  fm at midrapidity. HSD predicts an enhancement of  $D, \bar{D}$  mesons at low momenta with a maximum at  $p_T \approx 1$  GeV/c and a relative suppression for  $p_T > 2$  GeV/c.

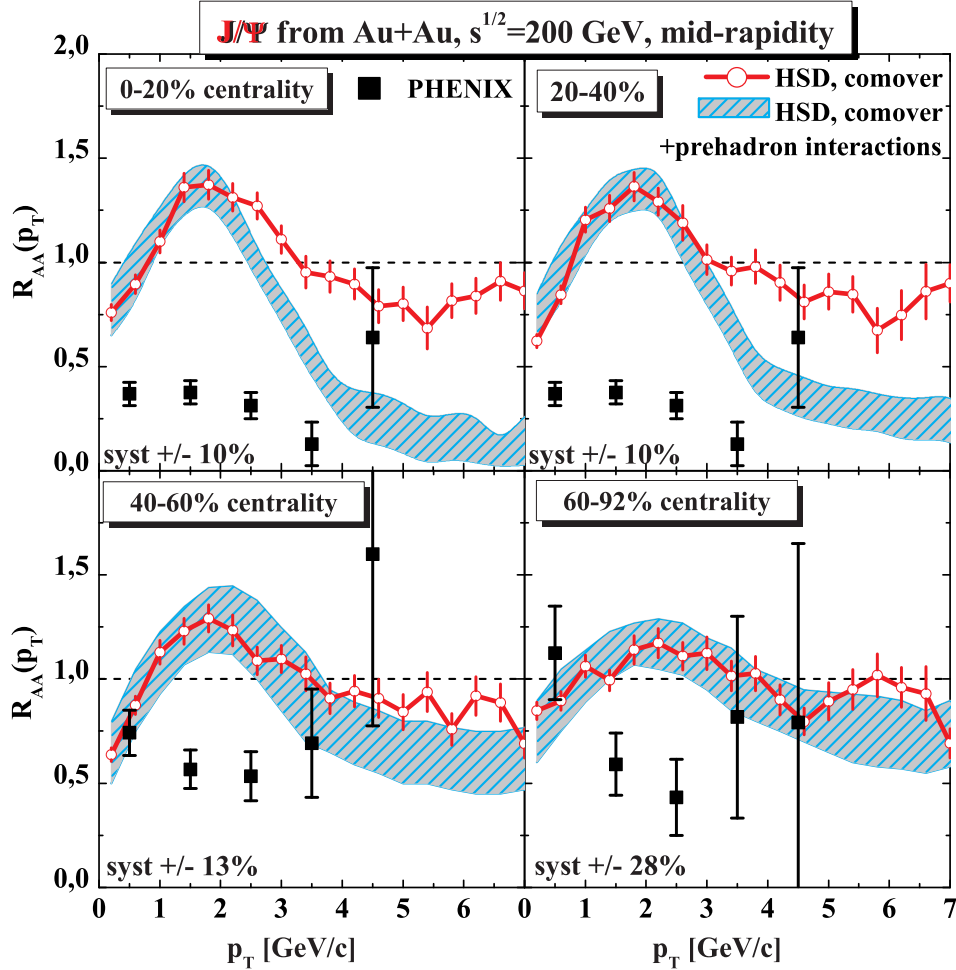


Fig. 45. HSD predictions for the ratio of the final to the initial  $p_T$  spectra of  $J/\Psi$ -mesons (solid lines with open dots, color: red) from Au + Au collisions at  $\sqrt{s} = 200$  GeV for  $b = 1, 5, 7$  and 12 fm at mid-rapidity as calculated in Ref. <sup>94</sup>. The preliminary PHENIX data for  $R_{AA}(J/\Psi)$  from Ref. <sup>97</sup> have been added later. The grey dashed bands represent the results from the extended version of the HSD comover approach, in which prehadron interactions are taken into account as described in Section 6.3.

These effects increase with the centrality of the Au+Au collision. We note that the maxima in the ratios disappear when switching off the rescattering with mesons in the transport approach. Thus a collective acceleration of the  $D + \bar{D}$  mesons occurs also via elastic scattering with mesons. As seen in Fig. 44 the suppression seen by PHENIX may well be explained by hadronic comover interactions up to transverse momenta about 4 GeV/c. Only for higher  $p_T$  a clear signal for parton energy loss - either gluon bremsstrahlung or parton elastic scattering - may be extracted in

comparison to the data!

The suppression pattern  $R_{AA}(J/\Psi)$  from HSD (in the comover scenario) is quite analogous to that of  $D$ -mesons for different centrality showing a slight maximum for transverse momenta of  $\sim 2$  GeV/c and a steady decrease for higher  $p_T$ . In Fig. 45 the predictions (from Ref. <sup>94</sup>) for the ratio of the final to the initial transverse  $p_T$  spectra of  $J/\Psi$ -mesons (solid red lines with open dots) as well as new calculations in the extended version of the comover approach – as described in Section 6.3 (grey dashed bands) – from Au + Au collisions at  $\sqrt{s} = 200$  GeV for four different centrality regions at mid-rapidity are displayed. The preliminary PHENIX data for  $R_{AA}(J/\Psi)$  from Ref. <sup>97</sup> - added later - show a substantially different pattern especially for non-peripheral interactions. The strong suppression for low  $p_T$   $J/\Psi$  mesons seen experimentally suggests that not primordial  $J/\Psi$ 's are accelerated during the dynamical evolution but that at least a part of initially formed  $J/\Psi$ 's are dissolved and created later e.g. by  $c\bar{c}$  coalescence. We stress that the reformation of charmonia in the hadronic phase (by  $D + \bar{D}$  etc.) carries the flow from the  $D$ -mesons and thus does not lead to suppression at small  $p_T$  as seen experimentally. This observation supports the idea that part of the charmonia are produced in the hadronization process!

## 11. Collective flow

A further possible way to disentangle hadronic from partonic dynamics is the elliptic flow  $v_2(y, p_T)$  as a function of the rapidity  $y$  and transverse momentum  $p_T$ . The flow  $v_2(y, p_T)$  is driven by different pressure gradients in case of non-vanishing spatial anisotropy

$$\epsilon_2 = \langle \frac{y^2 - x^2}{y^2 + x^2} \rangle. \quad (24)$$

Since  $\epsilon_2$  decreases fast during the expansion of a noncentral nucleus-nucleus reaction, the magnitude of  $v_2$  gives information about the interaction strength or interaction rate of the early medium.

The phenomenon of collective flow can generally be characterized in terms of anisotropies of the azimuthal emission pattern, expressed in terms of a Fourier series

$$\frac{dN}{d\phi}(\phi) \propto 1 + 2v_1 \cos(\phi) + 2v_2 \cos(2\phi) + \dots \quad (25)$$

which allows a transparent interpretation of the coefficients  $v_1$  and  $v_2$ . The dipole term  $v_1$  arises from a collective sideward deflection of the particles in the reaction plane and characterizes the transverse flow in the reaction plane (the “bounce-off”). The second harmonic describes the emission pattern perpendicular to the reaction plane. For negative  $v_2$  one has a preferential out-of-plane emission, called *squeeze-out*. Pions at SIS energies exhibit a clear out-of-plane preference <sup>205,206</sup> which is due to shadowing by spectator nucleons <sup>52</sup>.

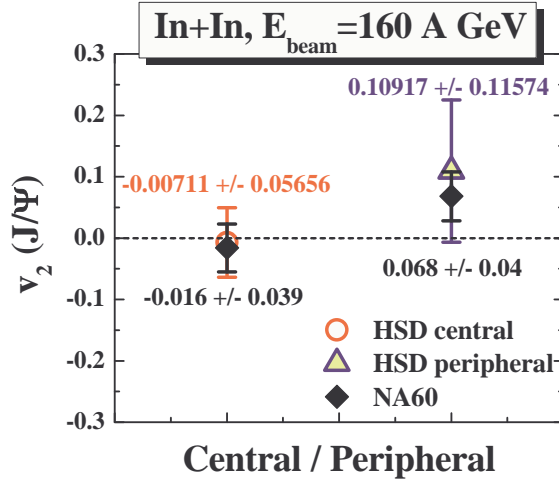


Fig. 46. Elliptic flow  $v_2$  of  $J/\Psi$ 's produced in central and peripheral  $In+In$  collisions at 158 A-GeV beam energy in the hadronic 'comover' mode of HSD (open circle and open triangle) compared to the NA60 data<sup>211</sup> represented by black diamonds. The figure is taken from Ref. 82.

Presently, the most employed flow observables are the in-plane and elliptic flows<sup>207</sup>:

$$v_1 = \left\langle \frac{p_x}{p_T} \right\rangle, \quad v_2 = \left\langle \frac{p_x^2 - p_y^2}{p_x^2 + p_y^2} \right\rangle. \quad (26)$$

Here,  $p_x$  denotes the momentum in  $x$ -direction, i.e. the transverse momentum within the reaction plane and  $p_y$  the transverse momentum out of the reaction plane. The total transverse momentum is given as  $p_T = \sqrt{p_x^2 + p_y^2}$ ; the  $z$ -axis is in the beam direction. The bounce-off, the squeeze-out and the antiflow<sup>208,209</sup> (third flow component<sup>60</sup>) have been suggested as differential barometers for the properties of compressed, dense matter from SIS to RHIC. In particular, it has been shown<sup>210,208</sup> that the disappearance or "collapse" of flow might be a direct result of a first order phase transition.

### 11.1. SPS energies

In Fig. 46 we compare the HSD result for  $v_2(J/\Psi)$  at SPS in the purely hadronic 'comover' scenario in comparison to the data for  $v_2(J/\Psi)$  of the NA60 collaboration for  $In+In$  collisions<sup>211</sup>. In central collisions the elliptic flow is practically zero both in the calculation as well as in the experiment, whereas in peripheral reactions a nonzero flow emerges. The agreement (within error bars) between the theory and the data indicates that, in line with the reproduction of the  $J/\Psi$  suppression data<sup>44</sup> (see Section 7.1), the low amount of  $v_2$  does not point towards additional strong partonic interactions at SPS energies. Consequently, the present measurements of

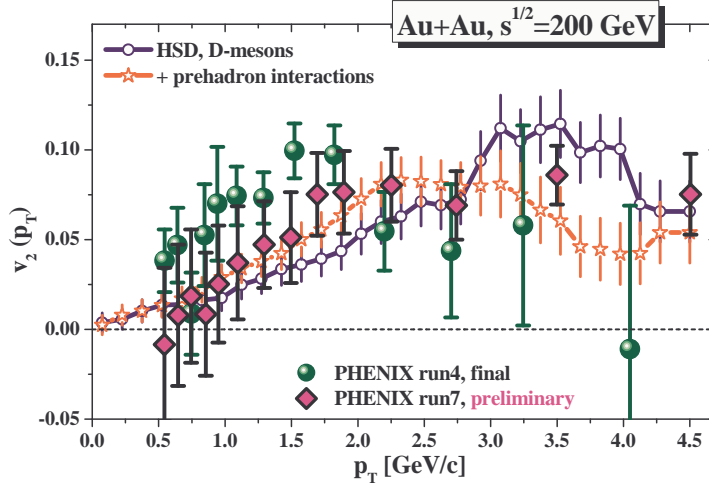


Fig. 47. Elliptic flow of  $D$ -mesons produced in  $Au + Au$  collisions at  $\sqrt{s} = 200$  GeV as a function of  $p_T$  from HSD (solid blue line with open circles) in comparison to the PHENIX data<sup>195</sup> on  $v_2$  of non-photonic electrons. The red line with open stars shows the HSD result for the  $v_2$  of  $D$ -mesons when including additionally pre-hadronic charm interactions as described in Section 6.3. The figure is taken from Ref.<sup>82</sup>.

$J/\Psi$  elliptic flow (at SPS energies) do not provide further constraints on the model assumptions.

### 11.2. RHIC energies

The situation, however, is different for the collective flow of  $D$ -mesons at top RHIC energies. Though collective flow can be described very elegantly in hydrodynamics (*cf.* Refs.<sup>215,216,217,218</sup>) by a proper choice of initial conditions, one has to be very careful, since most hydrodynamical calculations – describing flow – fail to reproduce the hadron spectra with the same initial conditions (and vice versa). Hydrodynamic flow and shock formation has been proposed early<sup>209</sup> as the key mechanism for the creation of hot and dense matter during relativistic heavy-ion collisions. However, the full three-dimensional hydrodynamical flow problem is much more complicated than the one-dimensional Landau model<sup>219</sup> used in many of the present hydrodynamical calculations. The 3-dimensional compression and expansion dynamics yields complex triple differential cross-sections, which provide quite accurate spectroscopic handles on the equation of state. In this respect, it is important to consider also microscopic multi-component (pre-) hadron transport theory (see Section 2) as control models for viscous hydro and as background models to extract interesting non-hadronic effects from data.

In Fig. 47 we show the elliptic flow of  $D$ -mesons produced in  $Au + Au$  collisions at  $\sqrt{s} = 200$  GeV as a function of the transverse momentum  $p_T$  in HSD (solid blue

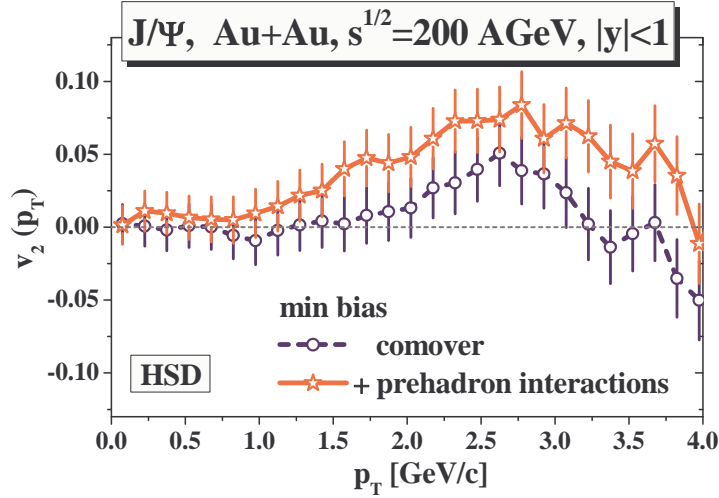


Fig. 48. Elliptic flow of  $J/\Psi$ -mesons produced in  $Au+Au$  collisions at  $\sqrt{s} = 200$  GeV as a function of  $p_T$  from HSD. The red line with open stars shows the HSD result for the  $v_2$  of  $D$ -mesons when including additionally pre-hadronic charm interactions as described in Section 6.3.

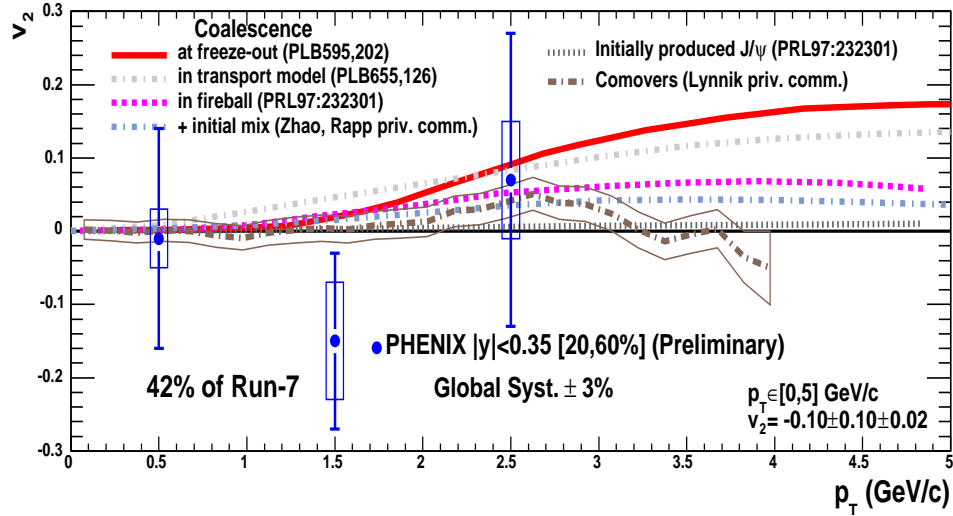


Fig. 49. Elliptic flow of  $J/\Psi$ -mesons produced in  $Au+Au$  collisions at  $\sqrt{s} = 200$  GeV as a function of  $p_T$  from HSD and other models. Preliminary PHENIX data <sup>212,213,214</sup> are shown by symbols. The figure is taken from Ref. <sup>213</sup>.

line with open circles) compared to the PHENIX data <sup>195</sup> on  $v_2$  of non-photonic electrons. Here the elliptic flow of  $D$ -mesons is clearly underestimated in the de-

fault (purely hadronic) HSD model (*cf.* Ref. <sup>94</sup>). Only when including pre-hadronic charm interactions - as described in Section 6.3 - the elliptic flow moderately increases (red line with open stars), but still stays below the PHENIX data. We thus conclude that the modeling of charm interactions by pre-hadronic interactions - as described in Section 6.3 - accounts for part of the non-hadronic generation of the  $v_2$ , but does not provide enough interaction strength in the early phase of the collision. Quite remarkably, this finding is again fully in line with the underestimation of high  $p_T$  hadron suppression <sup>168</sup> as well as far-side jet suppression <sup>169</sup> in the pre-hadronic interaction model. Independently, also the charm collective flow points towards strong partonic interactions in the early reaction phase beyond the pre-hadronic scattering incorporated so far.

Since a large fraction of  $J/\Psi$ 's in central Au+Au collisions at RHIC are created by  $D - \bar{D}$  recombination, the elliptic flow of  $J/\Psi$ 's obtained from HSD in the comover (purely hadronic) case is comparatively small, too (*cf.* Fig. 48). The preliminary PHENIX data <sup>212,213,214</sup> are additionally shown by blue symbols in Fig. 49, where the HSD prediction is represented by a brown (dash-dot) line and a band. The accuracy of the preliminary data so far does not allow for a differentiation between the different model predictions presented in Fig. 49.

In principle, partonic cascade simulations <sup>220,221,222,223,224,225,226</sup> are promising tools in approaching the mechanism of the early generation of elliptic flow. However, unexpectedly high parton cross sections of  $\sim 5-10$  mb have to be assumed in parton cascades <sup>151</sup> in order to reproduce the elliptic flow seen experimentally. These cross sections (per constituent quark) are roughly the same in the partonic and hadronic phase (or even higher in the partonic phase). In the new version of the parton cascade model of Xu and Greiner <sup>227</sup> lower binary cross sections are employed but additional  $2 \leftrightarrow 3$  gluonic reactions are incorporated that are very sensitive to the screening masses (parameters) used. Furthermore, a strong elliptic flow of particles may also be generated by repulsive mean-fields as known from the nuclear physics context <sup>52</sup>. In all the parton cascades addressed above no mean-fields or parton selfenergies are incorporated. In fact, a recent study within the Parton-Hadron-String-Dynamics (PHSD) approach suggests that a large fraction of the final elliptic flow might stem from strong repulsive partonic mean-fields <sup>43</sup>.

### 11.3. FAIR energies

The expected results for the  $D$ -meson elliptic flow  $v_2$  at mid-rapidity for Au+Au reactions at 25 A·GeV from HSD is compared in Fig. 50 with the  $v_2$  of charged hadrons. As seen from 50 the  $D, \bar{D}$  elliptic flow is smaller than the  $v_2$  of the lighter hadrons following essentially the mass ordering. Such a low elliptic flow is due to the moderate interaction rates of  $D, \bar{D}$  mesons in the hadronic expansion phase. A measurement of a sizeably larger elliptic flow of  $D$ -mesons at FAIR would indicate the presence of partonic degrees of freedom already at bombarding energies of 25 -

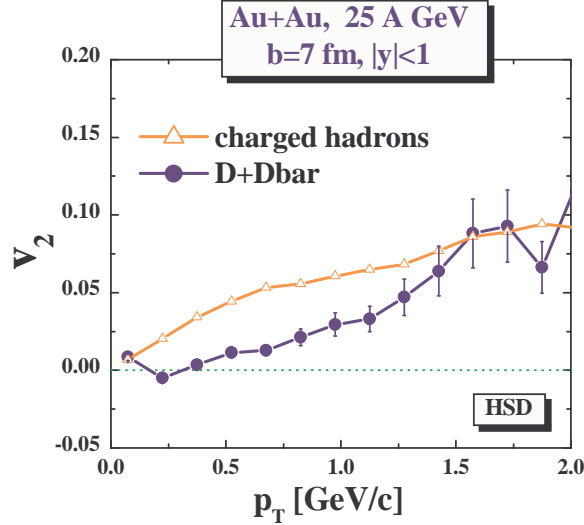


Fig. 50. The HSD predictions for the elliptic flow  $v_2$  of  $D + \bar{D}$ -mesons (solid lines with full dots) and charged hadrons (solid lines with open triangles) from Au + Au collisions at 25 A·GeV at  $b = 7$  fm versus  $p_T$  for  $|y| < 1$ . The figure is taken from Ref. <sup>30</sup>.

35 A·GeV.

## 12. Conclusions

This review has been devoted to an update of the information on charm dynamics gained from p+A and A+A reactions at SPS and RHIC energies in comparison to microscopic transport studies by incorporating different scenarios for the anomalous suppression of charmonia seen experimentally in central heavy-ion reactions. We have found that present data on charmonium suppression for Pb+Pb and In+In reactions at top SPS energies (158 A·GeV) compare well with transport calculations in the hadronic comover model involving only a single parameter for the average matrix element squared  $|M_0|^2$  that fixes the strength of the charmonium cross sections with comoving hadrons. This holds for the  $J/\Psi$  suppression as well as the  $\Psi'$  to  $J/\Psi$  ratio versus collision centrality. The bare ‘QGP threshold scenario’ gives satisfying results for the  $J/\Psi$  suppression for both systems (In+In and Pb+Pb) at 158 A·GeV but fails in the  $\Psi'$  to  $J/\Psi$  ratio since too many  $\Psi'$  already melt away for a critical energy density of 2 GeV/fm<sup>3</sup> at 158 A·GeV. These findings suggest that the charmonium dynamics in heavy-ion reactions is dominantly driven by hadronic interactions in the SPS energy regime. Since energy densities above 1 GeV/fm<sup>3</sup> are reached in central nucleus-nucleus collisions at 158 A·GeV, our observation indicates that hadronic correlators (with quantum numbers of the familiar hadrons) still persist above the critical energy density for the formation of a QGP. This finding is independently supported by lattice QCD calculations that show a survival of strongly bound hadronic states up to temperatures of 2  $T_c$ , which corresponds to



an energy density of about  $30 \text{ GeV}/\text{fm}^3$ . In fact, such high energies densities (or temperatures) are not reached even in central Au+Au (or Pb+Pb) collisions at the SPS.

The situation is found to be essentially different at top RHIC energies of  $\sqrt{s} = 200 \text{ GeV}$  (or  $21.3 \text{ A}\cdot\text{TeV}$ ). The study of the formation and suppression dynamics of  $J/\Psi$ ,  $\chi_c$  and  $\Psi'$  mesons within the HSD transport approach for Au+Au reactions at the top RHIC energy has demonstrated that both scenarios i.e. ‘charmonium melting’ in a QGP state as well as the hadronic ‘comover absorption and recreation model’ fail severely at RHIC energies. This is found in the  $J/\Psi$  suppression pattern versus the centrality of the collision, in the  $J/\Psi$  rapidity distribution as well as in the differential elliptic flow of  $J/\Psi$  and the charmonium nuclear modification factor  $R_{AA}$  as a function of transverse momentum  $p_T$  (in comparison to recent data from the PHENIX Collaboration<sup>97</sup>). Especially the latter observable indicates that at least part of the final  $J/\Psi$ ’s are created by coalescence of  $c\bar{c}$  pairs in the hadronization phase. Only when including pre-hadronic degrees in the early charm reaction dynamics, the general suppression pattern of charmonia may be reasonably described; though, the elliptic flow  $v_2$  is still (slightly) underestimated. On the other hand,  $R_{AA}(p_T)$  for  $J/\Psi$  mesons cannot be described in the comover approach, even when incorporating the early prehadron interactions. This analysis demonstrates that the dynamics of  $c, \bar{c}$  quarks in heavy-ion reactions at RHIC energies are dominated by partonic interactions in the strong QGP (sQGP) and can neither be modeled by ‘hadronic’ interactions nor described appropriately by color screening alone.

The different scenarios of ‘charmonium melting’ and ‘hadronic comover dissociation’ may clearly be distinguished at FAIR energies (of about  $25 - 35 \text{ A}\cdot\text{GeV}$ ), where the centrality dependence of the  $J/\Psi$  survival probability and the  $\Psi'$  to  $J/\Psi$  ratio are significantly lower in the ‘comover absorption’ model than in the ‘charmonium melting’ scenario. This result comes about since the average comover density decreases only moderately with lower bombarding energy, whereas the region in space-time with energy densities above critical values of *e.g.*  $2 \text{ GeV}/\text{fm}^3$  decreases rapidly and ceases to exist below about  $20 \text{ A}\cdot\text{GeV}$  even in central collisions of Au+Au.

### 13. Open questions and perspectives

Although substantial progress has been achieved on the field of charmonium physics in the last years - both theoretically and experimentally - the description of charmonium and open charm dynamics in relativistic nucleus-nucleus collisions remains a challenging task. So far we have just obtained a very rough picture of the collective flow and attenuation pattern of charmed and hidden-charm mesons and a profound microscopic understanding is still lacking.

On the theoretical side the basic open problem - and future challenge - is to incorporate explicit partonic degrees of freedom in the description of relativistic

nucleus-nucleus collisions and their transition to hadronic states in a microscopic transport approach. The available string/hadron transport models only schematically incorporate some parton dynamics (by modeling interactions of pre-hadrons) but definitely fail in describing the partonic phase in accordance with an equation of state from lattice QCD. On the other side the present partonic cascade simulations (propagating massless partons) fail in describing the reaction dynamics when employing cross sections from perturbative QCD. One might argue that this is due to the neglect of partonic selfenergies which even in case of small interaction strength should be large due to the high parton densities reached in ultra-relativistic nucleus-nucleus collisions. In fact, the studies of Peshier in a dynamical quasiparticle approach<sup>228,229</sup> indicate that the effective degrees of freedom in a partonic phase should be quite massive and have a width in the order of the pole mass already slightly above  $T_c$ . Such short lived degrees of freedom have to be propagated in off-shell transport approaches which also allow for a description of hadronization in terms of ‘local’ rate equations<sup>43</sup>.

On the experimental side, further differential spectra of charmonia and open charm mesons will become available from RHIC-II and the LHC in the next years. While studies at RHIC most likely probe the ‘partonic fluid’ produced in the heavy-ion reactions, experiments at LHC - especially for high  $p_T$  degrees of freedom - might provide further surprising results with respect to the properties of the partonic system at extreme energy densities. Also the future charm measurements at FAIR are expected to provide new insight into the charm dynamics especially at high baryon density. Accordingly, the field of open charm and charmonium physics is far from being closed and will remain exciting for a long time.

### Acknowledgements

The authors gratefully acknowledge stimulating discussions with A. Andronic, P. Braun-Munzinger, H. van Hees, J. Stachel, R. Rapp, P. Senger, L. Tolos, A. Ramos, V. D. Toneev, M. I. Gorenstein, R. Granier de Cassagnac, E. Scapparini. We are especially indebted to H. Stöcker for his continuous support, valuable suggestions and lively discussions.

### References

1. Nucl. Phys. **A774**, 1 (2006).
2. Z. Fodor and S. D. Katz, JHEP **0203**, 014 (2002); Z. Fodor, S. D. Katz, and K. K. Szabo, Phys. Lett. **B568**, 73 (2003).
3. NA38, M. C. Abreu *et al.*, Phys. Lett. **B449**, 128 (1999).
4. NA50, B. Alessandro *et al.*, Eur. Phys. J. **C39**, 335 (2005).
5. NA60, A. Förster *et al.*, J. Phys. **G32**, S51 (2006).
6. STAR, I. Arsene *et al.*, Nucl. Phys. **A757**, 1 (2005); STAR, B. B. Back *et al.*, Nucl. Phys. **A757**, 28 (2005); STAR, J. Adams *et al.*, Nucl. Phys. **A757**, 102 (2005); STAR, K. Adcox *et al.*, Nucl. Phys. **A757**, 184 (2005).
7. ALICE, A. Mastroserio, (2008), arXiv:0806.2526 [nucl-ex].

8. O. Brüning *et al.*, LHC design report. Vol. I: The LHC main ring, CERN-2004-003-V-1, <http://ab-div.web.cern.ch/ab-div/Publications/LHC-DesignReport.html>.
9. K. Peters, AIP Conf. Proc. **814**, 33 (2006).
10. M. Gazdzicki, Eur. Phys. J. ST **155**, 37 (2008).
11. A. N. Sissakian, A. S. Sorin, and V. D. Toneev, (2006), arXiv:nucl-th/0608032.
12. NA49, S. V. Afanasiev *et al.*, Phys. Rev. **C66**, 054902 (2002).
13. NA49, V. Friese *et al.*, J. Phys. **G30**, S119 (2004).
14. V. Toneev, (2007), arXiv:0709.1459 [nucl-ex].
15. J. D. Bjorken, Phys. Rev. **D27**, 140 (1983).
16. S. Fortunato, F. Karsch, P. Petreczky, and H. Satz, Phys. Lett. **B502**, 321 (2001).
17. H. Stöcker and W. Greiner, Phys. Rept. **137**, 277 (1986).
18. W. Cassing, E. L. Bratkovskaya, and S. Juchem, Nucl. Phys. **A674**, 249 (2000).
19. I. C. Arsene *et al.*, Phys. Rev. **C75**, 034902 (2007).
20. M. H. Thoma, J. Phys. **G31**, L7 (2005).
21. M. H. Thoma, Nucl. Phys. **A774**, 307 (2006).
22. A. Peshier and W. Cassing, Phys. Rev. Lett. **94**, 172301 (2005).
23. E. Shuryak, Prog. Part. Nucl. Phys. **53**, 273 (2004).
24. T. Hirano and M. Gyulassy, Nucl. Phys. **A769**, 71 (2006).
25. T. Matsui and H. Satz, Phys. Lett. **B178**, 416 (1986).
26. H. Satz, Rep. Progr. Phys. **63**, 1511 (2000).
27. H. Satz, J. Phys. **G32**, R25 (2006).
28. F. Karsch, D. Kharzeev, and H. Satz, Phys. Lett. **B637**, 75 (2006).
29. J. Rafelski and B. Müller, Phys. Rev. Lett. **48**, 1066 (1982), Erratum-ibid. **56**, 2334 (1986).
30. *CBM physics book*, to be published.
31. A. Dumitru and C. Spieles, Phys. Lett. **B446**, 326 (1999).
32. N. Xu, Prog. Part. Nucl. Phys. **53**, 165 (2004), and references therein.
33. W. Cassing, E. L. Bratkovskaya, and A. Sibirtsev, Nucl. Phys. **A691**, 753 (2001).
34. V. Greco, C. M. Ko, and R. Rapp, Phys. Lett. **B595**, 202 (2004).
35. M. J. Leitch, Eur. Phys. J. **A31**, 868 (2007).
36. W. Cassing and E. L. Bratkovskaya, Phys. Rep. **308**, 65 (1999).
37. W. Cassing, V. Metag, U. Mosel, and K. Niita, Phys. Rept. **188**, 363 (1990).
38. W. Cassing and U. Mosel, Prog. Part. Nucl. Phys. **25**, 235 (1990).
39. C. M. Ko and G.-Q. Li, J. Phys. **G22**, 1673 (1996).
40. S. A. Bass *et al.*, Prog. Part. Nucl. Phys. **42**, 255 (1998).
41. W. Cassing, Nucl. Phys. **A791**, 365 (2007).
42. B. Zhang *et al.*, Phys. Rev. **C61**, 067901 (2000); Z.W. Lin *et al.*, Phys. Rev. **C64**, 011902 (2001); Z. W. Lin *et al.*, Nucl. Phys. **A698**, 375 (2002).
43. W. Cassing and E. L. Bratkovskaya, (2008), arXiv:0808.0022 [hep-ph].
44. O. Linnyk, E. L. Bratkovskaya, W. Cassing, and H. Stöcker, Nucl. Phys. **A786**, 183 (2007).
45. O. Linnyk, E. L. Bratkovskaya, W. Cassing, and H. Stöcker, Phys. Rev. **C76**, 041901 (2007).
46. O. Linnyk, E. L. Bratkovskaya, W. Cassing, and H. Stöcker, J. Phys. **G35**, 044037 (2008).
47. E. L. Bratkovskaya, W. Cassing, and H. Stöcker, Phys. Rev. **C67**, 054905 (2003).
48. E. L. Bratkovskaya, A. P. Kostyuk, W. Cassing, and H. Stöcker, Phys. Rev. **C69**, 054903 (2004).
49. M. Bleicher *et al.*, J. Phys. **G25**, 1859 (1999).
50. W. Ehehalt and W. Cassing, Nucl. Phys. **A602**, 449 (1996).

51. M. Effenberger, E. L. Bratkovskaya, and U. Mosel, Phys. Rev. **C60**, 044614 (1999).
52. A. B. Larionov, W. Cassing, C. Greiner, and U. Mosel, Phys. Rev. **C62**, 064611 (2000); A. B. Larionov *et al.*, Phys. Rev. **C71**, 034910 (2005).
53. H. Sorge, Phys. Rev. **C52**, 3291 (1995).
54. K. K. Gudima, M. Ploszajczak and V. D. Toneev, Phys. Lett. **B328**, 249 (1994); N.S. Amelin *et al.*, Phys. Rev. **C47**, 2299 (1993).
55. E.E. Zabrodin, C. Fuchs, L.V. Bravina, A. Faessler, Phys. Rev. **C63**, 034902 (2001); Phys. Lett. **B508**, 184 (2001); G. Burau *et al.*, Phys. Rev. **C71**, 054905 (2005); J. Bleibel, G. Burau, A. Faessler, C. Fuchs, Nucl. Phys. **A767**, 218 (2006); L. Bravina *et al.*, Phys. Lett. **B631**, 109 (2005); L.V. Bravina *et al.*, Phys. Lett. **B543**, 217 (2002).
56. H. Weber, E. Bratkovskaya, W. Cassing, and H. Stöcker, Phys. Rev. **C67**, 014904 (2003).
57. FOPI, A. Andronic *et al.*, Phys. Rev. **C67**, 034907 (2003).
58. FOPI, A. Andronic *et al.*, Phys. Rev. **C64**, 041604 (2001).
59. S. Soff, S. A. Bass, M. Bleicher, H. Stöcker, and W. Greiner, (1999), arXiv:nucl-th/9903061.
60. L. P. Csernai and D. Röhrich, Phys. Lett. **B458**, 454 (1999).
61. P. K. Sahu, W. Cassing, U. Mosel, and A. Ohnishi, Nucl. Phys. **A672**, 376 (2000).
62. P. K. Sahu and W. Cassing, Nucl. Phys. **A712**, 357 (2002).
63. FOPI, A. Andronic *et al.*, Nucl. Phys. **A679**, 765 (2001).
64. FOPI, A. Andronic *et al.*, Phys. Lett. **B612**, 173 (2005).
65. FOPI, A. Andronic, Nucl. Phys. **A661**, 333 (1999).
66. E. L. Bratkovskaya *et al.*, Phys. Rev. **C69**, 054907 (2004).
67. A. D. Frawley, T. Ullrich, and R. Vogt, Phys. Rept. **462**, 125 (2008).
68. R. Vogt, Eur. Phys. J. ST **155**, 213 (2008).
69. NA16, M. Aguilar-Benitez *et al.*, Phys. Lett. **B135**, 237 (1984).
70. NA27, M. Aguilar-Benitez *et al.*, Z. Phys. **C40**, 321 (1998).
71. E743, R. Ammar *et al.*, Phys. Rev. Lett. **61**, 2185 (1998).
72. E653, K. Kodama *et al.*, Phys. Lett. **B263**, 573 (1991), *ibid.* **B284**, 461 (1992).
73. E789, M. J. Leitch *et al.*, Phys. Rev. Lett. **72**, 2542 (1994).
74. NA32, S. Barlag *et al.*, Z. Phys. **C39**, 451 (1988), *ibid.* **C49**, 555 (1991), Phys. Lett. **B247**, 113 (1990).
75. E769, G. A. Alves *et al.*, Phys. Rev. Lett. **77**, 2388 (1996), *ibid.* 2392.
76. WA92, M. Adamovich *et al.*, Nucl. Phys. **B495**, 3 (1997).
77. E791, E. M. Aitala *et al.*, Eur. Phys. J. **C4**, 1 (1999).
78. PHENIX, S. S. Adler *et al.*, Phys. Rev. Lett. **92**, 051802 (2004), *ibid.* **96**, 012304 (2006).
79. The open HSD source code is available from the URL – <http://www.th.physik.uni-frankfurt.de/brat/hsd.html>.
80. T. Sjöstrand *et al.*, Comput. Phys. Commun. **135**, 238 (2001).
81. PHENIX, A. Adare *et al.*, Phys. Rev. Lett. **98**, 232002 (2007).
82. O. Linnyk, E. L. Bratkovskaya, and W. Cassing, Nucl. Phys. **A807**, 79 (2008).
83. E705, L. Antoniazzi *et al.*, Phys. Rev. Lett. **70**, 383 (1993).
84. WA11, Y. Lemoigne *et al.*, Phys. Lett. **B113**, 509 (1982).
85. NA50, B. Alessandro *et al.*, Phys. Lett. **B553**, 167 (2003).
86. K. Hagiwara *et al.*, Phys. Rev. **D66**, 010001 (2002), (Review of Particle Properties).
87. J. Geiss *et al.*, Phys. Lett. **B447**, 31 (1999).
88. W. Cassing and E. L. Bratkovskaya, Nucl. Phys. **A623**, 570 (1997).
89. W. Cassing and C. M. Ko, Phys. Lett. **B396**, 39 (1997).
90. J. O. Schmitt, G. C. Nayak, H. Stöcker, and W. Greiner, Phys. Lett. **B498**, 163

- (2001).
91. J. Geiss, W. Cassing, and C. Greiner, Nucl. Phys. **A644**, 107 (1998).
  92. R. Vogt, Phys. Rep. **310**, 197 (1999).
  93. E672/E706, V. Abramov *et al.*, FERMILAB-Pub-91/62-E, IFVE-91-9, Mar. 1991.
  94. E. L. Bratkovskaya, W. Cassing, H. Stöcker, and N. Xu, Phys. Rev. **C71**, 044901 (2005).
  95. STAR, A. Tai *et al.*, J. Phys. **G30**, S809 (2004).
  96. PHENIX, S. S. Adler *et al.*, Phys. Rev. **C71**, 034908 (2005).
  97. PHENIX, A. Adare *et al.*, Phys. Rev. Lett. **98**, 232301 (2007).
  98. NA50, B. Alessandro *et al.*, arXiv:nucl-ex/0612012.
  99. D. Kharzeev and R. L. Thews, Phys. Rev. **C60**, 041901 (1999).
  100. NA50, B. Alessandro *et al.*, Eur. Phys. J. **C49**, 559 (2007).
  101. CMS, D. d'Enterria *et al.*, (2008), arXiv:0805.4769 [nucl-ex].
  102. NA50, G. Borges *et al.*, J. Phys. **G32**, S381 (2006).
  103. K. Martins, D. Blaschke, and E. Quack, Phys. Rev. **C51**, 2723 (1995).
  104. C. Gerschel and J. Hüfner, Z. Phys. **C56**, 171 (1992).
  105. I. C. Arsene *et al.*, (2007), arXiv:0708.3801 [hep-ph].
  106. A. Capella, E. G. Ferreira, A. Capella, and E. G. Ferreira, Phys. Rev. **C76**, 064906 (2007).
  107. R. Vogt, Phys. Rev. **C71**, 054902 (2005).
  108. N. Armesto *et al.*, Eur. Phys. J. **C29**, 531 (2003).
  109. A. Capella and E. G. Ferreira, Eur. Phys. J. **C42**, 419 (2005).
  110. E. G. Ferreira, F. Fleuret, and A. Rakotozafindrabe, (2008), arXiv:0801.4949 [hep-ph].
  111. B. Kopeliovich, A. Tarasov, and J. Hüfner, Nucl. Phys. **A696**, 669 (2001).
  112. A. Capella *et al.*, (2007), arXiv:0712.4331 [hep-ph].
  113. PHENIX, A. Adare *et al.*, Phys. Rev. **C77**, 024912 (2008).
  114. K. J. Eskola, V. J. Kolhinen, and P. V. Ruuskanen, Nucl. Phys. **B535**, 351 (1998).
  115. K. J. Eskola, V. J. Kolhinen, and C. A. Salgado, Eur. Phys. J. **C9**, 61 (1999).
  116. D. de Florian and R. Sassot, Phys. Rev. **D69**, 074028 (2004).
  117. A. M. Rakotozafindrabe, (2008), arXiv:0806.3678 [hep-ph].
  118. PHENIX, S. S. Adler *et al.*, Phys. Rev. Lett. **96**, 012304 (2006).
  119. PHENIX, R. Granier de Cassagnac, J. Phys. **G34**, S955 (2007).
  120. A. Andronic, P. Braun-Munzinger, K. Redlich, and J. Stachel, Nucl. Phys. **A789**, 334 (2007).
  121. A. Andronic, P. Braun-Munzinger, K. Redlich, and J. Stachel, Phys. Lett. **B659**, 149 (2008).
  122. L. Grandchamp, R. Rapp, and G. E. Brown, Phys. Rev. Lett. **92**, 212301 (2004).
  123. L. Tolos, A. Ramos, and T. Mizutani, Phys. Rev. **C77**, 015207 (2008).
  124. R. Molina, D. Gamermann, E. Oset, and L. Tolos, (2008), arXiv:0806.3711 [nucl-th].
  125. B. Zhang, C. M. Ko, B.-A. Li, Z. Lin, and B.-H. Sa, Phys. Rev. **C62**, 054905 (2000).
  126. W. Cassing *et al.*, Prog. Part. Nucl. Phys. **53**, 211 (2004).
  127. C. Spieles *et al.*, J. Phys. **G25**, 2351 (1999), Phys. Rev. **C60**, 054901 (1999).
  128. NA50, L. Ramello *et al.*, Nucl. Phys. **A715**, 243 (2003).
  129. S. Datta, F. Karsch, P. Petreczky, and I. Wetzorke, J. Phys. **G30**, S1347 (2004), J. Phys. **G30**, S889 (2004).
  130. M. Asakawa and T. Hatsuda, J. Phys. **G30**, S1337 (2004).
  131. C. Lourenco and H. Wohri, Phys. Rept. **433**, 127 (2006).
  132. C. M. Ko, X. N. Wang, and X. F. Zhang, Phys. Lett. **B444**, 237 (1998).
  133. N. Armesto and A. Capella, Phys. Lett. **B430**, 23 (1998).

134. M. Gazdzicki and M. I. Gorenstein, Phys. Rev. Lett. **83**, 4009 (1999).
135. P. Braun-Munzinger, D. Miskowiec, A. Drees, and C. Lourenco, Eur. Phys. J. **C1**, 123 (1998).
136. R. L. Thews, M. Schroedter, and J. Rafelski, Phys. Rev. **C63**, 054905 (2001).
137. P. Braun-Munzinger and J. Stachel, Phys. Lett. **B490**, 196 (2000).
138. B. Müller, Nucl. Phys. **A661**, 272c (1999).
139. P. Braun-Munzinger and K. Redlich, Eur. Phys. J. **C16**, 519 (2000).
140. K. Martins, D. Blaschke, and E. Quack, Phys. Rev. **C51**, 2723 (1995).
141. C. Y. Wong, E. S. Swanson, and T. Barnes, Phys. Rev. **C62**, 045201 (2000).
142. F. O. Duraes *et al.*, Phys. Rev. **C68**, 035208 (2003).
143. W. Cassing, L. A. Kondratyuk, G. I. Lykasov, and M. V. Ryzanin, Phys. Lett. **B513**, 1 (2001).
144. Z. Lin and C. M. Ko, Phys. Rev. **C62**, 034903 (2000).
145. Z. Lin and C. M. Ko, J. Phys. **G27**, 617 (2001).
146. K. L. Haglin, Phys. Rev. **C61**, 031903 (2000).
147. P. Braun-Munzinger and K. Redlich, Nucl. Phys. **A661**, 546 (1999).
148. L. Grandchamp and R. Rapp, Phys. Lett. **B523**, 60 (2001).
149. L. Grandchamp and R. Rapp, Nucl. Phys. **A709**, 415 (2002).
150. Z.-w. Lin and C. M. Ko, J. Phys. **G27**, 617 (2001).
151. Z.-w. Lin and C. M. Ko, Phys. Rev. **C65**, 034904 (2002).
152. L. Grandchamp and R. Rapp, Phys. Lett. **B523**, 60 (2001), Nucl. Phys. **A709**, 415 (2002).
153. J. P. Blaizot and J. Y. Ollitrault, Phys. Rev. Lett. **77**, 1703 (1996).
154. S. Digal, S. Fortunato, and H. Satz, Eur. Phys. J. **C32**, 547 (2004).
155. G. Aarts *et al.*, (2007), arXiv:0705.2198[hep-lat].
156. S. Datta, F. Karsch, P. Petreczky, and I. Wetzorke, Phys. Rev. **D69**, 094507 (2004).
157. P. Petreczky and K. Petrov, Phys. Rev. **D70**, 054503 (2004).
158. RBC-Bielefeld, K. Petrov, PoS **LAT2006**, 144 (2006).
159. O. Kaczmarek, PoS **CPOD07**, 043 (2007).
160. A. Mocsy and P. Petreczky, (2007), arXiv:0706.2183 [hep-ph].
161. S. Digal, P. Petreczky, and H. Satz, Phys. Lett. **B514**, 57 (2001).
162. R. Rapp and H. van Hees, (2008), arXiv:0803.0901 [hep-ph].
163. E. V. Shuryak and I. Zahed, Phys. Rev. **D70**, 054507 (2004).
164. M. Mannarelli and R. Rapp, Phys. Rev. **C72**, 064905 (2005).
165. A. Mocsy and P. Petreczky, Phys. Rev. **D73**, 074007 (2006).
166. W. M. Alberico, A. Beraudo, A. De Pace, and A. Molinari, Phys. Rev. **D72**, 114011 (2005).
167. D. Cabrera and R. Rapp, Phys. Rev. **D76**, 114506 (2007).
168. W. Cassing, K. Gallmeister, and C. Greiner, Nucl. Phys. **A735**, 277 (2004).
169. K. Gallmeister and W. Cassing, Nucl. Phys. **A748**, 241 (2005).
170. H. van Hees and R. Rapp, Phys. Rev. **C71**, 034907 (2005).
171. T. Falter, K. Gallmeister, W. Cassing, and U. Mosel, Phys. Rev. **C70**, 054609 (2004).
172. T. Falter, K. Gallmeister, W. Cassing, and U. Mosel, Phys. Lett. **B594**, 61 (2004).
173. R. Rapp, D. Blaschke, and P. Crochet, (2008), arXiv:0807.2470 [hep-ph].
174. R. Rapp and L. Grandchamp, J. Phys. **G30**, S305 (2004).
175. D. Blaschke, Y. Kalinovsky, and V. Yudichev, Lect. Notes Phys. **647**, 366 (2004).
176. M. Bedjidian *et al.*, arXiv:hep-ph/0311048.
177. P. Braun-Munzinger and J. Stachel, Nucl. Phys. **A690**, 119 (2001).
178. R. Rapp, Eur. Phys. J. **C43**, 91 (2005).
179. A. Capella and E. Ferreira, Eur. Phys. J. **C42**, 419 (2005).



180. F. Karsch, J. Phys. **G30**, S887 (2004).
181. M. I. Gorenstein, A. P. Kostyuk, H. Stöcker, and W. Greiner, Phys. Lett. **B509**, 277 (2001).
182. NA50, M. C. Abreu *et al.*, Nucl. Phys. **A638**, 261 (1998).
183. NA60, R. Arnaldi *et al.*, Nucl. Phys. **A774**, 711 (2006).
184. L. Grandchamp, R. Rapp, and G. E. Brown, J. Phys. **G30**, S1355 (2004).
185. NA60, E. Scapparini, J. Phys. **G34**, S463 (2007).
186. A. Andronic, P. Braun-Munzinger, K. Redlich, and J. Stachel, Phys. Lett. **B652**, 259 (2007).
187. V. Friese, Nucl. Phys. **A774**, 377 (2006).
188. A. Andronic, private communication.
189. F. Becattini, Z. Phys. **C69**, 485 (1996).
190. N. Xu and Z.-b. Xu, Nucl. Phys. **A715**, 587 (2003).
191. H. van Hecke, H. Sorge, and N. Xu, Nucl. Phys. **A661**, 493 (1999).
192. H. Sorge, Phys. Lett. **B373**, 16 (1996).
193. A. Mishra, E. L. Bratkovskaya, J. Schaffner-Bielich, S. Schramm, and H. Stöcker, Phys. Rev. **C70**, 044904 (2004).
194. PHENIX, C. Luiz da Silva, (2006), arXiv:hep-ex/0606021.
195. PHENIX, A. Adare *et al.*, Phys. Rev. Lett. **98**, 172301 (2007).
196. STAR, J. Bielcik, Nucl. Phys. **A774**, 697 (2006).
197. J. L. Nagle and T. S. Ullrich, (2002), arXiv:nucl-ex/0203007.
198. PHENIX, S. S. Adler *et al.*, Phys. Rev. **C69**, 034910 (2004).
199. STAR, J. Adams *et al.*, Phys. Rev. Lett. **91**, 172302 (2003).
200. BRAHMS, I. Arsene *et al.*, Phys. Rev. Lett. **91**, 072305 (2003).
201. X.-N. Wang, Phys. Rev. **C58**, 2321 (1998).
202. R. Baier, D. Schiff, and B. G. Zakharov, Ann. Rev. Nucl. Part. Sci. **50**, 37 (2000).
203. PHENIX, S. S. Adler *et al.*, Phys. Rev. Lett. **91**, 072303 (2003).
204. STAR, J. Adams *et al.*, Phys. Rev. Lett. **91**, 072304 (2003).
205. KaoS, D. Brill *et al.*, Phys. Rev. Lett. **71**, 336 (1993).
206. TAPS, L. B. Venema *et al.*, Phys. Rev. Lett. **71**, 835 (1993).
207. S. Voloshin and Y. Zhang, Z. Phys. **C70**, 665 (1996).
208. H. Stöcker, J. Hofmann, J. A. Maruhn, and W. Greiner, Prog. Part. Nucl. Phys. **4**, 133 (1980).
209. J. Hofmann, H. Stöcker, W. Scheid, and W. Greiner, Report of the Workshop on BeV/nucleon Collisions of Heavy Ions: How and Why, Bear Mountain, New York, 29 Nov - 1 Dec 1974.
210. J. Hofmann, H. Stöcker, U. W. Heinz, W. Scheid, and W. Greiner, Phys. Rev. Lett. **36**, 88 (1976).
211. NA60, R. Arnaldi *et al.*, Nucl. Phys. **A783**, 261 (2007).
212. R. Granier de Cassagnac, (2008), arXiv:0806.0046 [hep-ph].
213. PHENIX, C. Silvestre, (2008), arXiv:0806.0475 [nucl-ex].
214. PHENIX, E. T. Atomssa, (2008), arXiv:0805.4562 [nucl-ex].
215. P. F. Kolb, U. W. Heinz, P. Huovinen, K. J. Eskola, and K. Tuominen, Nucl. Phys. **A696**, 197 (2001).
216. D. Teaney, Phys. Rev. **C68**, 034913 (2003).
217. E. Shuryak, J. Phys. **G30**, S1221 (2004).
218. T. Hirano and Y. Nara, J. Phys. **G31**, S1 (2005).
219. L. Landau and E. Lifshitz, *Fluid Mechanics* (New York: Pergamon Press (Addison-Wesley), 1959).
220. K. Geiger, Phys. Rept. **258**, 237 (1995).

221. B. Zhang, M. Gyulassy, and C. M. Ko, Phys. Lett. **B455**, 45 (1999).
222. D. Molnar and M. Gyulassy, Nucl. Phys. **A697**, 495 (2002), Erratum-ibid. **A703**, 893 (2002).
223. D. Molnar and M. Gyulassy, Nucl. Phys. **A698**, 379 (2002).
224. S. A. Bass, B. Muller, and D. K. Srivastava, Phys. Lett. **B551**, 277 (2003).
225. Z.-W. Lin *et al.*, Phys. Rev. **C72**, 064901 (2005).
226. Z. Xu and C. Greiner, Phys. Rev. **C71**, 064901 (2005).
227. O. Fochler, Z. Xu, and C. Greiner, (2008), arXiv: 0806.1169 [hep-ph].
228. A. Peshier, Phys. Rev. **D70**, 034016 (2004).
229. A. Peshier, J. Phys. **G31**, S371 (2005).